

SILICON NANOCRYSTAL CHARGING DYNAMICS AND
MEMORY DEVICE APPLICATIONS

Thesis by
Tao Feng

In Partial Fulfillment of the Requirements
for the degree of
Doctor of Philosophy



California Institute of Technology
Pasadena, California

2005

(Defended November 16th 2005)

© 2005

Tao Feng

All Rights Reserved

To my wife, Jun

with all my love

Acknowledgements

It is my great pleasure to take this opportunity to thank all of the people who have contributed to my thesis directly or indirectly.

First of all, I am greatly indebted to my advisor, Professor Harry A. Atwater, for his generous support throughout my Ph.D. study at Caltech. He took me into the world of semiconductors with his broad knowledge and precious insights. I was very impressed by his enthusiasm and strict attitude both as a scientist and as an academic professional. He helped me to be independent and creative in almost all aspects of research, and provided me warm and timely encouragement while I was facing difficulties. Throughout my life I will benefit from the experience, knowledge, and confidence that I gained while working with Professor Atwater.

I'd like to thank my predecessor, Elizabeth Boer, for introducing me to atomic force microscopy (AFM). She told me many times one should not nod and say "yes" until something is 100% understood. I was deeply impressed and influenced by this seemingly trivial but very important attitude of studying as well as doing research. I must thank her for the time she spent with me and for her pioneer investigations into the charge dissipation problems in Si nanocrystal doped SiO₂ film using an ambient AFM. I also had the great pleasure to collaborate with Dr. Hongbin Yu in Jim Heath's group. He is an experienced surface physicist specializing in ultrahigh vacuum scanning tunneling microscopy (UHV STM). I especially thank him for providing me with many helpful suggestions and consultations on UHV STM/AFM. I owe much to Alireza Ghaffari for his instruction on cleanroom operations. I would like to thank him for showing me how to

use so many facilities, including the ellipsometer, SEM, evaporator, and techniques in the standard semiconductor microfabrication.

I have enjoyed interacting with many talented postdocs and graduate students in the Atwater group and have learned a great deal from them. Dr. Mark Brongersma impressed me with his talent and modesty from the first day I entered the group and had him as my officemate. It was really a pity for me that he transferred to the Vahala group and then went to Stanford University so soon. Dr. Pieter Kik can always find small but very useful software for research on the web, in most cases available immediately without Harry's signature because it was free! Dr. Young-Bae Park showed very generous interest and broad knowledge. He must read thousands of papers every year because he is always ready to offer suggestions to others. Dr. Domenico Pacifici helped me get a clearer understanding of the formation and structure of silicon nanoclusters embedded in SiO_2 . I must thank Rob Walters and Julie Biteen for their help on PL experiments and for providing me some nanocrystal samples. Oh, Robb, thanks for lending me your caliper so many times. I am also indebted to Rhett Brewer for his help on the initial effort to use RHEED on nanocrystal samples. I enjoyed interactions with my longest officemate, Julie Casperson Brewer, whose brilliant smile made me feel the sunshine of California even inside the building. I received help from almost every member of our group when I was putting together the UHV AFM system. I would like to give special thanks to Maribeth Mason and Dr. Sungjee Kim. Brendan Kayes also deserves to be thanked. He was always the first one in my mind when I needed a hand because his office was so close to lab 249, and he always offered me help without any hesitation. Gerald Miller joined the group this summer, and I really enjoyed the time that

we spent together watching the dissipation of electrons and holes. In addition, I am indebted to him for his help in proofreading my thesis.

I also would like to thank all other Atwater group members past and present. They are: Dr. Anna Fontcuberta i Morral, Dr. Chang-Geun Ahn, Regina Ragan, Sefan Maier, Michelle Ostraat, James Zahler, Jason Holt, Matthew Dicken, Jennifer Dionne, Luke Sweatlock, Christine Richardson, Katsu Tanabe, Carrie Ross, Jennifer Ruglovsky, Ken Diest, Melissa Griggs, Darci Taylor, Dr. Henri Lezec, and Professor Albert Polman. I enjoyed my conversations with them and appreciated the help they gave me. Many thanks also to all my friends at Caltech and who were once at Caltech - you know who you are.

Finally, I am deeply grateful to my family members without whom this thesis won't be possible. I thank my parents for their unlimited support and confidence in me. I also want to thank my wife, Jun, to whom this thesis is dedicated. I am indebted to her for everything she did for me, which cannot be listed here in simple words.

– *Tao Feng*

Pasadena, CA

September, 2005

ABSTRACT

The application of Si nanocrystals as floating gate in the metal oxide semiconductor field-effect transistor (MOSFET) based memory, which brings many advantages due to separated charge storage, attracted much attention in recent years. In this work, Si nanocrystal memory with nanocrystals synthesized by ion implantation was characterized to provide a better understanding of the relationship between structure and performance – especially charge retention characteristics.

In the structural characterization it was demonstrated that scanning tunneling microscopy (STM) and non-contact atomic force microscopy (nc-AFM) enable much more accurate measurements of the ensemble size distribution and array density for small Si nanocrystals in SiO₂, estimated to be around 2–3 nm and 4×10^{12} – 3×10^{13} cm⁻², respectively. The reflection high energy electron diffraction (RHEED) pattern further verified the existence of nanocrystals in SiO₂. Capacitance-voltage (C-V) measurements demonstrated the memory effects. The comparison between charge density and nanocrystal density suggests single charge storage on individual Si nanocrystals.

The electronic property of tunnel oxide layer is a key factor influencing charge retention, and was characterized by conductive atomic force microscopy (C-AFM). An overall high conductance observed between the nanocrystal floating gate and the substrate is believed to be responsible for the relatively short retention time for electrons. A narrowed denuded zone contaminated with nanocrystals is suggested to be the reason for the high conductance, which is further supported by switching events and fluctuations in local current-voltage (I-V) curves. From the results of C-AFM, a better control of

nanocrystal distribution close to the channel is shown to be critical for non-volatile nanocrystal memory made via Si ion implantation.

Nanoscale charge retention characteristics of both electrons and holes were probed directly by ultrahigh vacuum (UHV) nc-AFM, in which a highly doped Si tip was applied to inject charges into the nanocrystal layer and monitor subsequent charge dissipation. The results reveal a much longer hole retention time (e.g., >1 day) than that for electrons (e.g., <1 hour), which is consistent with the charge retention characteristics from electrical characterization of nanocrystal floating gate MOS capacitors as well as time-resolved photoluminescence measurements. The large difference in charge retention times for electrons and holes is attributed to the difference in tunneling barrier heights: 3.1 eV and 4.7 eV for electrons and holes, respectively. Based on the charge injection and retention characteristics obtained from UHV nc-AFM and nanocrystal floating gate MOS devices, we suggest that hole programming in Si nanocrystal memory is an interesting choice in improving data retention or in further device scaling.

UHV nc-AFM guarantees high detection sensitivity and stability in charge imaging experiments due to a lack of air damping, so a three-dimensional (3D) electrostatic model can be developed to provide quantitative information regarding the distribution and evolution of the localized charges. For example, a transition from initial complementary error function distribution to Gaussian distribution was suggested in the simulation. In addition, charge detection sensitivity was found to increase with the scanning height, showing much room for further improvement of the sensitivity in UHV nc-AFM. The limitation of the electrostatic model is also discussed, and some knowledge regarding the

charge distribution obtained from theoretical analysis and other experimental methods is suggested to be necessary supplements to the quantitative charge analysis by nc-AFM.

Finally, the approach used in the electrostatic simulation of nc-AFM was applied in 3D simulation of Si nanocrystal memory. The dependence of Coulomb charging energy on dielectric environment is analyzed. From the local variation of channel minority carrier density due to separated charge storage, the threshold number density of charged nanocrystals for 1D approximation to break down is shown to be 10^{12} cm^{-2} in the sample geometry investigated.

TABLE OF CONTENTS

Acknowledgements	iv
Abstract	vii
Table of contents	x
List of figures	xiii
Chapter 1: Introduction	1
1.1 The era of nanotechnology	1
1.2 Nanocrystals	2
1.3 Silicon nanocrystal floating gate memory	4
1.4 Scanning probe microscopy	7
1.5 Outline of the thesis	10
Chapter 2: Fabrication and characterization of Si nanocrystal memory	12
2.1 The ion implantation method for Si nanocrystal synthesis	12
2.2 Fabrication of Si nanocrystal memory	14
2.3 Structural characterization	14
2.3.1 TEM	16
2.3.2 AFM and RHEED	16
2.3.3 STM, nc-AFM, and RHEED	18
2.4 Electrical characterization	23
2.4.1 I-V	23
2.4.2 C-V	24
2.5 Optical measurements	28

2.6	Comparison between nanocrystal density and charge density	31
2.7	Summary	33
Chapter 3: Electronic properties of tunnel oxide layer in silicon nanocrystal memory . .		36
3.1	Introduction	36
3.2	Conductive atomic force microscopy	37
3.3	Morphology and current images	39
3.4	Quantitative analysis and discussion	42
3.5	Switching events	48
3.6	Summary	49
Chapter 4: Charge retention characteristics in Si nanocrystal doped SiO ₂ films		51
4.1	Introduction	51
4.2	Charge injection and imaging by conductive-tip noncontact AFM	53
4.3	Charging and discharging with electrons	59
4.4	Charging and discharging with holes	62
4.5	Control samples	64
4.6	Discussion and qualitative analysis	67
4.7	Quantitative charge analysis through electrostatic simulation	71
4.8	Temperature dependence	79
4.9	Summary	83
Chapter 5: Improved models for quantitative charge imaging by atomic force microscopy		
5.1	Introduction	85
5.2	Electrostatic model	86
5.3	Method of images algorithm for electrostatic simulation	89

5.3.1	Two and three dielectric layers	90
5.3.2	Method of images algorithm	93
5.3.3	Example	98
5.4	Effects of dielectrics and space charge in Si substrate	100
5.5	Charge detection sensitivity and lateral resolution	104
5.6	Vertical and lateral charge dissipation	106
5.7	Summary	107
Chapter 6:	Electrostatic calculation related to silicon nanocrystal memory device ...	109
6.1	Introduction	109
6.2	Coulomb charging energy	110
6.3	Variation of channel carrier density due to separated charge storage	113
6.4	Summary	117
Chapter 7:	Conclusions and future directions	118
7.1	Conclusions	118
7.2	Future directions	119
Bibliography	123
Appendix A:	Information related to Omicron UHV VT STM/AFM system	139
A.1	STM tip/AFM cantilever selection	139
A.2	Self-designed parts and explanation	140
Appendix B:	C++ codes for electrostatic calculation	143
B.1	Method of images algorithm	143
B.2	Quantitative charge imaging by nc-AFM	150
B.3	3D calculation of channel carrier density in nanocrystal memory	155

LIST OF FIGURES

1.1	Schematics of conventional floating gate memory and nanocrystal memory	5
2.1	Schematic of ion beam synthesis of Si nanocrystals	12
2.2	Schematic of nanocrystal samples and devices used in this project	15
2.3	Cross section TEM image of a nanocrystal memory device	17
2.4	Contact mode AFM image and RHEED pattern of half-etched SiO ₂ film containing Si nanocrystals	17
2.5	RHEED patterns of SiO ₂ , ‘nanocrystals’, and Si substrate	18
2.6	UHV STM image and RHEED pattern of Si nanocrystals	19
2.7.1	Non-contact mode AFM (nc-AFM) images of Si substrate with and without Si nanocrystals	21
2.7.2	Size distribution and size histogram of Si nanocrystals	22
2.8	Gate leakage characteristics of a nanocrystal floating gate MOS capacitor	24
2.9	C-V characteristics of a nanocrystal floating gate MOS capacitor	25
2.10	Capacitance decay measurements on a nanocrystal floating gate MOS capacitor	26
2.11	Capacitance decay measurements at elevated temperatures	27
2.12	Energy band diagrams during programming with holes and electrons	29
2.13	Energy band diagrams during electron retention and hole retention	29
2.14	Normalized PL spectrum of a nanocrystal sample at room temperature	30
2.15	Comparison between contact mode AFM image and UHV STM image of silicon nanocrystal clusters	32

3.1	Experimental setup for conductive AFM (C-AFM)	38
3.2	Surface morphology and simultaneously acquired current images of a half-etched Si nanocrystal sample ($V_{\text{tip}} > 0$)	39
3.3	Surface morphology and simultaneously acquired current images of a half-etched Si nanocrystal sample ($V_{\text{tip}} < 0$)	40
3.4	An explanation to the features observed in the current images	41
3.5	Local I-V characteristics	43
3.6	Histogram of current values in the current images at +3.52 V and -4.55 V	43
3.7	Cross section of nanocrystal distribution in the ‘nucleation and growth’ regime, and ‘spinodal decomposition’ regime with limited annealing time	46
3.8	Energy band diagrams for C-AFM with half-etched Si nanocrystal sample	47
3.9	I-V characteristics showing switching events and fluctuations	48
3.10	Schematic of current routes for electron tunneling through the SiO_2 film with Si nanocrystals	49
4.1	Schematics of charge injection and subsequent imaging by nc-AFM	54
4.2	Synthesis of the nanocrystal samples used in charge injection and imaging experiments	56
4.3	Schematic of the mechanism of charge injection with a biased AFM tip	57
4.4	Schematic of the charge dissipation mechanisms	58
4.5	3D view of nc-AFM images showing dissipation process of electrons in the ‘low dose’ sample	59
4.6	Series of line profiles showing the electron dissipation process	61

4.7	3D view of nc-AFM images showing dissipation process of holes in the ‘high dose’ sample	62
4.8	Series of line profiles showing the hole dissipation process	63
4.9	Series of line profiles showing dissipation process of holes in the control SiO ₂ sample without ion implantation	65
4.10	Series of line profiles showing dissipation process of holes in the control sample with Si ⁺ ion implantation but without thermal annealing	66
4.11	2D nc-AFM images showing change of protrusion shape in the dissipation of holes	68
4.12	Time dependence of peak height in the charge imaging of localized holes and electrons, re-plotted with logarithmic scale in either axis	69
4.13	The Energy band diagrams showing field-enhanced diffusion of holes	70
4.14	Experimental discharge time series and corresponding fits to the data	73
4.15	The cross sections of the charge distributions that fit experimental nc-AFM images	75
4.16	Number of detected holes in the nanocrystal layer as a function of time, and ratios of the hole number over nc-AFM profile peak height	77
4.17	Evolution of Gaussian charge distribution in the Si nanocrystal layer	78
4.18	Time dependence of the number of detected holes in the nanocrystal layer, re-plotted with logarithmic scale in either axis	80
4.19	Series of line profiles showing the hole dissipation process at 400 K	81
4.20	Series of line profiles showing the hole dissipation process at 500 K	82
4.21	Schematics of <i>n</i> -channel and <i>p</i> -channel Si nanocrystal memory	84

5.1	Electrostatic model for the charge imaging experiment by nc-AFM	86
5.2	Method of images for two dielectric layers with a planar interface	91
5.3	Method of images for three dielectric layers with two planar interfaces (I)	92
5.4	Method of images for three dielectric layers with two planar interfaces (II)	94
5.5	An example showing the application of method of images algorithm on a problem including three metallic spheres and four dielectric layers	99
5.6	Critical influence of dielectric environment on charge imaging by nc-AFM	101
5.7	Trivial influence of substrate space charge on charge imaging by nc-AFM	103
5.8	Minimum detectable number of basic charges as a function of the tip- sample spacing	104
5.9	Lateral resolution of nc-AFM when scanning two point charges ($30 q_0$ each)	105
5.10	Simulated nc-AFM images of a 2D Gaussian charge distribution that dissipates in three different ways	106
6.1	Influence of nanocrystal position and size in a memory device on Coulomb charging energy for adding the first basic charge	111
6.2	Coulomb charging energy lowering by using high- κ dielectrics	112
6.3	Local variation of electric potential distribution in the substrate showing the situation that 1D approximation starts to break down	114
6.4	Plan views of the channel minority carrier density of a nanocrystal floating gate memory showing the influence of discrete charge storage on turn on characteristics of the device	115

Chapter 1

Introduction

1.1 The era of nanotechnology

Nanotechnology is already a very popular word that frequently appears in mass media. Although this word still remains something of a mystery and a cause for confusion in the popular imagination, even without a clear and strict definition, nobody can deny that an era of nanotechnology is fast approaching. The concept of nanotechnology had its genesis in a lecture by Richard Feynman titled “There’s Plenty of Room at the Bottom”¹ given at the annual meeting of the American Physical Society held at California Institute of Technology in 1959, and the term was created in 1974 by Tokyo Science University professor Norio Taniguchi to describe precision manufacturing of materials at the nanometer scale.² Today the boom of nanotechnology is happening in a wide variety of disciplines, ranging from basic research areas such as chemistry, physics, and biology to application areas such as communication, energy, and medicine. At the same time, nanotechnology is blurring the boundaries between these disciplines.

In microelectronics, complementary metal oxide semiconductor (CMOS) technology has proven itself to be one of the most important achievements in modern engineering history and has become the primary engine driving the world economy. For more than 30 years, the continuous scaling of CMOS transistors predicted by the famous Moore’s law³ has been playing a key role in achieving higher performance and lower costs. With the appearance of 90 nm, 65 nm, and even 45 nm process technology, there is no “plenty of

room at the bottom” any longer before reaching the fundamental limits set by semiconductor physics and quantum mechanics. Novel ideas such as carbon nanotubes⁴ are presented as a possible substitute for transistor-on-silicon chips. However, until an idea can be proven practical in volume production and has advantages large enough to persuade manufacturers to abandon the dominating and mature CMOS technology, this technology is still our most dependable source for further miniaturization. In the meantime, more effort is needed to overcome issues such as overheating and power leakage. As Moore said, “No exponential lasts forever. But it can be postponed.”

1.2 Nanocrystals

Low dimensional materials, including nanowires, nanotubes, and nanocrystals, have attracted much attention in recent years. Nanocrystals typically contain a few tens to a few tens of thousands of atoms following crystalline structure, and their properties are usually quite different from bulk materials. Nanocrystals have very large surface-to-volume ratios, or a high percentage of atoms in the disordered surface region instead of the crystalline phase, which makes nanocrystals highly chemically active and unstable. For nanocrystals with the sizes of a few nanometers, quantum mechanical effects have to be considered when studying their optical and electronic properties. The quantized energy levels even make them behave like “artificial atoms,”⁵ so nanocrystals are also called “quantum dots.”

Semiconductor nanocrystals have shown potential applications in many areas. Their first practical use was found in biology as fluorescent probes in biological staining and diagnostics.^{6,7,8} Light emitting diodes (LEDs)^{9,10,11} and single electron transistors¹² based

on semiconductor nanocrystals as well as applications in optical amplifiers¹³ and lasers¹⁴ have been suggested.

Bulk silicon is an indirect bandgap semiconductor, making it an inefficient light emitter. However, the small sizes of silicon nanocrystals enable their properties to approach that of a direct bandgap semiconductor. Silicon nanocrystals have attracted a huge amount of interest since Canham's discovery of room temperature photoluminescence of porous silicon,¹⁵ which was attributed to quantum confinement. Since then, more research on light emission has been conducted using porous silicon,^{16,17,18,19} Si/SiO₂ superlattices,²⁰ and surface-textured bulk silicon,²¹ as well as silicon nanocrystals fabricated through electrochemical etching and dispersion,²² silicon ion implantation plus annealing,^{23,24,25} and annealing of SiO_x films prepared by plasma enhanced chemical vapor deposition.²⁶ Surface passivation was found to play an important role next to the size effect in tuning the band gap or emission wavelength.^{27,28} Although silicon nanocrystals are less optically efficient than many other nanocrystals formed by direct band gap semiconductors, their compatibility with CMOS processing and high quality of surface passivation with SiO₂ make them an ideal candidate for many applications in optoelectronics. The nanocrystal antenna effect found in Si nanocrystal-doped SiO₂ containing erbium,^{29,30,31} or a similar system,^{32,33} shows the ability to increase the effective Er absorption cross section by several orders of magnitude, and was explained theoretically by an energy transfer process from excitons in nanocrystals to surrounding Er ions.^{34,35} Since Er ions emit light at 1.55 μm, the wavelength for optical telecommunication, this effect may help to fabricate efficient LEDs, optical amplifiers, or even a silicon laser.

Silicon nanocrystal fabrication techniques have advanced enough to make it possible to obtain single electron charging effects even at room temperature, and have become a potential way to fabricate nanodevices which have feature sizes beyond the limit set by standard lithographic techniques. This would allow for future ultralow power and ultrahigh density integrated devices. One example is a single electron tunneling device that consists of nanocrystals which constitute active electron transport paths.^{36,37} Fabrication of the Si-nanocrystal-based single electron transistor was first demonstrated by Choi et al. using silicon nanocrystals deposited by low pressure chemical vapor deposition (LPCVD) in 1998,³⁸ and then by Fu et al³⁹ with a unique plasma deposition technique for Si nanocrystal deposition. In addition, the charge storage ability of Si nanocrystals was used to control Coulomb blockade oscillations in a single electron transistor structure.⁴⁰ More so than in tunneling devices, an immediate and more practical application of Si nanocrystals is in floating gate memory.

1.3 Silicon nanocrystal floating gate memory

The idea of silicon nanocrystal based memory was presented by Sandip Tiwari et al.⁴¹ in 1995. Figure 1.1 shows the schematic of this memory device as well as conventional floating gate memory. Both devices consist of a metal oxide semiconductor field effect transistor (MOSFET) structure and a floating gate which can store charges. Charges can be injected into or erased from the floating gate through a tunnel oxide layer under appropriate gate biases. The key difference exists in the formation of the floating gate, which is a continuous layer of polycrystalline silicon in the conventional version, but a layer of discrete Si nanocrystals embedded in SiO₂ matrix in the nanocrystal version.

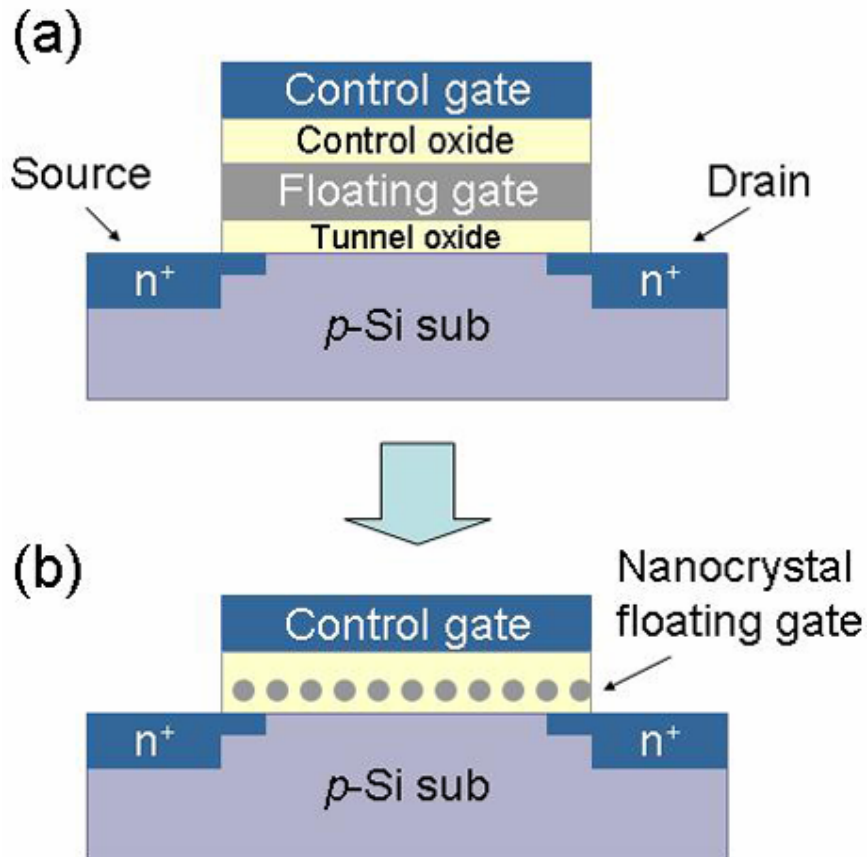


Figure 1.1. Schematic of conventional floating gate memory (a) and silicon nanocrystal floating gate memory (b).

Nanocrystal memory has many advantages over conventional floating gate memory due to the separated charge storage. As conventional flash memory devices begin to scale into the sub-100 nm lithography regime, scaling is becoming more challenging especially due to the stringent leakage requirements. For example, one leaking path that connects the channel and the continuous floating gate can dissipate all the stored charges and ruin the whole device. The leakage issue has imposed fundamental scaling limitations on physical thickness of the tunnel oxide as well as further scaling of the memory devices (transistors generally need to scale proportionally to avoid short-channel effects.) The tunnel oxide thickness in the conventional floating gate memory device is typically larger

than 8 nm, which requires high operation voltages for programming and erasing. Since 8 nm is in the Fowler-Nordheim tunneling region, defects can be generated by many rounds of electrical stress and degrade the tunnel oxide. In nanocrystal memory, the stringent leakage requirements do not exist. A leaking path can only discharge one or a few nanocrystals, but the charges on all other nanocrystals will still be there, and the memory device will still work. With this feature, nanocrystal memory devices can be further scaled and tunnel oxide thickness can be less than 3 nm. Decrease of tunnel oxide thickness brings lower operation voltages and lower power consumption, which alleviates heat dissipation problems. The mechanism of charging and discharging is direct tunneling, which has little influence on the oxide quality and helps to increase the number of operation cycles. In addition, Si nanocrystal memory can be fabricated using simple methods fully compatible with mainstream semiconductor processing and avoid the fabrication complications and costs of a dual-poly process.

The advantages of Si nanocrystal memory have attracted much attention, and research on this topic has boomed in the last ten years. Various fabrication processes have been suggested for nanocrystals in nanocrystal memory. One important process is the excess Si-precipitation technique, which uses high-energy ion implantation of Si into the SiO₂ layer⁴² or deposition of a Si-rich SiO₂ layer, followed by thermal annealing at high temperature to precipitate Si nanocrystals. Other methods include the aerosol technique, which can deposit Si nanocrystals with a SiO₂ shell,⁴³ and LPCVD, which grows hemispherically shaped Si islands,^{44,45} etc. In 2003, De Salvo et al. demonstrated up to a 1 Mbit test array,⁴⁶ and Motorola declared a 4 Mbit nonvolatile memory,⁴⁷ raising hope for commercialization. In addition, Si nanocrystal memories fabricated on silicon-on-

insulator substrate have shown single electron charging and discharging phenomena at room temperature,^{48,49} and experimental evidence has been presented which supports the possibility of achieving dual bit operation.⁵⁰

In spite of all these advantages and promising developments of Si nanocrystal memory, there are still many challenges ahead on the road to commercialization. According to Jan De Baluwe,⁵¹ part of the voltage gain benefit from a thinner tunnel oxide layer is offset due to poor control gate coupling. Also, both the nominal and statistical retention behavior still need to be tested before claiming true nonvolatility, and a more fundamental understanding of the scaling limits of nanocrystal memories is still lacking. For example, control of the channel conductance when relying on only a few nanocrystals is still unknown. After all, Si nanocrystal memory has not fundamentally changed the constraints of transistor charge based memory scaling;⁵² it is an improved version rather than a brand new substitute for the current mainstream floating gate storage.

1.4 Scanning probe microscopy

Scanning Tunneling Microscopy (STM) was invented by Gert Binnig and Heinrich Rohrer in 1981.⁵³ Five years later, atomic force microscopy (AFM) was invented.⁵⁴ These inventions made it possible to not only take photos of individual atoms, but to actually move a single atom around.⁵⁵ Based on similar principles, various scanning probe microscopy (SPM) techniques were developed, including non-contact atomic force microscopy (nc-AFM); tapping-mode atomic force microscopy;^{56,57} Kelvin probe or electrostatic force microscopy (EFM);^{58,59} scanning capacitance microscopy (SCM);⁶⁰

piezoelectric force microscopy (PFM); magnetic force microscopy (MFM); and near-field scanning optical microscopy (NSOM); etc. SPM techniques have become powerful tools in surface science, materials science⁶¹ and even biological research,^{62,63} providing not only high-resolution surface morphology information but also local electrical,⁶⁴ mechanical,⁶⁵ magnetic, and optical properties.^{66,67} In addition, SPM can be used to watch dynamic processes^{68,69} and fabricate nanometer-sized patterns.^{70,71}

SPM is our main tool in the study of Si nanocrystals and Si nanocrystal memory devices. We used STM to characterize nanocrystal sizes and areal density, conductive AFM to study morphology and electron tunneling through the tunnel oxide, and nc-AFM to inject charges into the nanocrystal layer and monitor charge dissipation in real time. Three AFM systems were employed: an ambient AFM operated at room temperature (Park Scientific Autoprobe CP), a low temperature (down to 5 K) UHV STM (Omicron Nanotechnology), and a variable temperature (25 K to 1500 K) UHV STM/AFM (Omicron Nanotechnology). The first two were primarily used to perform structural characterization, while the latter was used for both structural and electrical characterizations.

The principle of STM is quite simple, and can be compared with that of an old-fashioned record player since they both use a sharp needle (or tip) to interrogate the surface; in STM, however, the tip does not touch the surface of a sample. Typically, a nearly constant distance (within 1 nm) between the tip and the sample is maintained during scanning. To achieve this purpose, a bias voltage is applied between the tip and sample surface, and feedback electronics control the vertical movement of the tip (or the sample) with a piezoelectric element to maintain a constant tunneling current (a few pA

to a few nA). The vertical movement is recorded and corresponds to the morphology of the sample surface. Since current is the monitored parameter, STM generally requires conductive samples such as metals or semiconductors (e.g., highly doped silicon). However, this requirement has become less important with the continuously increasing sensitivity of electrical current detection in recent years, and even insulators have become possible objectives of STM.

Contact mode AFM was developed soon after STM and was designed to be able to work on insulators. In the mainstream AFM system, a tip with a typically 15 nm radius of curvature is attached to a microscale cantilever with a low spring constant. The AFM tip gently touches the sample surface and the bending of the cantilever is detected, often with a laser beam reflected from the cantilever. The AFM measures contours of constant force (repulsive or attractive) rather than tunneling current. The forces are usually set in the nanoNewton range or are even smaller, depending on the hardness of the sample surface and the tip material, to avoid damage to the tip and the sample.

In nc-AFM, a much stiffer cantilever is excited to oscillate at high frequency (several hundred kHz), and the tip does not touch the sample surface. Only long-range interactions remain and can be detected from the changes to cantilever oscillation. The relevant forces include van der Waals interactions, electrostatic and magnetostatic interactions, and the force due to formation of liquid capillaries under ambient conditions. The most commonly used detection method for ambient nc-AFM is generally called 'slope detection'. Generally, when the tip is brought close to the sample surface, the emergence of tip-sample interactions can affect the oscillation as if the cantilever has a

modified spring constant, and results in a shift in the resonant frequency, and a drop in the oscillation amplitude if the cantilever is driven at a fixed frequency.

In UHV nc-AFM, an alternative method called frequency modulation (FM) is used. The oscillation frequency of the cantilever instantaneously follows its resonant frequency, which changes with force gradient. During scanning, the feedback electronics directly maintain a preset oscillation frequency that is a little (several tens or hundred Hz) smaller than the resonant frequency before approaching the tip to the sample. A constant frequency shift is roughly equivalent to a constant force gradient, or a constant average tip-sample spacing if there is only van der Waals force between the tip and the sample surface. Since there is almost no air damping in UHV, a Q value as high as 10^5 or more can be obtained, compared with less than 100 for ambient AFM. Therefore a UHV nc-AFM has much higher sensitivity. See chapter 5 for more details on the principle of UHV nc-AFM.

1.5 Outline of the thesis

The work described in this thesis focuses on characterization of Si nanocrystal memory with nanocrystals synthesized by the ion implantation method. It aims to improve charge retention characteristics and explore the space for further device scaling.

Chapter 2 describes fabrication, structural, and electrical characterization of Si nanocrystal memory devices. The sizes and areal density of the tiny Si nanocrystals were characterized by STM, non-contact AFM, and RHEED. The memory effects were demonstrated by C-V measurements. Special attention was paid to the relationship between nanocrystal density and charge density.

Chapter 3 investigates the electronic property of the tunnel oxide layer, which is closely related to charge retention. From the overall high conductance between nanocrystal floating gate and channel found by conductive contact mode AFM, the formation and distribution of nanocrystals in the tunnel oxide layer are discussed. A better control of nanocrystal distribution is shown to be necessary for a true nonvolatile memory.

Chapter 4 is the central part of the thesis. Nanoscale charge retention characteristics of both electrons and holes in the nanocrystal layer were obtained by using an UHV conductive-tip non-contact AFM to inject charges into nanocrystals and monitor subsequent charge dissipation. Quantitative information regarding total charge, charge distribution, and evolution was extracted from the time-dependent non-contact AFM images through electrostatic simulation. Enlightened by the superior retention characteristics of holes, a *p*-channel nanocrystal memory working with holes is presented as an interesting choice.

Chapter 5 provides the details of the electrostatic simulation of charge imaging by non-contact AFM. The effect of dielectric environment was included in the simulation with the method of images algorithm, and proved to be critical. Theoretical issues such as charge detection sensitivity and limit of the electrostatic simulation are also discussed.

In Chapter 6, the approach used in Chapter 5 was applied in 3D electrostatic simulation of nanocrystal memory. Coulomb charging energy and local variation of channel minority carrier density were calculated and analyzed.

Based on the conclusions drawn in Chapter 7, future directions of this research are discussed and complementary experiments suggested.

Chapter 2

Fabrication and characterization of Si nanocrystal memory

2.1 The ion implantation method for Si nanocrystal synthesis

Shortly after the discovery of strong visible photoluminescence in porous silicon, Si nanocrystals were fabricated by Si^+ ion implantation into silica.⁷² Among the various techniques mentioned in chapter 1, ion beam synthesis has become a popular one because of its important manufacturing advantages that are fully compatible with the complementary metal oxide semiconductor (CMOS) technology. This technique is briefly

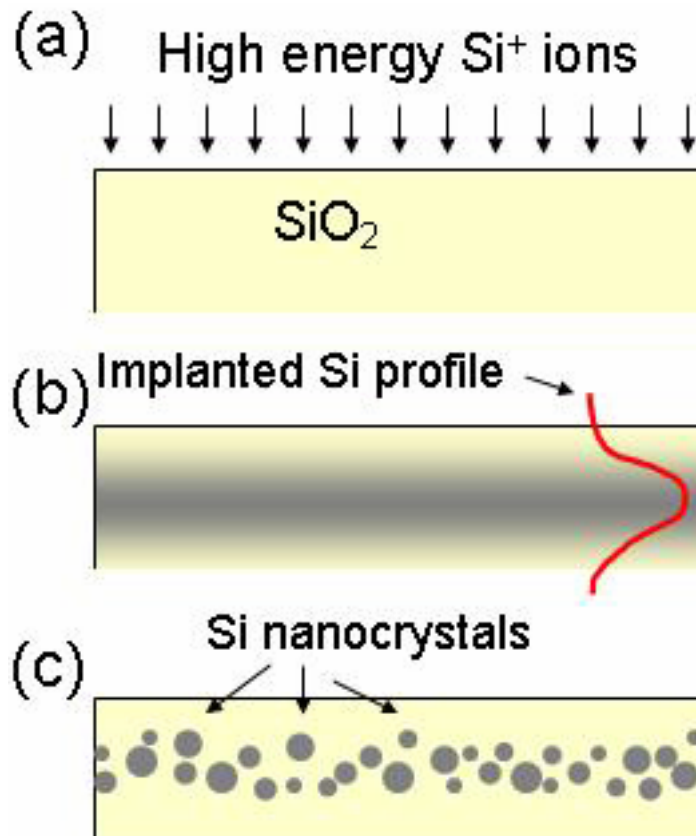


Figure 2.1. Schematic of ion beam synthesis of Si nanocrystals. (a) Si^+ ion implantation into silica. (b) Solid state supersaturation of Si near the surface. (c) Implanted Si is precipitated into discrete Si nanocrystals, usually by thermal annealing.

described in Figure 2.1. Silica is injected with energetic Si^+ ions that are accelerated from a few kilovolts to a few thousands kilovolts. High dose implantation can create a solid state supersaturation of Si in a layer extending from the specimen surface to a depth of a few nanometers to a few hundred nanometers. Subsequent thermal annealing induces the implanted Si to precipitate and form discrete nanoparticles. The nanocrystal spatial distribution, density, and sizes can be controlled by varying the implantation dose, dose rate, and energy, as well as post-implantation annealing conditions such as temperature, time, and annealing environment. Moreover, the ion implantation technique is now widely employed in the semiconductor industry and is well established in the commercial synthesis and processing of materials with microscopic precision and control.⁷³ These advantages make the ion implantation technique an ideal approach for making Si nanocrystals for memory device applications.

The employment of separated silicon nanocrystals as charge storage nodes in floating gate memory makes it possible for further device scaling with current silicon techniques. The prospect is largely due to the extremely small sizes of nanocrystals fabricated through ion implantation synthesis and other methods which are well below the feature size achievable by e-beam lithography. It is essential to control Si nanocrystal size, depth distribution, and areal density as accurately as possible. However, structural characterization of these small Si nanocrystals embedded in SiO_2 via transmission electron microscopy (TEM) is usually difficult and fails to correctly resolve nanocrystal size and density. In this chapter we demonstrate that ultrahigh vacuum scanning tunneling microscopy (UHV STM) / noncontact atomic force microscopy (nc-AFM) enables a much more accurate measurement of the ensemble size distribution and array

density for small Si nanocrystals in SiO₂. In addition, reflection high energy electron diffraction (RHEED) further verifies the existence of nanocrystallites in SiO₂. The results obtained from both structural and electrical characterization are combined for a complete analysis of nanocrystal floating gate memory devices made via Si ion implantation.

2.2 Fabrication of Si nanocrystal memory

The major fabrication steps of our Si nanocrystal memory were performed at Intel Corporation using 300 mm processing equipment. First, 15 nm of dry oxide was grown on *p*-type silicon substrate with a doping concentration of $3 \times 10^{18} \text{ cm}^{-3}$. Then the samples were implanted with 5 keV Si⁺ ions to a fluence of $1.27 \times 10^{16} \text{ cm}^{-2}$, followed by rapid thermal annealing at 1080 °C for 5 minutes in an atmosphere containing 2% O₂ to allow formation of Si nanocrystals [Fig. 2.2(a)]. To form transistor structures, polysilicon gate and source/drain regions were defined and then doped with blanket implantation [Fig. 2.2(b)]. In addition, some metal-oxide-semiconductor structures [Fig. 2.2(c)] were formed by depositing 80-nm-thick gold with mechanical masks on the front side and 50-nm-thick gold on the backside (with oxide removed), and thermally annealing at 200 °C for 30 minutes.

2.3 Structural characterization

After the fabrication of nanocrystal samples and nanocrystal memory devices, it is important to know whether the fabricated structures match the designs. Since the nanocrystal floating gate is the key part governing charge storage and memory

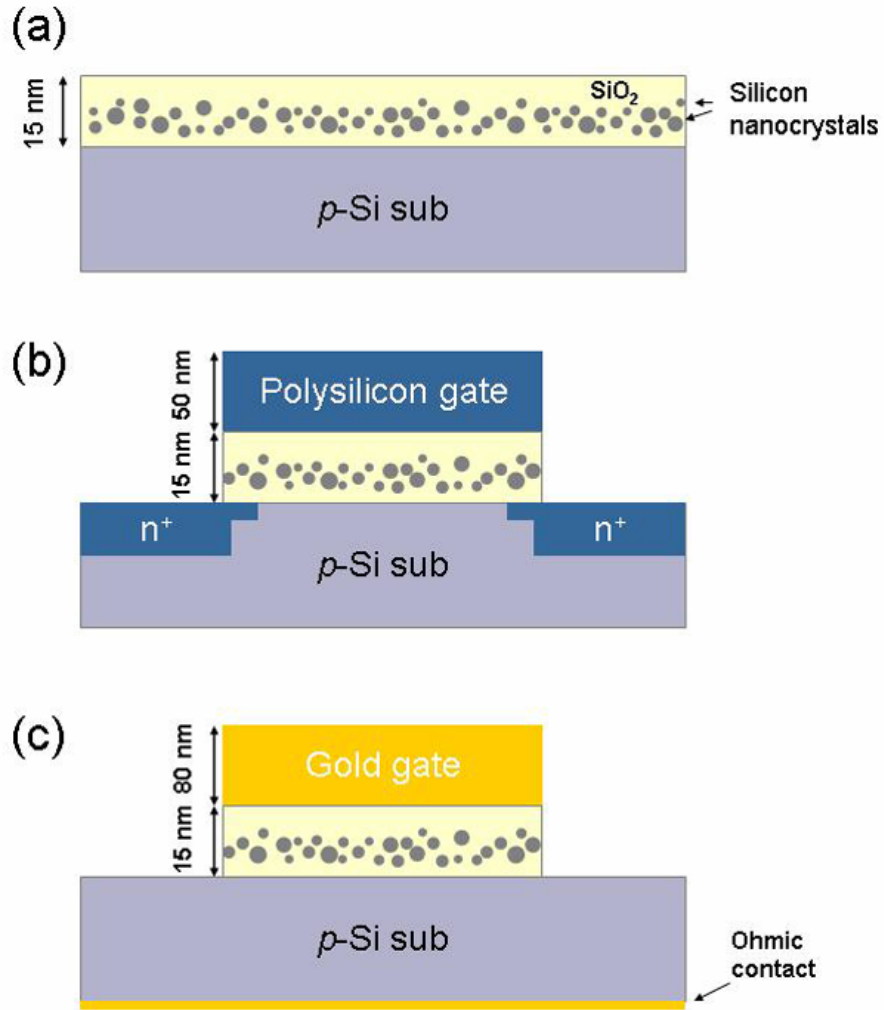


Figure 2.2. (a) Nanocrystal sample fabricated by Si⁺ ion implantation (5 keV , $1.27 \times 10^{16} \text{ cm}^{-2}$) followed by rapid thermal annealing ($1080 \text{ }^\circ\text{C}$, 5 min , $98\% \text{ Ar} + 2\% \text{ O}_2$). (b) A nanocrystal floating gate memory device. Various combinations of channel length and channel width were chosen, with channel length varying from 1 mm to $1 \text{ }\mu\text{m}$ and channel width varying from 1.5 mm to $3 \text{ }\mu\text{m}$. (c) MOS with nanocrystals. The diameter of gold gate varies from 0.4 to 0.7 mm .

characteristics, it is especially important to find out whether Si nanocrystals were formed in the SiO₂ matrix, and if so, what the areal density is and what nanocrystal sizes are.

2.3.1 TEM

Transmission electron microscopy (TEM) is the most popular tool to characterize microstructures. It has been successfully used to characterize nanocrystal size and distribution with high resolution,^{43,73,74,75} and sometimes electron diffraction is used to further substantiate the existence of crystallites;⁷³ this is why TEM was tried first.

Figure 2.3 shows the cross-sectional high resolution TEM image of a nanocrystal memory device. The polysilicon gate, 15 nm SiO₂ layer and single crystalline (100) Si substrate can be clearly seen. However, the image does not clearly reveal individual Si nanocrystals. In addition, electron diffraction is unable to confirm the existence of a crystalline Si phase in the SiO₂ layer. We attribute this result to the small sizes of nanocrystals and electron scattering by the surrounding amorphous SiO₂ matrix. Due to the small *Z* contrast between Si and SiO₂, it is hard to detect Si nanocrystals with electron microscopy at sizes below approximately 2 nm.

2.3.2 AFM and RHEED

AFM and RHEED were used to characterize nanocrystal samples etched approximately halfway through the SiO₂ layer with buffered hydrofluoric acid [Fig. 2.4(a)]. The inset of Fig. 2.4(b) shows the RHEED pattern. The continuous background from amorphous SiO₂ confirms that the sample was etched only halfway down. Compared with the pattern from a control sample with pure SiO₂ under the same experimental conditions [Fig. 2.5 (a)], it is slightly different because at least one bright ring can be noticed. After digitally subtracting the diffraction pattern of the control

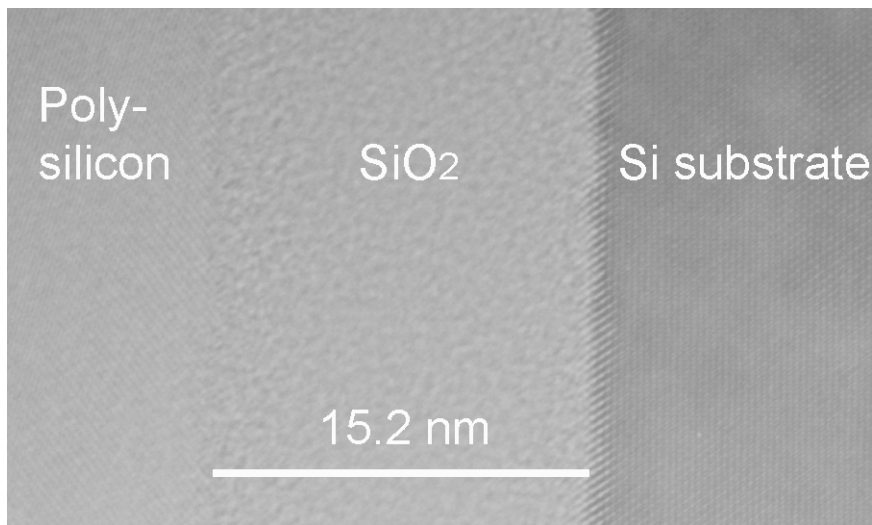


Figure 2.3. Cross-sectional TEM image of the polysilicon/SiO₂/Si structure in the nanocrystal floating gate memory device. Individual Si nanocrystals are not revealed.

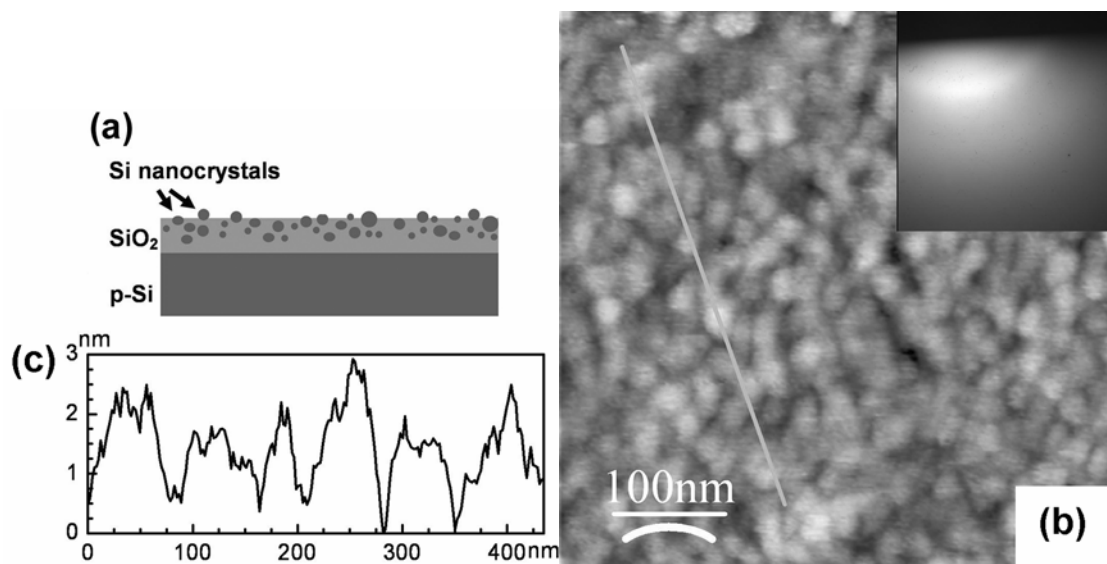


Figure 2.4. (a) Schematic of the half-etched SiO₂ film containing Si nanocrystals. (b) AFM image (contact mode, 500 nm × 500 nm). Inset shows the corresponding RHEED pattern. (c) Cross section along the line indicated in (b).

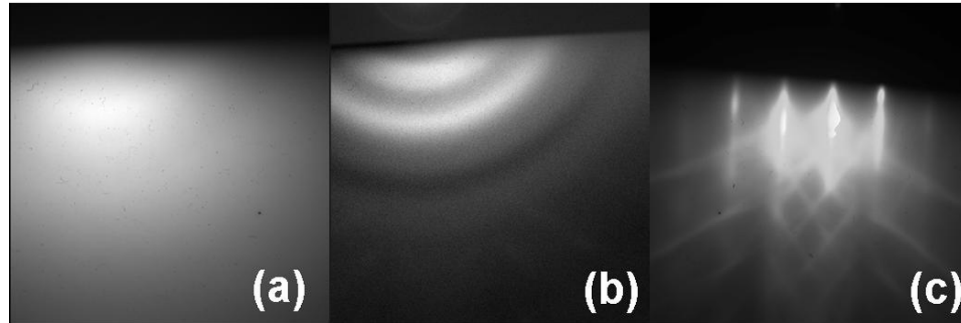


Figure 2.5. (a) RHEED pattern of SiO₂ film without Si nanocrystals. (b) The pattern obtained by digitally subtracting (a) from the inset of Figure 2.4(b). (c) RHEED pattern of Si substrate.

sample from the diffraction pattern of the half-etched sample, more rings could be found [Fig. 2.5 (b)]. These rings may indicate the existence of Si nanocrystals with random crystalline orientations. Figure 2.4 (b) shows contact mode AFM images with a 0.5 μm field of view. A surface variation of around 3 nm [Fig. 2.4 (c)] was observed in the AFM image and attributed to the existence of Si nanocrystals. If this result is used, a nanocrystal areal density of $1.6 \times 10^{11} \text{ cm}^{-2}$ can be estimated. This is an underestimated value because the tip size is much larger than the nanocrystal sizes, and so the observed “particles” in the images are in fact clusters of dozens of nanocrystals,⁷⁶ as verified by STM measurement on a fully etched sample.

2.3.3 STM, nc-AFM and RHEED

STM is a better tool for evaluating quantitative data such as nanocrystal sizes and densities. Millo et al. have used STM to characterize CdSe and InAs quantum dots on Au.^{77,78} STM measurements of Si nanocrystals fabricated by low pressure chemical vapor deposition⁷⁹ and nanocrystalline silicon films obtained by boron implantation of amorphous Si layers⁸⁰ have also been reported.

In our case samples have to be etched with buffered hydrofluoric acid to completely remove SiO_2 , leaving Si nanocrystals terminated with hydrogen and adhering directly on the Si substrate [Fig. 2.6(a)]. Within several minutes after etching, the samples were loaded into the chamber of a UHV STM. The vacuum inside the chambers was kept at 1×10^{-10} Torr to avoid further oxidation of the Si. Figure 2.6(b) shows the resolved Si nanocrystals in a cluster. The lateral dimension of the image is 50 nm. The sizes of the particles are quite uniform in this area, with the smallest interparticle distance of about 3 nm [Fig. 2.6(c)]. Based on this information, the upper bound on the size of the nanocrystals is about 3 nm. The areal density of the nanocrystals is measured to be around $4 \times 10^{12} \text{ cm}^{-2}$, 25 times higher than the result from contact mode AFM.

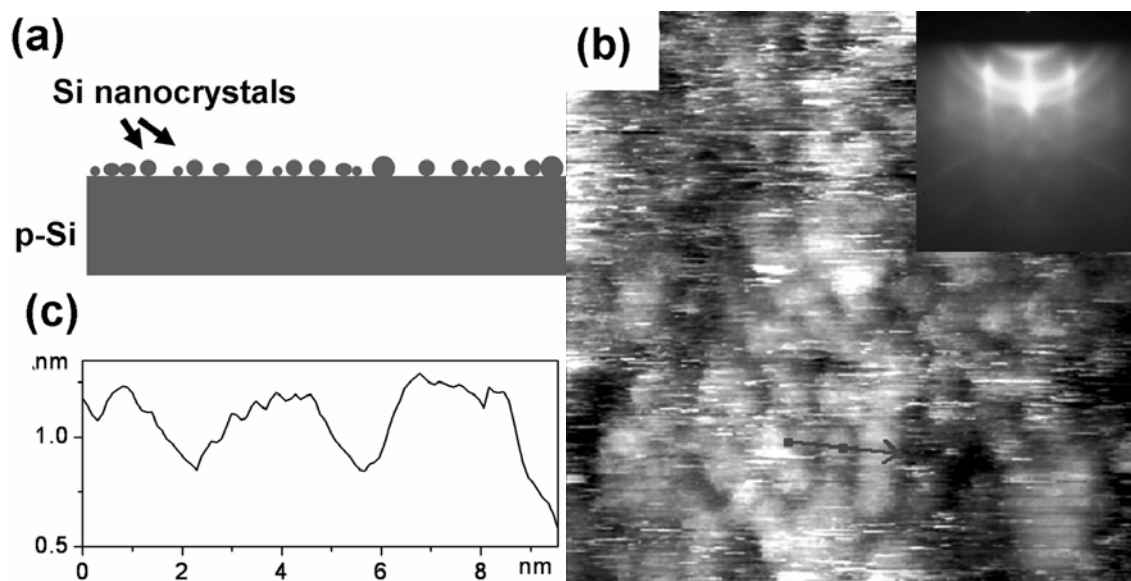


Figure 2.6. (a) Schematic of Si nanocrystals sitting on Si substrate. (b) STM topography image ($50 \text{ nm} \times 50 \text{ nm}$). Inset shows the corresponding RHEED pattern. (c) Cross section along the arrow in (b).

Considering the loss of nanocrystals during the etching process, this value is still a lower bound. The inset of Figure 2.6(b) shows the RHEED pattern. Note that diffraction spots and Kikuchi lines from the single crystal substrate and diffraction rings from nanocrystals can clearly be seen, while the pattern of the control sample does not contain diffraction rings [Fig. 2.5(c)]. The clear rings in the diffraction pattern of the fully etched sample also show that the observed nanoparticles in STM images are crystalline.

Figure 2.7.1(a) shows nc-AFM images of Si nanocrystals on Si substrate. Because of tip convolution effects, the lateral sizes of nanocrystals are usually amplified in their scan profiles. But the vertical sizes can be obtained accurately if the density of nanocrystals is sufficiently low. For this purpose, the sample was placed in an ultrasonic bath after etching to remove most of the nanocrystals that adhere to the surface of the Si substrate. About 80 Si nanocrystals can be clearly identified in Figure 2.7.1(a). The scale bar shows that the vertical sizes of the nanocrystals in the image vary from about 1 nm to more than 3 nm. It should be noted that the surface of the Si substrate without Si nanocrystals is quite flat [Fig. 2.7.1(b); the r.m.s. roughness is less than 1 Å], which makes it possible to measure the vertical sizes of individual nanocrystals with high accuracy. 83 nanocrystals in the image were measured. The histogram, as well as accurate size distribution of these nanocrystals, is shown in Figures 2.7.2(b) and 2.7.2(c), respectively. The arithmetic mean size is about 2.4 nm, and the r.m.c. (root mean cube) value is 2.5 nm.

However, the nanocrystal size distribution may have been shifted to smaller values because relatively small nanocrystals have a large chance to survive the ultrasonic bath. On the other hand, we may have missed some very tiny nanocrystals in the cluster, especially if they were surrounded by large nanocrystals, in which case the nanocrystal

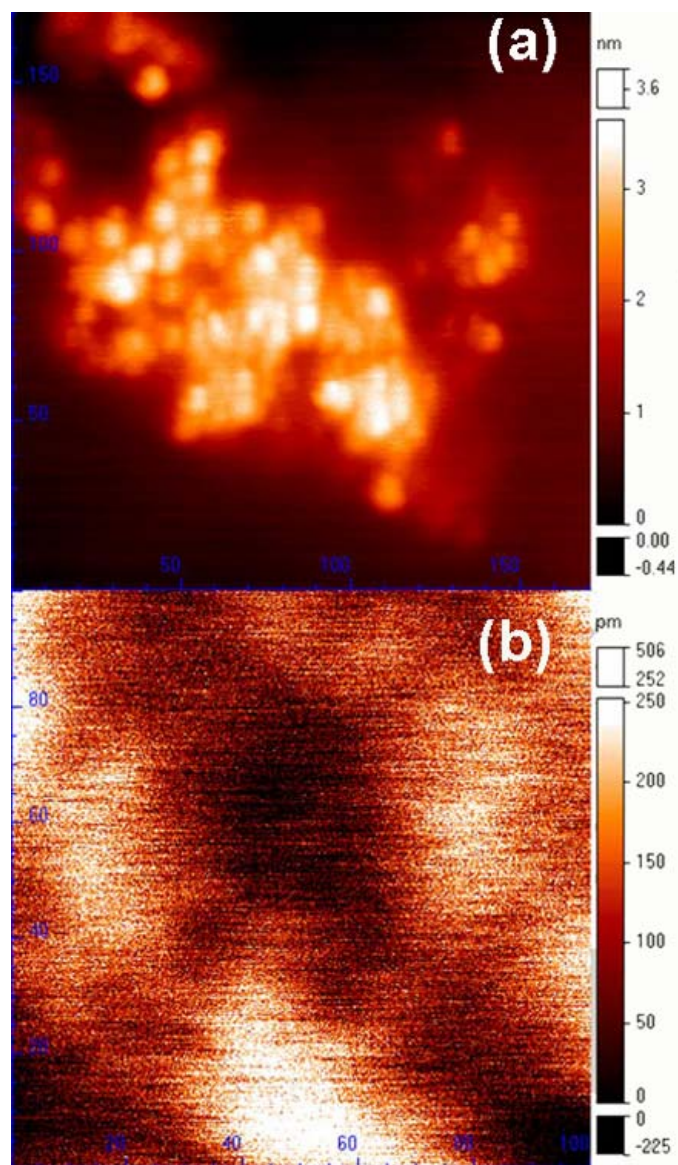


Figure 2.7.1. (a) Non-contact AFM image ($170 \times 170 \text{ nm}^2$) of Si nanocrystals on Si substrate. (b) Non-contact AFM image ($100 \times 100 \text{ nm}^2$) of Si substrate without Si nanocrystals. The surface roughness (r.m.s.) is 0.084 nm.

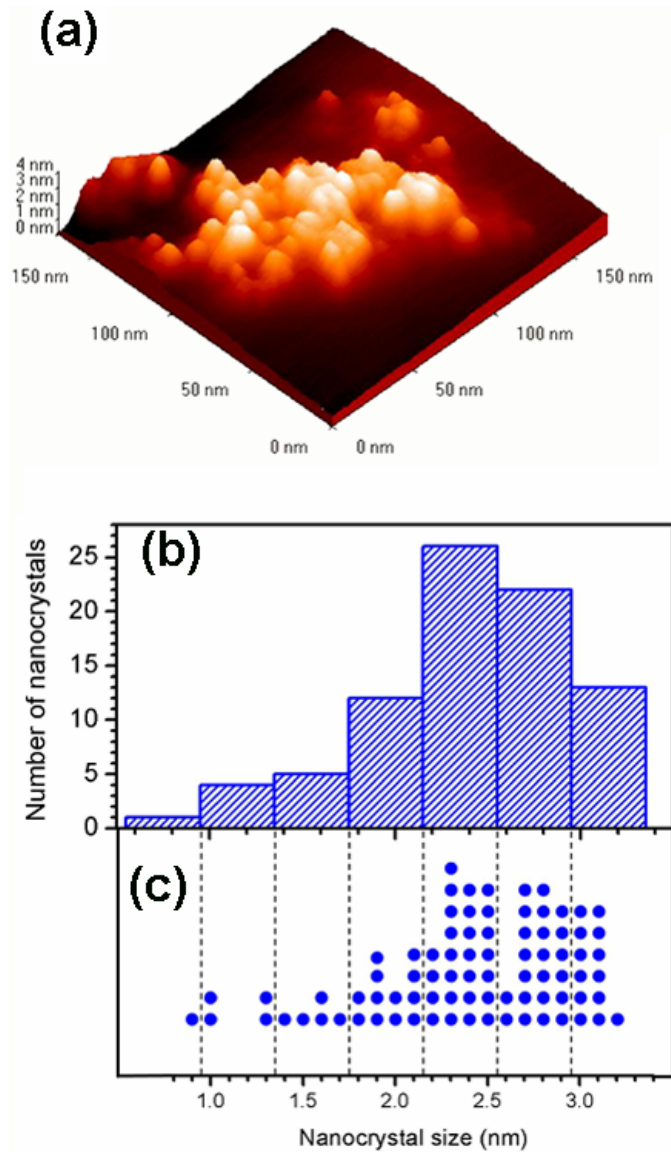


Figure 2.7.2. (a) 3D view of the non-contact AFM image shown in Figure 2.7.1(a). (b) and (c) are the histogram and distribution, respectively, of Si nanocrystal sizes based on the measurements of the 83 Si nanocrystals in (a).

size distribution may have been shifted to bigger values. As to the groove in Fig. 2.7.2(c), we believe it is nothing but a fluctuation which may happen when the statistical sample is not large enough. Although a few uncertainties exist, the nc-AFM results provide a clear view of the size distribution of nanocrystals fabricated through ion implantation.

2.4 Electrical characterization

Electrical characterization determines directly whether a device works and how well it works. We probed gate leakage characteristics (I_g vs. V_g), subthreshold characteristics (I_{sd} vs. V_g), and output characteristics (I_{sd} vs. V_d) of the nanocrystal floating gate transistors. Because no metal pads were deposited on the 50-nm-thick polysilicon gate in order to allow optical measurements, the probe sometimes punched through the gate, and a good electrical contact between the probe and the gate was not always established. Although memory effects were identified in some experiments, stable and repeatable results were very hard to achieve. We thus switched to the structure of MOS with nanocrystals [Fig. 2.2(c)] to evaluate the memory device operations. Current-voltage (I-V) and capacitance-voltage (C-V) measurements were made on these MOS capacitors with diameters ranging from 0.4 to 0.7 mm. Retention characteristics were obtained with capacitance decay measurements.

2.4.1 I-V

I_g - V_g measurements were performed with a Keithley 236 source measure unit. It was found that the flatband voltage for all fresh MOS capacitors were very close to the theoretical value (-0.15 V)⁸¹ for Au/SiO₂/p-Si. An overall high leakage problem was observed for all devices, with a difference of 3 orders of magnitude among them. Figure 2.8 shows the I_g - V_g curves of the leakiest device scanned in both directions. The gate leakage is about 0.05 A/cm² at ± 8 V, which is very high considering the total oxide thickness is 15 nm. According to the calculation using TRIM, the Si ion implantation profile has a very broad peak, with the maximum at the depth of about 10 nm. The broad

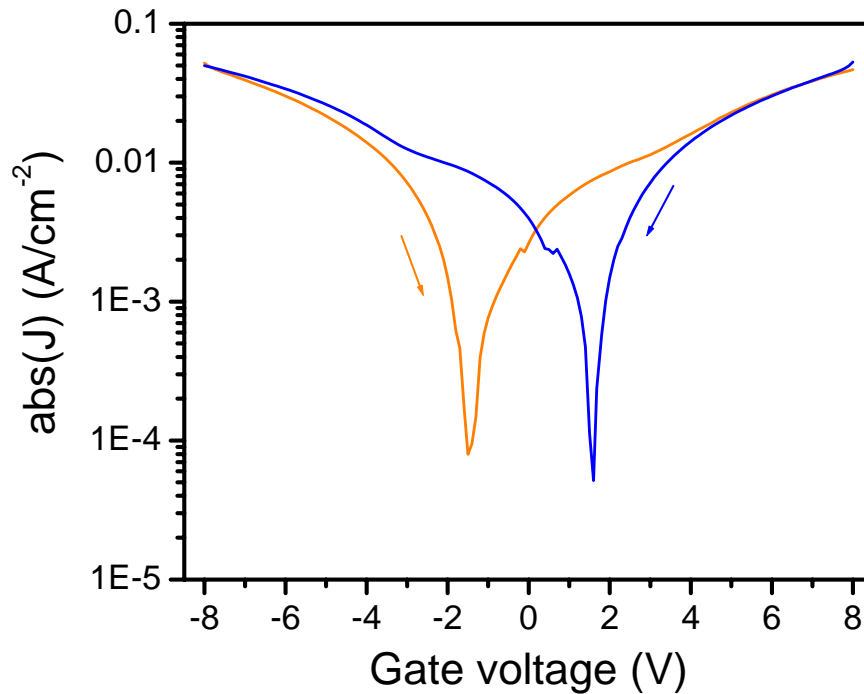


Figure 2.8. Gate leakage characteristics of a nanocrystal floating gate MOS capacitor. $V_{\text{step}} = 0.1$ V, delay = 1 s.

distribution of Si nanocrystals and Si related defects in SiO_2 is responsible for the high leakage problem. A hysteresis with more than a 3 V shift was observed and shows charge storage in the Si nanocrystal floating gate.

2.4.2 C-V

C-V measurements were performed with a Keithley 590 C-V analyzer to analyze charging and discharging phenomena. Figure 2.9 shows C-V hysteresis curves at 1MHz with various scan ranges of gate bias. In the experiment, fresh MOS devices were first scanned between -1 and +1 V (± 1 V scan), and no hysteresis was found, indicating no charging or discharging. The observed flatband voltage was very close to the theoretical

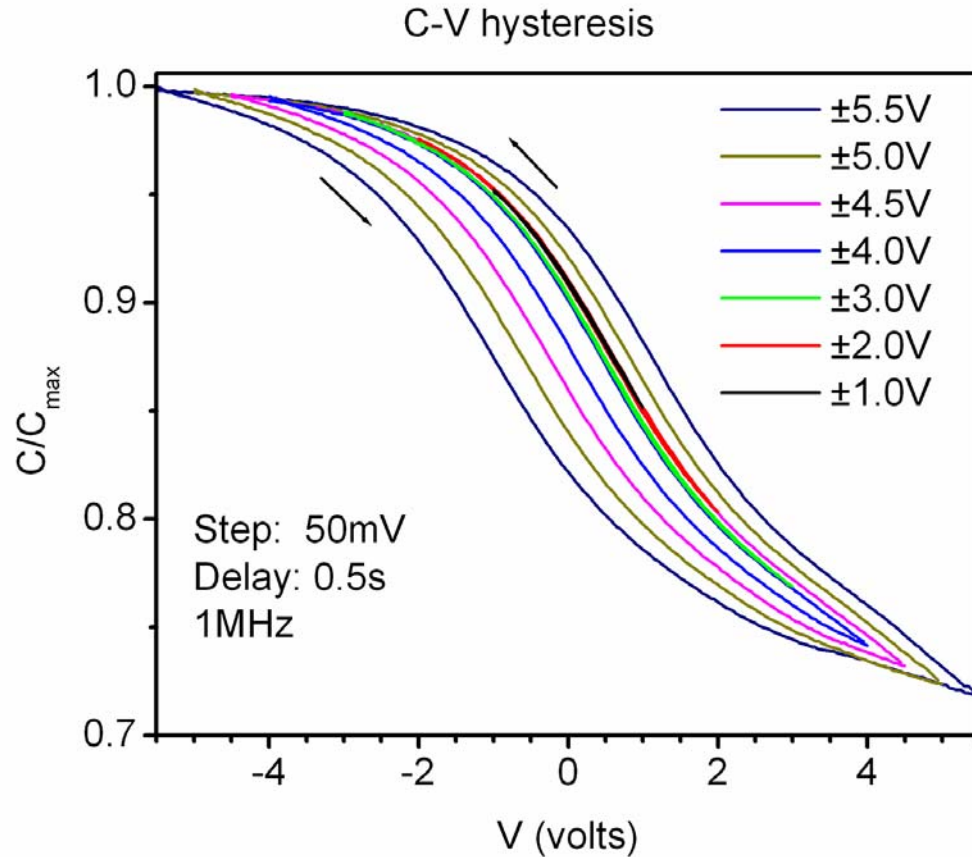


Figure 2.9. C-V characteristics of a nanocrystal floating gate MOS capacitor, obtained by sweeping gate voltage back and forth between different biases. For example, ± 1 V indicates that gate voltage is swept between -1 and +1 V. Measurements were performed with ascending order of sweeping ranges.

value of -0.15 V. The same happened for ± 2 V scan. There were still no hysteresis in the ± 3 V scan, but the curve shifted to the left by a small amount, indicating charging of holes into the floating gate but no erasing at positive voltages. In the subsequent ± 4 V scan, erasing of holes lead to the appearance of hysteresis. Due to partial erasing, the right edge of the C-V curve was still to the left of initial curves of the ± 1 V scan and ± 2 V scan until the positive voltage was large enough for complete erasing, which occurred at 4.5 V. After that, both hole charging and electron charging of the floating gate could be observed, resulting in wider and wider hysteresis loops.

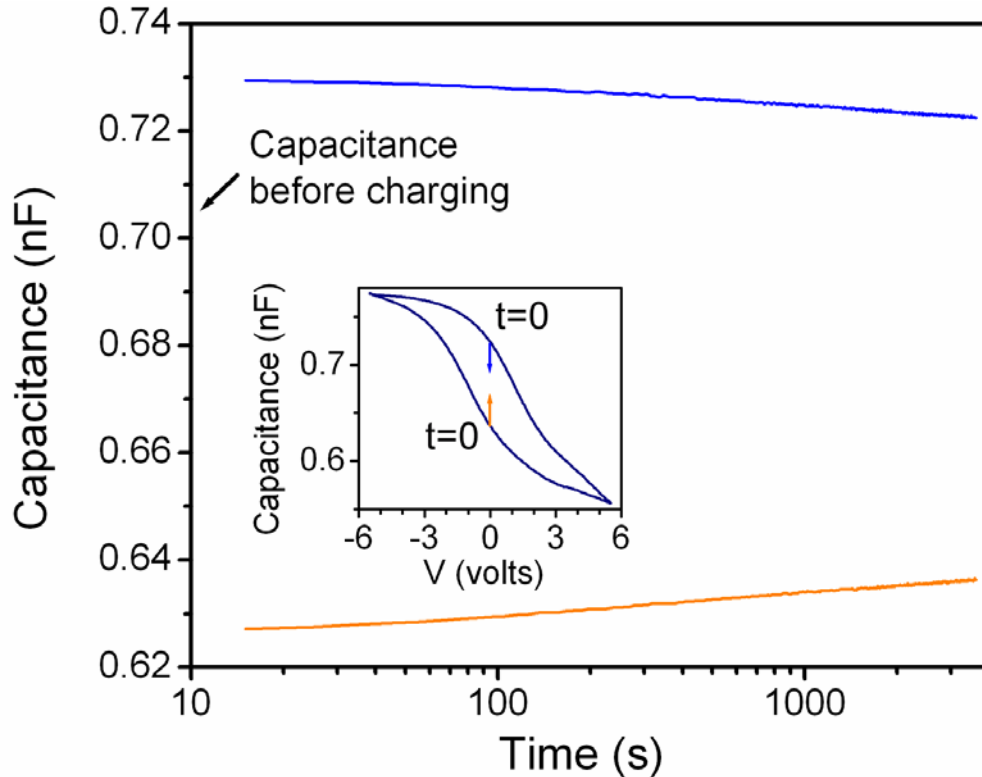


Figure 2.10. Capacitance decay measurements at $V_G=0$ on a nanocrystal floating gate MOS capacitor after charge injection at +5.5 V (blue curve) and -5.5 V (orange curve). The inset indicates the corresponding discharge.

The retention times were obtained with capacitance decay measurements at 0 V after the MOS capacitor was charged at +5.5 and -5.5 V, respectively (Fig. 2.10). In this range the capacitance changes approximately linearly with voltage shift, which is proportional to the areal density of stored charges. Capacitance shift can thus be an indication of charges left in the floating gate. Logarithmic dependence on time was observed, as has been reported elsewhere.^{45,82} This is also consistent with the leakage current decay measurement at 0 V, which shows a $1/t$ dependence on time. After charging at ± 5.5 V, the estimated time to lose 30% of holes is about 10^4 hours, while it is about 1 hour for electrons.

Capacitance decay measurements were also performed at high temperatures by controlling an electrical heating element with cooling water flow embedded in the probe station. However, the increase of temperature caused an increase in noise, and device failure was much more common. Stable results were only obtained below 100 °C [Fig. 2.11]. Although the data is quite noisy, an increased charge dissipation rate with temperature can be noticed, especially for holes.

In the experiments, higher voltages are needed to shift the C-V curve to the right, while the corresponding electron discharging happens faster. To explain this phenomenon, we suggest that electron tunneling occur under positive programming

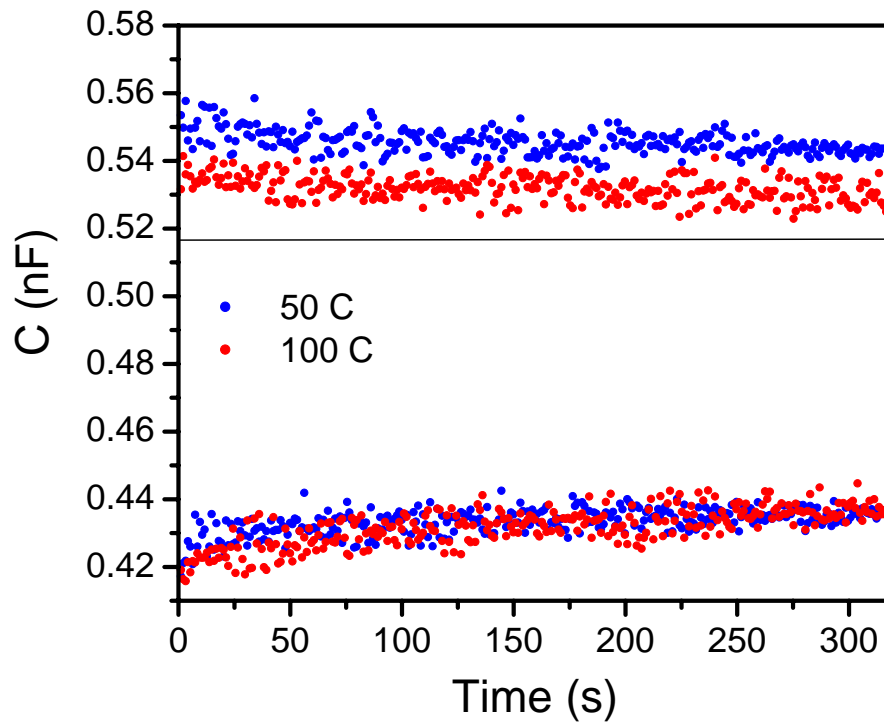


Figure 2.11. Capacitance decay measurements on a nanocrystal floating gate MOS capacitor ($V_G=0$ after charge injection at ± 5.5 V) at 50 °C (blue) and 100 °C (red), respectively. The line indicates the capacitance before charging.

voltage and hole tunneling occur under negative programming voltage. For Fowler-Nordheim tunneling, the energy barrier is about 4.7 eV for holes and about 3.1 eV for electrons between Si and SiO₂. In conventional floating gate memory with the tunnel oxide thickness at least ~8 nm, the tunneling component due to holes is many orders of magnitude smaller than the electron tunneling component. Therefore, it is almost impossible to inject holes from the channel to the floating gate. However, this difference becomes smaller as the oxide thickness is scaled down into the direct tunneling region, which makes hole tunneling possible.⁸³ During programming, an n-type inversion layer has to be formed inside the channel before pronounced electron tunneling from the channel to nanocrystal floating gate becomes possible. This is not, however, necessary for hole tunneling, which makes hole charging easier than electron charging [see Fig. 2.12]. During discharging, the smaller loss rate for holes results from the higher tunneling barrier just mentioned [see Fig. 2.13], but short retention time for electrons still suggests a large number of leakage paths between nanocrystals and the channel, which needs to be addressed to achieve an optimal memory performance. This topic will be investigated in Chapter 3.

2.5 Optical measurement

As an additional way to characterize Si nanocrystals and their size distribution, photoluminescence (PL) spectra were collected under excitation from the $\lambda_{ex}=457.9$ nm line of an Ar⁺ laser with a power density P_{ex} of 10 mW/mm² using a liquid nitrogen cooled (-118 °C) CCD array and a grating spectrometer. Stray light was removed by optical filters. The spectra were integrated for 10 s.

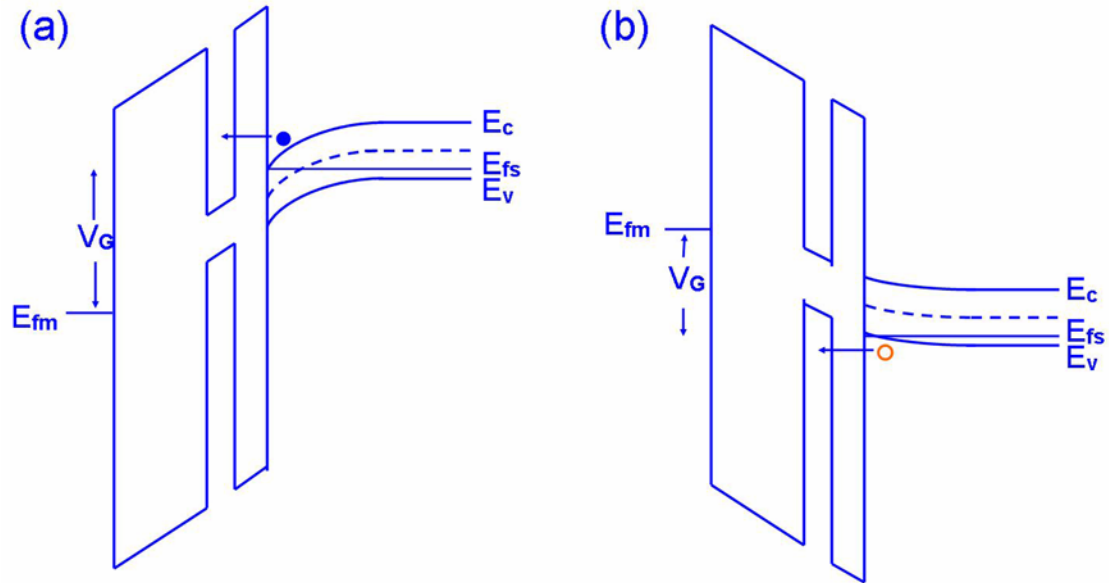


Figure 2.12. Energy band diagrams during programming with electrons (a) and holes (b). The substrate is *p*-type. The tunneling barrier height of electrons and hole are 3.1 eV and 4.7 eV, respectively.

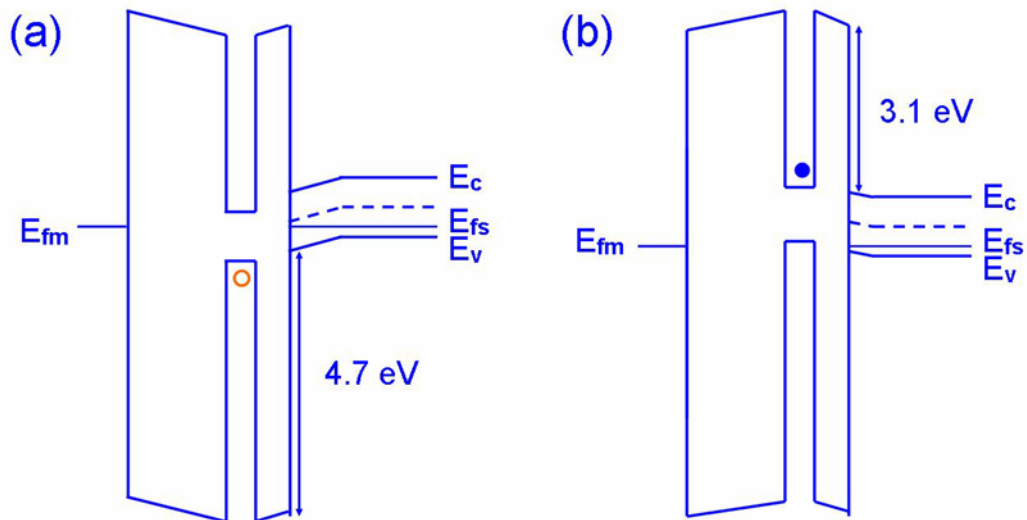


Figure 2.13. Energy band diagrams during retention for holes (a) and electrons (b). $V_G=0$. The substrate is *p*-type.

Figure 2.14 shows the room temperature PL spectrum of the nanocrystal sample. The peak of the spectra is about 750 nm and the FWHM is about 200 nm. The large spectrum width can be ascribed to the broad distribution of nanocrystal sizes. The peak of the

spectra corresponds to a nanocrystal diameter of 3.4 nm⁸⁴ when compared to calculations by Puzder et al.⁸⁵ It is well known that the band gap of Si nanocrystals widens due to quantum confinement, and surface passivation also plays an important role, especially at small sizes ($d < 3$ nm). A huge Stokes shift was observed for small nanocrystallites and an upper limit of the emission energy (2.1 eV, or 590 nm) was found and attributed to the charge trapping in Si=O bonds.²⁸ All these theoretical works help to clarify the controversy regarding PL mechanisms of nanostructured Si. However, a widely accepted theory which can be applied to obtain an accurate nanocrystal size distribution from an experimental PL spectrum is still lacked.

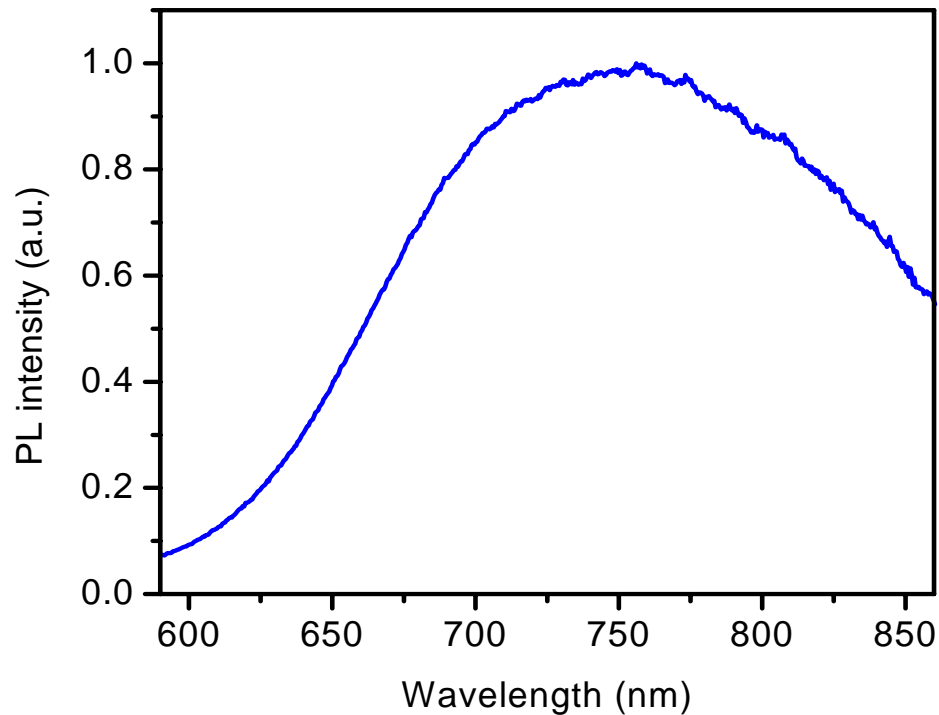


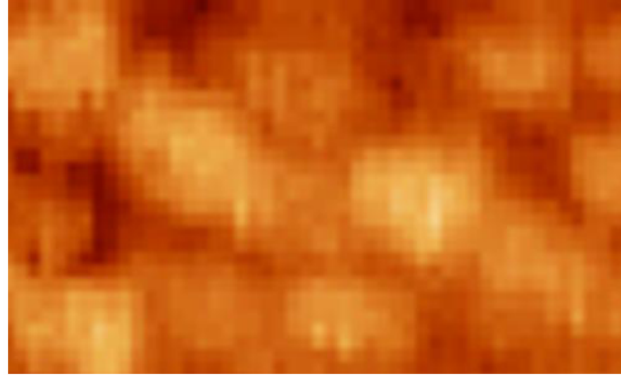
Figure 2.14. Normalized room temperature photoluminescence spectrum of nanocrystal sample [Fig. 2.2(a)]. $\lambda_{ex}=457.9$ nm, $P_{ex}=10$ mW/mm².

2.6 Comparison between Si nanocrystal density and charge density

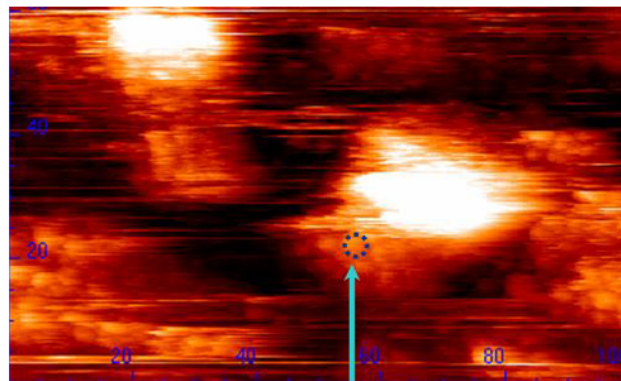
It is commonly believed that a very broad size distribution exists for Si nanocrystals fabricated through ion implantation. Regarding the sizes of Si nanocrystals in our nanocrystal memory devices, STM results set an upper bound of ~ 3 nm for lateral dimension and nc-AFM results give a distribution between 0.9 nm and 3.2 nm with an average value of 2.4 nm for vertical dimension. A spherical shape is assumed for Si nanocrystals, since the sizes are still much smaller than the oxide thickness (15 nm). With this assumption, the nanocrystal sizes can be described with the nc-AFM data. Large area contact mode AFM scans of a half-etched sample indicate a surface variation of about 3 nm [Fig. 2.4 (c)] and PL measurements give a average size of 3.4 nm. Both are roughly consistent with STM and nc-AFM results. It should be noted that even if the theoretical model for PL mechanism is accurate, the size obtained from PL data may be overestimated due to the energy transfer from small nanocrystals to large nanocrystals.⁸⁶

The areal density of nanocrystals on the fully etched sample is measured to be around $4 \times 10^{12} \text{ cm}^{-2}$, which is 25 times higher than the results from contact mode AFM. In fact, if we compare that with features in STM image [Fig. 2.15(b)], those “particles” in the contact mode AFM image [Fig. 2.15(a)] are likely clusters including dozens of nanocrystals. The comparison between contact mode AFM and STM clearly shows the ability of STM to resolve tiny individual nanocrystals, while using contact mode AFM alone may severely underestimate the nanocrystal density. However, considering the loss of nanocrystals during the etching process, $4 \times 10^{12} \text{ cm}^{-2}$ is still a lower bound. By applying the average nanocrystal size of 2.5 nm (r.m.c value), the calculation using the

(a)



(b)



Si nanocrystal

Figure 2.15. (a) Contact mode AFM image ($100 \times 60 \text{ nm}^2$) of half-etched SiO_2 film containing Si nanocrystals. [This is a close up of Fig. 2.4(b).] (b) UHV STM image ($100 \times 60 \text{ nm}^2$) of Si nanocrystals sitting on Si substrate. [zoom out of Fig. 2.6(b).]

total fluence of implanted Si^+ ions gives an area density of $3 \times 10^{13} \text{ cm}^{-2}$, which is an upper bound. This occurs because some Si^+ may be implanted into the Si substrate, and there is also Si loss by diffusion into the substrate during high temperature annealing. Even for Si atoms remaining in the SiO_2 , not all contribute to the formation of nanocrystals. Thus, the actual nanocrystal density should be between these two values.

In transistor-based floating gate memory, the stored charges in the floating gate screen the gate charge and effectively shift the threshold voltage of the device to more

positive (if charges are electrons) or more negative (if charges are holes) values. The magnitude ΔV_T is approximately given by⁴¹

$$\Delta V_T = \frac{q_0 n}{\epsilon_{ox}} \left(t_{ctrl} + \frac{1}{2} \frac{\epsilon_{ox}}{\epsilon_{Si}} t_{nc} \right), \quad (2.1)$$

where ΔV_T is the threshold voltage shift, t_{ctrl} is the thickness of the control oxide under the gate, t_{nc} is the linear dimension of the nanocrystals, ϵ 's are the permittivities, q_0 is the basic charge, and n is the density of charges stored in the nanocrystal floating gate. For nanocrystals that are 2.5 nm in dimension with a control oxide thickness of 8.75 nm, a threshold voltage shift of 1 V corresponds to a charge number density of 2.35×10^{12} cm⁻². For the C-V hysteresis curves shown in Figure 2.9, the largest voltage shift is less than 2 V, corresponding to a charge density of about 4×10^{12} cm⁻². Because the areal density of nanocrystals is between 4×10^{12} cm⁻² and 3×10^{13} cm⁻², the charge density is smaller than or at most equal to the areal density of nanocrystals in the floating gate, indicating at most one charge per nanocrystal on average. The conclusion is probably still true for even larger voltage shifts that we observed, such as 5 V in the ± 12 V scan, considering that the loss of nanocrystals in the etching process is nontrivial and the actual nanocrystal density is probably several times larger than the lower bound. Adding a second charge is unlikely to happen due to very small capacitance or large Coulomb charging energy of these tiny nanocrystals, which will be further analyzed in Chapter 6.

2.7 Summary

Ion implantation synthesis provides a simple and convenient way to fabricate Si nanocrystals that is compatible with current Si deposition techniques, but due to the

extremely small sizes and low Z contrast between Si and SiO₂ as well as the relatively broad spatial distribution in the SiO₂ matrix, TEM faces a huge challenge to correctly resolve Si nanocrystal sizes and areal density. We demonstrate that UHV STM/nc-AFM is an effective alternative to TEM for characterizing extremely small nanocrystals embedded in SiO₂. In electrical characterization, memory effects were evaluated primarily through C-V measurements. The retention characteristics were evaluated through capacitance decay measurements and show the application potential, especially with holes as stored charges. The asymmetric charging and discharging processes were explained by the differences between electron tunneling and hole tunneling. Comparison between flatband voltage shift and nanocrystal density indicates no more than a single charge per nanocrystal on average. Finally, more accurate nanocrystal density and size measurements made by UHV STM/nc-AFM enable the electrical measurements to be more clearly understood.

RHEED was chosen as an effective alternative to electron diffraction in TEM to verify the existence of nanocrystalline phase. Because of the small incident angle (a few degrees) and small penetration depth (a few nanometers) of the incident electron beam, RHEED is a highly sensitive tool to characterize nanocrystals on the surface of a single crystal substrate. The control samples in our experiments were obtained very conveniently. Since the initial dry oxide layers were grown on both sides of the wafers and Si⁺ ions were implanted only into the front side, the control samples (the back side) were automatically treated in the same way in all of the following processes.

Care was taken to keep samples clean in sample preparations. For example, the samples prepared for STM experiments were treated with UV-ozone followed by RCA

clean (immerse samples in a solution of 5:1:1 H₂O:H₂O₂:NH₄OH at 80 °C for 20 min followed by a rinse in DI water) prior to etching with buffered HF [7.2% HF (aq), 36% NH₄F (aq) v/v] for 40 seconds.⁸⁴ Care was taken to hold the samples horizontally during the etching process to keep the loss of nanocrystals to a minimum. The etching rate of such buffered HF to Si is extremely small, so the change of nanocrystal sizes due to etching itself is negligible. The oxidation in air is also negligible since the samples were loaded into UHV chamber within several minutes after etching, resulting in hydrogen terminated Si nanocrystals with sizes almost invariant.

Chapter 3

Electronic properties of tunnel oxide layer in silicon nanocrystal memory

3.1 Introduction

Among the different techniques used to synthesize Si nanocrystals, the ion implantation method is the simplest and most compatible with current silicon technology. In the previous chapter Si nanocrystal memory devices with nanocrystals fabricated through this method were characterized and analyzed, and the results showed that nanocrystals can be ideal charge storage nodes. However, a few problems were also noticed, such as high gate leakage and relatively short retention times for electrons. These problems revealed an important concern with the structures fabricated with this technique, which is the lack of good control over the nanocrystal depth distribution, and tunnel oxide thickness and properties in particular.

In other techniques such as CVD or SiO_x deposition, a high quality tunnel oxide layer is grown prior to the step of nanocrystal synthesis and plays a key role in the charge retention of the nonvolatile memory. The electrical properties of such an oxide layer can be tested with current-voltage (I-V) measurements on a metal-oxide-semiconductor (MOS) structure. But in the ion beam synthesis of nanocrystals, the tunnel oxide region cannot be identified until the formation of the nanocrystal floating gate in the SiO_2 matrix during annealing. Although I-V measurement on the MOS structure with nanocrystals

[such as that in Fig. 2.2(c)] can provide information on the overall gate leakage through both the thin tunnel oxide and the thicker control oxide [Fig. 2.8], it is even more important to study the electronic properties of the tunnel oxide alone. However, the fabrication of a MOS structure with control oxide removed first through chemical etching is not a good idea. Because of the existence of nanocrystals, a surface variation comparable to the tunnel oxide thickness [Fig. 2.4(b) and (c)] usually appears. In the I-V characterization of a MOS structure fabricated in this way, major current goes through some “dips” on the oxide surface with number of “dips” and local oxide thicknesses almost unknown. For this reason, it is hard to provide comprehensive and accurate information regarding the electronic properties of the tunnel oxide layer. Prior to this research study, there is no report focusing on direct electrical characterization of the tunnel oxide layer of nanocrystal floating gate memory fabricated through ion implantation.

3.2 Conductive atomic force microscopy

While conventional I-V measurements lack the ability to study the tunnel oxide layer in the nanocrystal memory fabricated by ion implantation, conductive atomic force microscopy (C-AFM) has proved to be a powerful tool in this area. In the literature, C-AFM has already been widely applied to measure nanometer-scale electrical characteristics in the study of thickness variation⁸⁷ and degradation issues^{88,89,90} of SiO₂ gate films. By using C-AFM on the half-etched nanocrystal sample with the control oxide removed, morphology, spatially resolved current images, and local I-V characteristics can

be obtained simultaneously, providing complete information for the analysis of electron tunneling through the tunnel oxide layer of the nanocrystal memory device.

Figure 3.1 shows the schematic of the C-AFM. The contact mode AFM cantilever was coated with PtIr₅ and used as the top electrode, and the metalized Si substrate was used as the bottom electrode. A DC voltage was applied to the cantilever and the current was measured. The measurements were carried out in an UHV chamber (2×10^{-9} Torr) to reduce the residual water layer on the surface. To prevent wear of the coating at the tip, the contact forces were maintained on the order of 1 nN. To study the electronic properties of the tunnel oxide layer, we used buffered hydrofluoric acid to etch a nanocrystal sample without gate structures to the depth of the peak of the Si implantation profile calculated by TRIM (approximately 10 nm). The average thickness of the remaining SiO₂ was measured by ellipsometry to be 5.1 nm. Since there is no well defined tunnel oxide region due to the relatively broad depth distribution of nanocrystals, we chose this depth considering that it corresponds to most charge storage locations in the device. Under different geometries (i.e., if the control oxide were removed), electron tunneling dominates under both positive and negative biases in the C-AFM experiments.

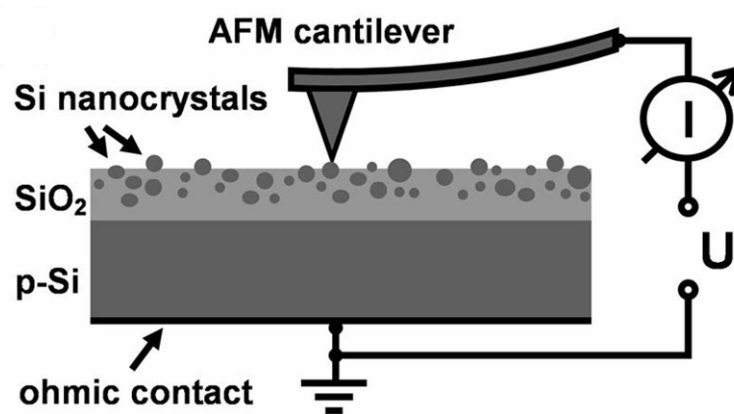


Figure 3.1. Experimental setup for conductive AFM (C-AFM).

3.3 Morphology and current images

In the C-AFM experiments, the scanned area is $300 \times 300 \text{ nm}^2$. Surface morphology (400×400 data points) and local I-V curves (100×100 data points) were measured simultaneously. After measurements, current images at different biases can also be displayed. Figure 3.2 shows the topography [Fig. 3.2(a)] and corresponding current images at +1.36 V [Fig. 3.2(b)] and +4.63 V [Fig. 3.2(c) and (d), with different scales], respectively. An overall correlation can be found between topography and current images, especially when comparing Figures 3.2(a) and 3.2(d). The correlation is obviously due to the dependence of electric current on SiO_2 thickness under a constant

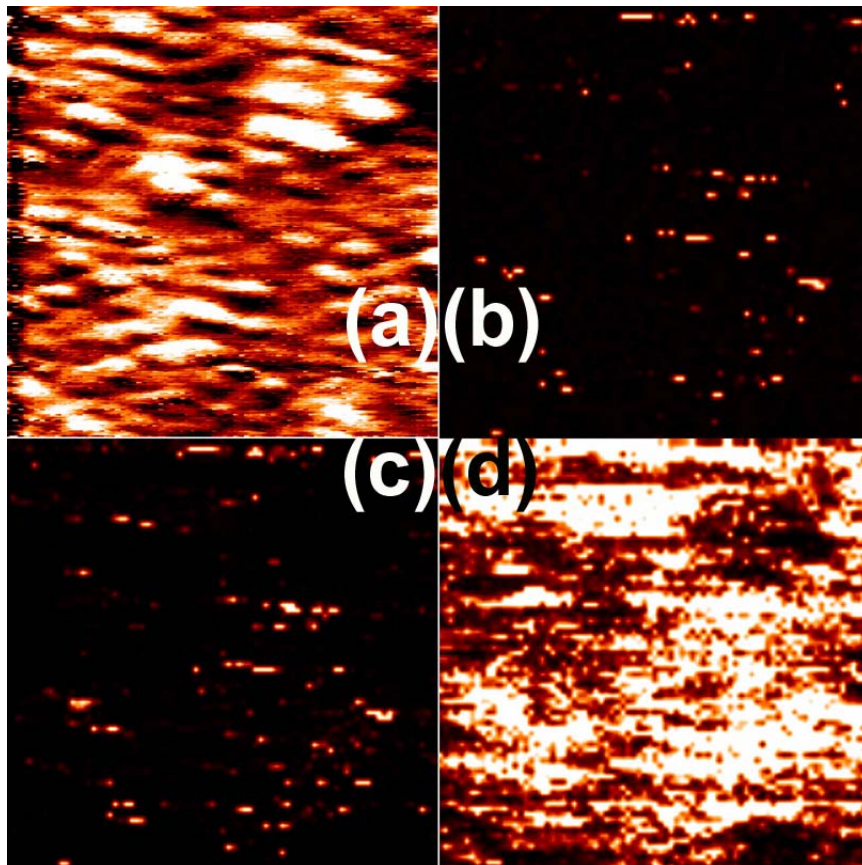


Figure 3.2. Surface morphology [(a), scale is 2.84 nm] and simultaneously acquired electric current images at the bias voltage of +1.36 V [(b), scale is 0.05 nA] and +4.63 V [(c), scale is 3.9 nA; (d), scale is 0.05 nA]. The scanned area is $300 \times 300 \text{ nm}^2$.

bias. In addition, we noticed some leaking spots where the electric current larger than the noise level (about 1 pA) was first detected [Fig. 3.2(b)]. At a larger bias [Fig. 3.2(c)], the currents through these spots are still much larger than that through surrounding areas, even if the surrounding areas have a similar nominal oxide thickness. Figure 3.3 shows the topography [Fig. 3.3(a)] and corresponding current images at -2.13 V [Fig. 3.3(b)], -3.74 V [Fig. 3.3(c)], and -5.76 V [Fig. 3.3(d)]. For comparison, the negative biases of Fig. 3.3(b) and Fig. 3.3(d) were chosen so that the magnitudes of the overall average currents are the same as that of Fig. 3.2(b) and Figs. 3.2(c),(d), which are 5 pA and 0.3 nA, respectively. The features of the images in Fig. 3.3 are very similar to that observed

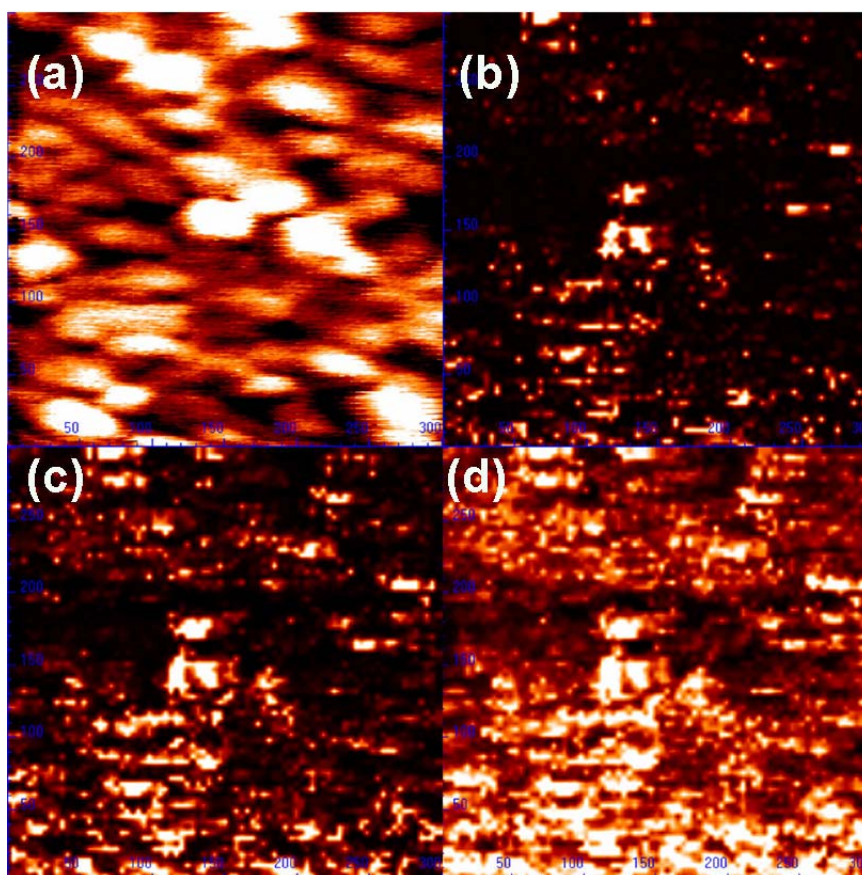


Figure 3.3. Surface morphology [(a), scale is 3.06 nm] and simultaneously acquired electric current images at a bias voltage of -2.13 V [(b), scale is 30 pA], -3.74 V [(c), scale is 0.15 nA], and -5.76 V [(d), scale is 0.6 nA]. The scanned area is 300×300 nm².

in Fig. 3.2, but with a much smaller contrast in the current images, especially under large biases.

The features in the topography and current images can be explained with the sample structure illustrated in Fig. 3.4. Because of the inhomogeneity originated from ion implantation and nanocrystal growth in silica matrix, the spatial distribution of Si nanocrystals is nonuniform [Fig. 3.4(a)]. Since the etching effect of buffered HF on Si is

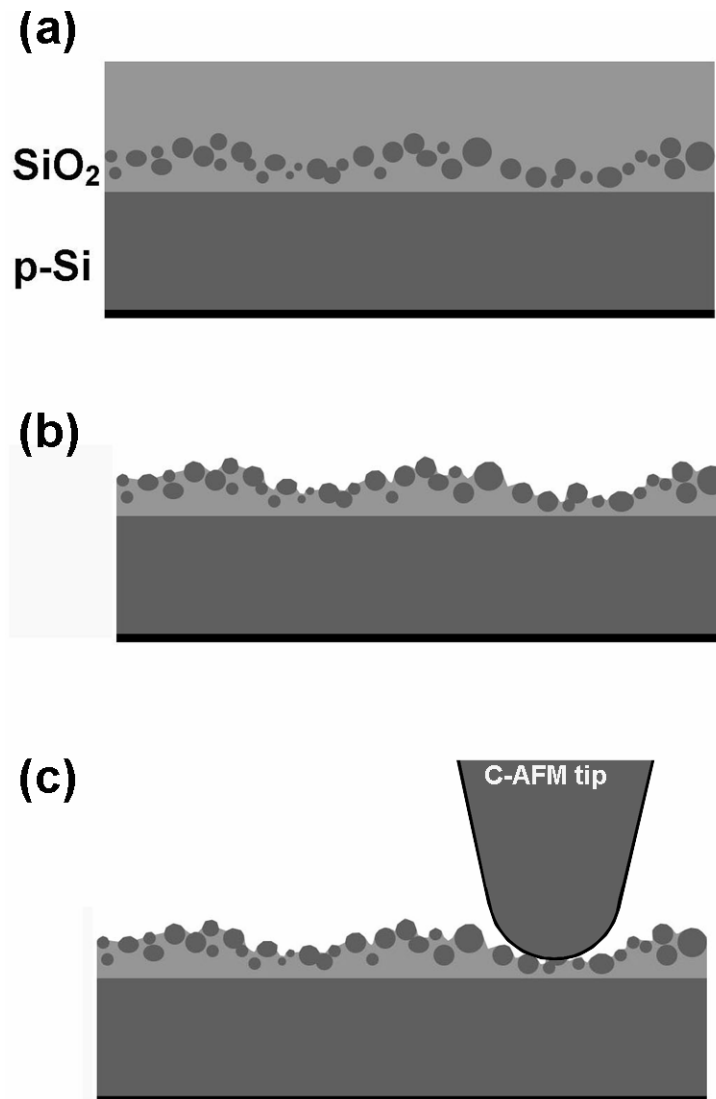


Figure 3.4. (a) The inhomogeneous distribution of Si nanocrystals in SiO₂ matrix. (b) The sample surface after 8 s etching with buffered HF. (c) In the C-AFM experiments, embedded nanocrystals largely increased the electric currents by decreasing the effective oxide thicknesses of the local oxide layer.

almost negligible compared with that on SiO₂, the etching process was severely hindered when reaching the Si-rich nanocrystal region at the end of the 8s etching period. The sample surface variation thus corresponds to the curved envelope surface of the Si-rich region [Fig. 3.4(b)], which includes Si nanocrystals and perhaps excess Si in SiO₂ and amorphous Si as well. In the C-AFM experiments, the electric currents depend primarily on the local thickness of the SiO₂ film, while nanocrystals also play an important role by decreasing the effective oxide thicknesses and greatly increasing the current magnitudes [Fig. 3.4(c)].

3.4 Quantitative analysis and discussion

Figure 3.5 shows maximum, minimum, and areal averages of all I-V curves collected, including both 0 to +6 V scan and 0 to -6 V scan. The currents under positive tip bias for those leaking spots observed in Fig. 3.2(b) and 3.2(c) sometimes exceed the limit set by the system and were recorded as 50 nA. Figure 3.6 shows histograms of current values at +3.52 V and -4.55 V, respectively. The data were collected within the same area and the voltages were chosen so that both have an average current of 0.1 nA.

The average oxide thickness is 5.1 nm, and the average tunneling current measured by C-AFM should be less than 1 pA⁸⁷ (or the sensitivity of our system) if the device grade oxide layer contains no excess Si. However, the currents through some leaking spots were observed to be even larger than the current level through a 1.1 nm film under similar conditions.⁹¹ Indeed, a detailed analysis on the current values shows a high level

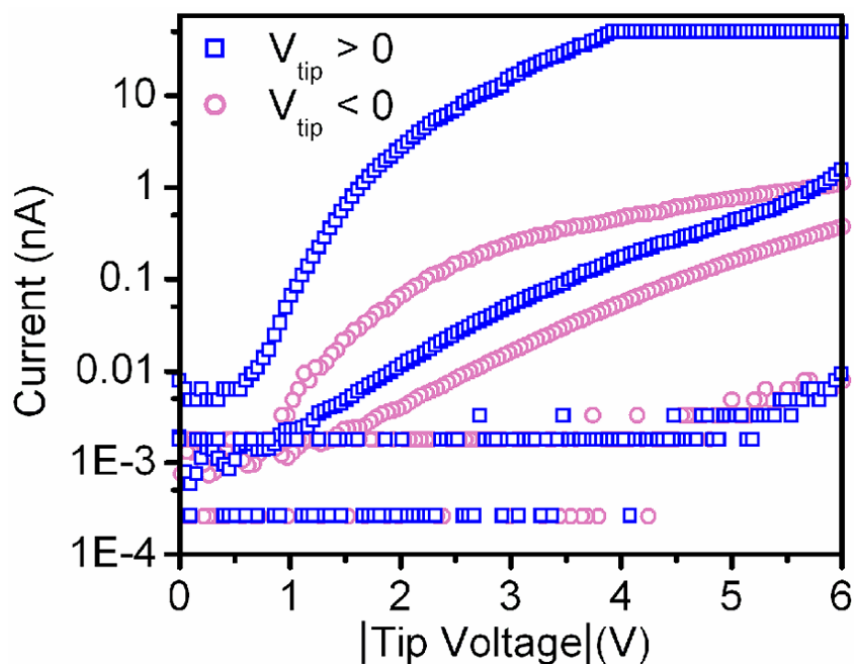


Figure. 3.5. I-V characteristics (squares: from 0 to +6 V; circles: from 0 to -6 V) corresponding to the spot with highest conductance, the spot with lowest conductance, and the average over all spots in the scanned area.

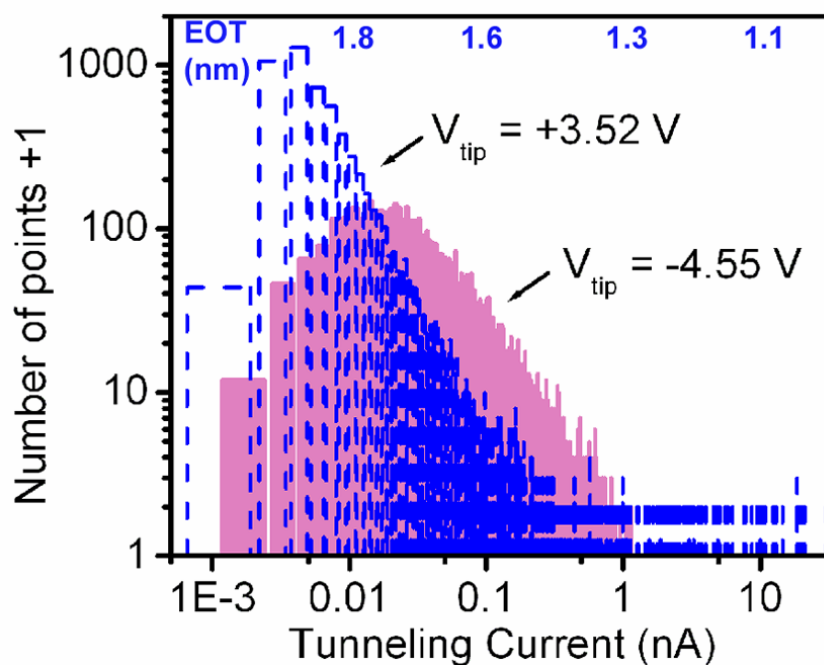


Figure 3.6. Histogram of current values in the current images at +3.52 V and -4.55 V, respectively. The bias voltages were chosen so that the average current is 0.1 nA for both situations. The equivalent oxide thicknesses (EOTs) are given for current values under positive tip bias.

of conductance for the whole area. An estimation of equivalent oxide thicknesses was made by calculating tunneling current densities through the film and comparing that with the theoretical and experimental curves^{92,93,94} showing the oxide thickness dependence of electron tunneling currents, with the difference in work function taken into account. The contact area between the AFM tip and sample surface may vary during the scan. An estimated average of 100 nm^2 with a range between 30 nm^2 and 300 nm^2 was based on similar experiments on device grade SiO_2 with known thickness. This range is consistent with the resolution of the C-AFM topographic images. In addition, due to the extremely high sensitivity of currents to local variations of oxide thickness, i.e., one order of magnitude change in current density only corresponds to less than 0.3 nm change of local oxide thickness, the contact area need not be known precisely. Under positive tip bias, calculation reveals that the estimated equivalent oxide thicknesses corresponding to the largest, smallest, and average currents are $1 \pm 0.15 \text{ nm}$, $2.4 \pm 0.15 \text{ nm}$ and $1.7 \pm 0.15 \text{ nm}$, respectively.

These values are much smaller than the actual thicknesses of the SiO_2 layer, which is about $5.1 \pm 1.5 \text{ nm}$. Such a big difference suggests the Si nanocrystal doped SiO_2 layer has a largely increased conductivity. Most likely, the concentration of implanted silicon is close to or even above the percolation threshold, so the separations between nanocrystals are not well maintained, creating high conductance paths. Recalling the upper limit of nanocrystal density, which is $3 \times 10^{13} \text{ cm}^{-2}$, and assuming no implanted Si was lost into substrate during annealing and that half of the nanocrystals were kept in our sample, there should be 15 nanocrystals with sizes about 2.5 nm within the $10 \text{ nm} \times 10 \text{ nm} \times (\sim 5 \text{ nm})$ region of SiO_2 film underneath the C-AFM tip. Since a volume of $(2.5 \text{ nm})^3$ can barely

hold one nanocrystal, there are totally $4 \times 4 \times 2$ spaces to hold the 15 nanocrystals. Statistics show that it is certain that some nanocrystals will occupy the “upper-floor” spaces and some nanocrystals will occupy the “lower-floor” spaces, and nanocrystals contact each other to some extent, both laterally and vertically. This can create high-conductance path underneath the AFM tip at any time during scanning.

The depth profile of implanted Si with a peak value of 20% excess Si atoms is very similar to the situation of percolation threshold in the simulation work of Müller et al.⁹⁵ According to their research, for high concentrations Si separates by spinodal decomposition during annealing. The nanocrystals become larger and may even interconnect, and the interface minimization of nonspherical Si structures leads to a narrowing of the denuded zone, which, for optimal device architectures, should be free of nanocrystals with a thickness of a few nanometers above the Si/SiO₂ interface [Fig. 3.7(a)]. Moreover, because larger nanocrystals dissolve more slowly, annealing time may not be enough to completely dissolve nanocrystals in the denuded zone, which would cause the scenario mentioned above. The reduced and contaminated denuded zone and the interconnections between nanocrystals [Fig. 3.7(b)] increased the overall magnitude of tunneling currents through the tunnel oxide.

One major advantages of nanocrystal memory is its immunity to oxide defects. In general, several leaking paths won't affect the function of the memory device. However, the histogram of current values [Fig. 3.6] shows that the equivalent oxide thicknesses are between 1.5 nm and 2.0 nm for most spots, and are even close to 1 nm for some spots. The actual distances between the contacted nanocrystals and the channel should be even smaller than these values, considering the cross section of nanocrystals is much smaller

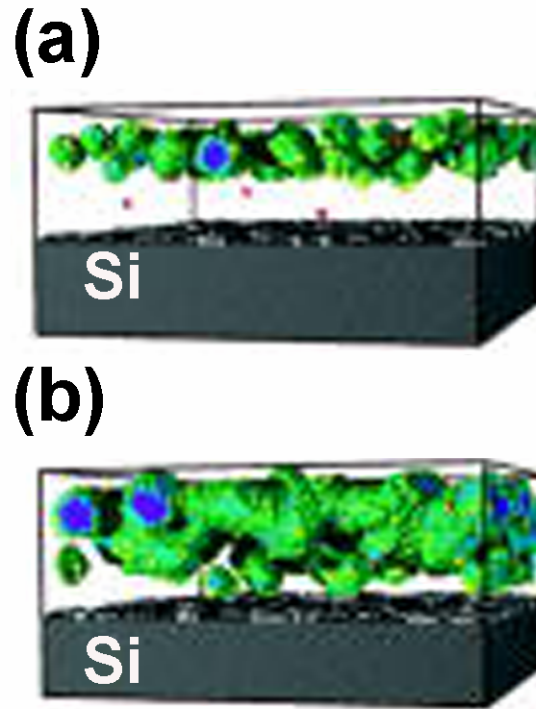


Figure 3.7. Cross section of nanocrystal distribution in the (a) “nucleation and growth” regime and (b) “spinodal decomposition” regime with limited annealing time.⁹⁵

than the contact area of the AFM tip. The high conductance observed at most spots in the scanned area is responsible for the relatively short retention time of the memory device, which is about 1 hour to lose the initial 30% of electrons in our capacitance decay measurements. The tunneling of holes cannot be tested in C-AFM because electrons are still the dominant carriers even under negative tip bias, which is different from the situation in device operation. As stated in the Chapter 2, the barrier height for holes is larger than that for electrons, and consequently a much longer retention time for holes was observed.

When studying the I-V curves in Figure 3.5, the max/min ratio under positive tip bias was found to be much larger than that under negative tip bias. The smaller dependence of current on surface morphology under negative tip bias was also noticed in the histograms

of current values [Fig. 3.6]. This difference can be due to the non-ohmic contact between the metallic AFM tip and the Si nanocrystal layer. In fact, this contact can be viewed as a Schottky barrier. It can be neglected in the C-AFM setup under positive tip bias [Fig. 3.8(a)] but has to be taken into consideration when the tunneling current through oxide under negative bias is comparable to the saturation current of the Schottky barrier [Fig. 3.8(b)], which makes it the limiting factor for increasing the tunneling current. However, because the oxide voltage under negative tip bias is bigger than that under positive tip bias with the same magnitude, the tunneling current of the former could exceed that of the latter when the tunneling current is far below the saturation current of the Schottky barrier, i.e. in the area where the oxide is relatively thick. In addition, hole tunneling also makes a contribution to the total current under negative tip bias. For simplicity, most of our analysis and discussion of electron tunneling is focused on the I-V characteristics obtained under positive tip bias.

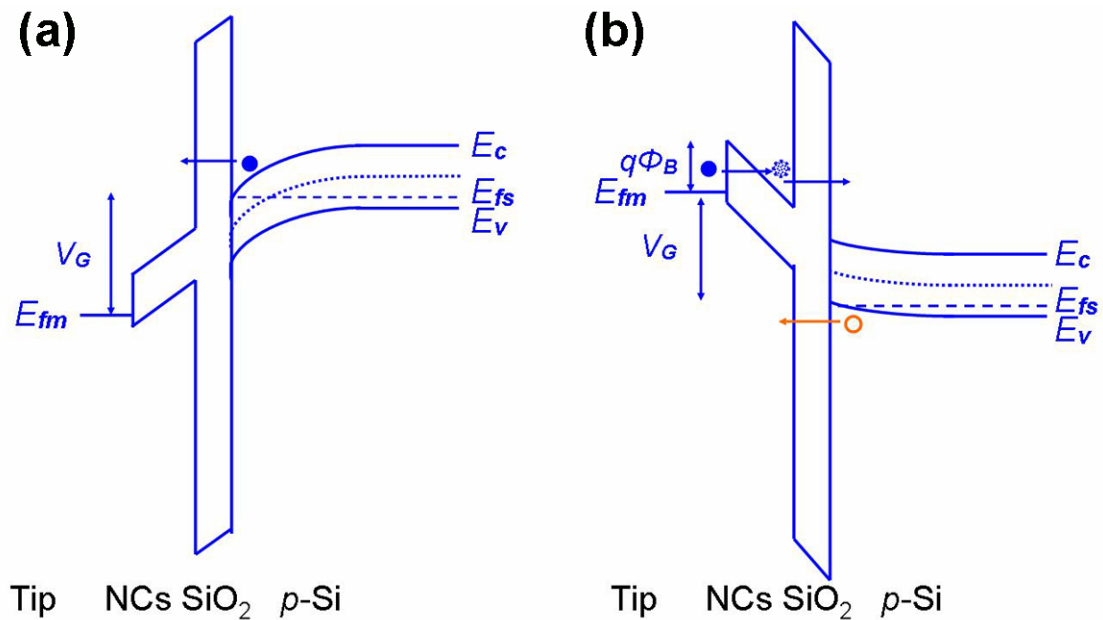


Figure 3.8. Energy band diagrams for positive tip bias (a) and negative tip bias (b) in the C-AFM. $\chi(\text{Si})=4.05$ V, $\Phi(\text{PtIr}_5)=5.3$ V, measured barrier height $\Phi_B=0.9$ V.

3.5 Switching events

Figure 3.9 shows switching events between a few I-V characteristics (a, b) and even fluctuations (c). This phenomenon agrees with the argument regarding the formation and distribution of nanocrystals. Under the AFM tip there are usually many nanocrystals, nanocrystal chains or nanocrystal clusters, which dramatically decrease the effective oxide thickness and increase the tunneling current. Among the many tunneling paths (Fig. 3.10), there are usually one or a few dominant paths where the corresponding effective oxide thickness is the smallest. In some cases, charges can be trapped in a nanocrystal of a dominant tunneling path and block that path, or can be removed from a nanocrystal and recover the path. Such on/off phenomenon leads to the switching of dominant tunneling path(s) or the switching events observed in I-V curves. For more complex situations, switching among many paths and even soft-breakdown behavior in the oxide can be

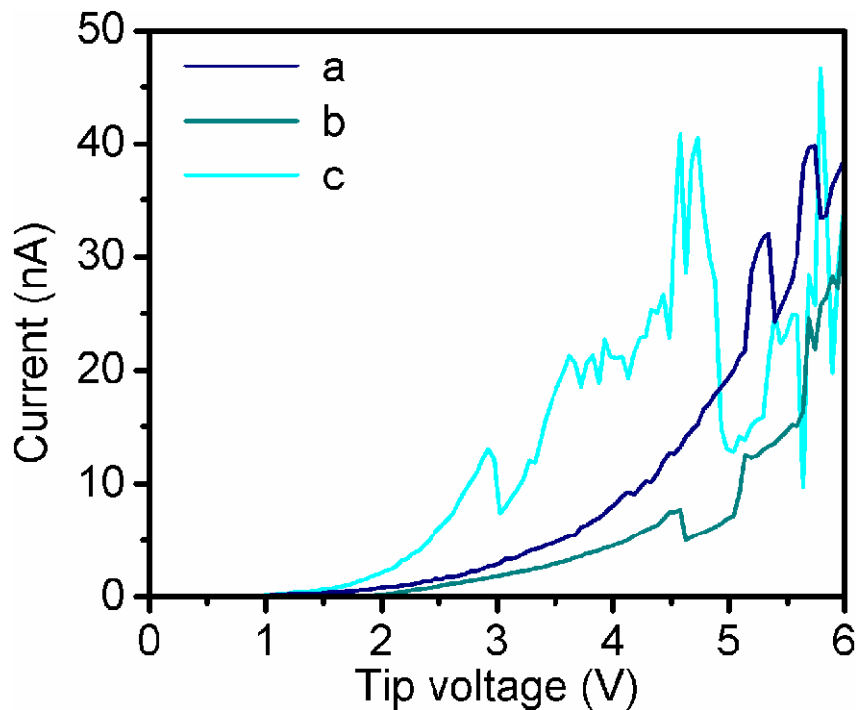


Figure 3.9. Typical I-V characteristics showing switching events between a few conductance states (a, b) and fluctuations (c).

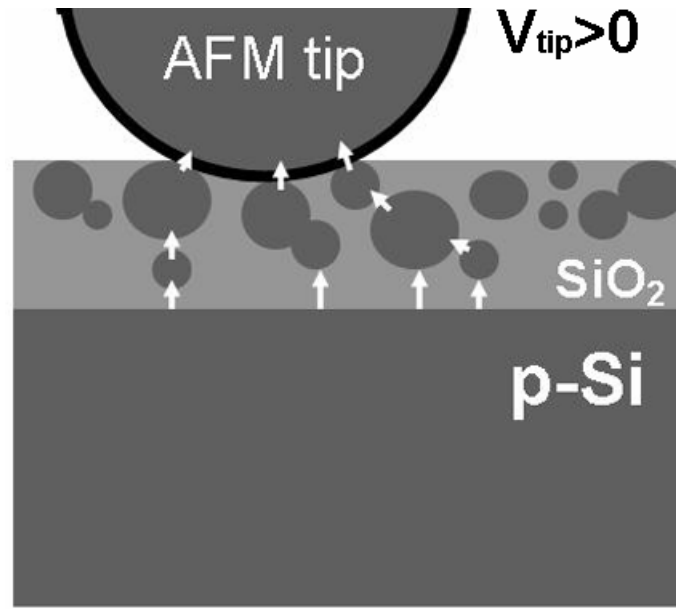


Figure 3.10. Schematic of current routes for electron tunneling through the SiO₂ film with Si nanocrystals.

observed. This is very similar to the behavior of stress-induced leakage current (SILC)^{89,96,97}. In SILC, it is the electrical stress that produces many oxide defects which increase leakage current through trap-assisted tunneling. In our study, fresh samples already have Si clusters, Si nanocrystals, and Si-related defects close to the substrate. They increase leakage current in a similar way.

3.6 Summary

In summary, C-AFM is shown to be an effective method for characterizing the electron tunneling between the nanocrystal floating gate and Si substrate. An overall high conductance was observed in the spatially resolved I-V characteristics and is responsible for the limited retention time for electrons. The interconnection between nanocrystals and the lack of a high quality denuded zone with enough thickness are suggested to be the

origin of the high conductance, which is further supported by switching events and fluctuations observed in some local I-V curves. The results clearly reveal the existing problem for the tunnel oxide layer and show the necessity of better control of Si nanocrystal distribution for true nonvolatile nanocrystal memory.

Chapter 4

Charge retention characteristics in Si nanocrystal doped

SiO₂ films

4.1 Introduction

In chapter 3, the electronic properties of the tunnel oxide layer were addressed by C-AFM. The lack of a denuded zone with high quality and enough thickness was suggested to be the origin of the overall high conductance of this layer, which largely increased the chances of charges tunneling back into the substrate. To improve charge retention, more efforts should be made to better control the Si nanocrystal distribution.

Indeed, Si nanocrystal memory fabricated through ion implantation has been criticized for its inferior charge retention characteristics in comparison to the 10 year requirement of electrically erasable programmable read only memory (EEPROM), which makes it limited to applications such as dynamic random access memory (DRAM) at its current stage. For longer charge storage, the nanocrystals must be better isolated. With the limitations of the current ion implantation technique, such as poor control over nanocrystal sizes and spatial distribution as well as defect amount, the simplest way out is by increasing the tunnel oxide thickness in the vertical direction and the spacing between nanocrystals in the lateral direction, which sacrifices the benefits from tunnel oxide scaling and large threshold voltage offset. Actually, the ion-implantation energy and dose are selected with consideration of all of these factors.

While C-AFM provides information regarding electron transport through the tunnel oxide layer, it is just an indirect approach for investigating charge retention characteristics. Transistor measurements and C-V measurements give information about device operation, but lack the ability to monitor a few localized charges for the study of charge dissipation dynamics and mechanisms, which are important in guiding device fabrication and bringing up innovation. Conductive-tip nc-AFM⁹⁸ [refs] and EFM^{99,100,101} are very sensitive to the electrostatic force produced by a small amount of charges down to a single electron,⁹⁸ which makes them good tools for microscopic charge analysis. In addition, the conductive AFM tip can be conveniently used to inject charges into the surface layer of a sample surface by applying an appropriate bias. For all these reasons, conductive-tip nc-AFM and EFM have been widely employed for injection and probing of localized charges in silicon nanocrystals.^{102,103,104,105,106} Ng et al.¹⁰⁷ investigated the influence of Si nanocrystal distribution on charge decay rate, and Krishnan et al.¹⁰⁸ observed the effect of oxidation on charge localization and transport in a Si nanocrystal layer, both using lift mode scanning with detection of frequency shift. The vertical and lateral charge dissipations studied by conductive-tip nc-AFM and EFM may help to determine whether Si nanocrystal memory can be a viable way for further device scaling into the few tens of nanometers regime.

In this chapter we show from charge injection and imaging experiments in a UHV chamber that holes have a much longer retention time than electrons in the Si nanocrystal floating gate fabricated through ion-implantation. Using an electrostatic model for nc-AFM operation, the charge retention characteristics are analyzed quantitatively and found to have an approximately logarithmic dependence on time. All results from microscopic

charge analysis are consistent with previous capacitance decay measurements. The small dissipation rate of holes in both lateral and vertical directions makes it an interesting choice as the working charge in Si nanocrystal memory. Based on this idea, we suggest *p*-channel Si nanocrystal memory as a possible candidate for further device scaling.

4.2 Charge injection and imaging by conductive-tip noncontact AFM

Charge injection and imaging experiments were performed with an UHV VT STM/AFM (Omicron Nanotechnology). Figure 4.1 shows the schematics of the experiments. An n^+ -doped silicon cantilever with a resonant frequency of 284192 Hz was used for charge injection and subsequent charge imaging. The pressure inside the UHV chamber is around 10^{-9} Torr, which not only excludes the influence of surface water and other contamination as charge storage media and dissipation pathways, but also dramatically increases the Q factor and detection sensitivity of the nc-AFM. The scanning height and oscillation amplitude were observed to be around 10 nm and 5 nm, respectively, confirming that the working range is indeed “noncontact mode” rather than “tapping mode”. After a topographic image was obtained successfully with $\Delta f = -20$ to -30 Hz [Fig. 4.1(b)], the AFM tip was brought to the center of the area and the feedback was disabled. Then the tip was moved manually toward the sample surface, with the oscillation monitored by an oscilloscope, until the oscillation was fully quenched to indicate complete contact between the Si tip and the sample surface. A bias of typically +10 V or -10 V was applied to the tip with respect to the grounded sample substrate for around 10 s to inject holes or electrons into the sample surface [Fig. 4.1(a)]. To restore

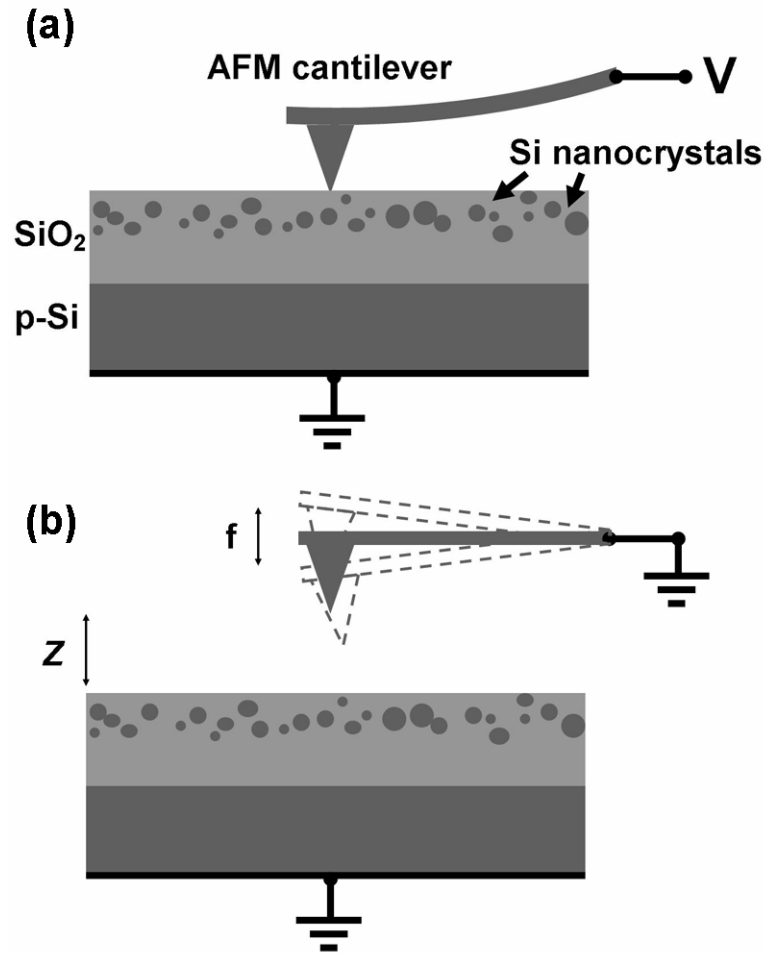


Figure 4.1. (a) Charge injection by lowering the AFM tip to touch the sample surface and applying a potential to the tip for a short period. (b) Noncontact mode imaging of surface morphology or surface morphology with injected charges.

scanning, the tip was retracted 50 nm from the sample surface, the tip bias was reset to zero, and the feedback was enabled again. A minor adjustment called “auto Δf ” was performed to adapt to the possible tip changes that happened in the contact period. After that, the tip can be auto-approached to the working distance of about 10 nm to begin continuous scans in non-contact mode and monitor the charge dissipation process in real time [Fig. 4.1(b)].

The charge injection and imaging experiments were first tried on the Si nanocrystal sample [Fig. 2.2(a)] which is most similar to the real device geometry, but no charging effect was observed. The 7-s-etched Si nanocrystal sample [Fig. 3.4(b)] was also tested and did not show the existence of local charges. We attribute the fail to a leaky SiO₂ layer which caused insufficient charging of Si nanocrystals. The majority of charges tunneled between the tip and the substrate rather than flowing into the nanocrystal layer during the charge injection, so the charged nanocrystals were limited to a very small area. Furthermore, the quantity of charges in the nanocrystal layer may be too little to be detected. In addition, because the nanocrystals are very close to the substrate, polarized charges at the interface further weakened the electric field produced by injected charges and made charge detection even harder.

It should be noted that we generally prefer intact Si nanocrystal samples rather than etched samples in the charging experiments. The latter contains mobile nanocrystals adhering to the surface which may touch each other and form fast charge dissipation paths. Even if the situation can be improved by additional oxidation¹⁰⁹ or by removal of the adhered nanocrystals using ultrasonic bath after etching, the charge dissipation dynamics still deviate from what would really happen in the original SiO₂ matrix.

In order to remove the influence of the leaky oxide on the charging and discharging processes, we chose to significantly increase the tunnel oxide thickness. The samples were fabricated by ion-implantation into 100 nm SiO₂ films followed by thermal annealing with similar conditions to that for device fabrication [Fig. 4.2]. The peak concentration of the implanted silicon is at a depth of about 10 nm, so the tunnel oxide

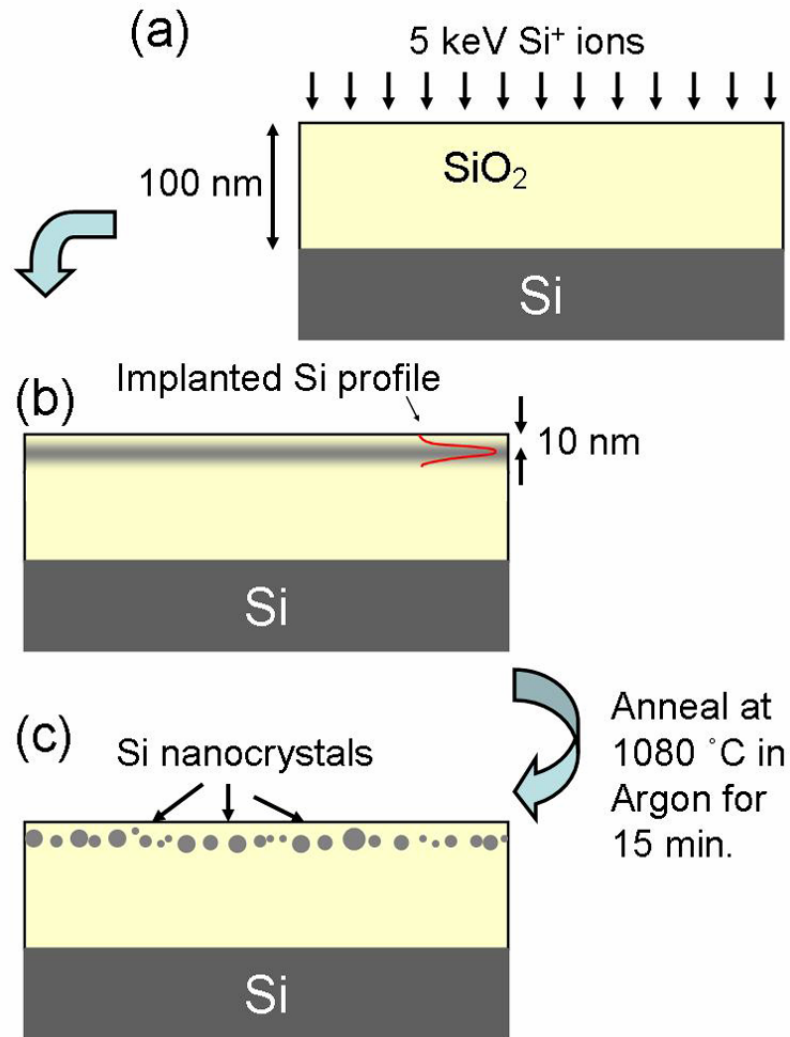


Figure 4.2. Synthesis of SiO₂ films (100 nm) containing Si nanocrystals which are distributed at a depth of around 10 nm. The Si⁺ ion implantation doses are $0.95 \times 10^{16} \text{ cm}^{-2}$ (low dose sample) and $1.27 \times 10^{16} \text{ cm}^{-2}$ (high dose sample), respectively.

thickness is around 90 nm, which almost completely forbids charge tunneling into the substrate during experiments. In addition to the same ion-implantation dose of $1.27 \times 10^{16} \text{ cm}^{-2}$ (“high dose”) that was used to fabricate the nanocrystal memory device in Chapter 2, a lower dose of $0.95 \times 10^{16} \text{ cm}^{-2}$ was also selected to evaluate the nanocrystal density dependence of the charge retention characteristics.

For these samples the anticipated mechanism of charge injection was described in Fig. 4.3. Since charge tunneling between the nanocrystal layer and the substrate can be neglected, the charge injection process is similar to the charging process of a parallel capacitor, in which the silicon substrate is the bottom plate and the nanocrystal layer is the top plate. In a classical parallel capacitor, charges flow into both conductive plates and distribute homogeneously until arriving at a stable state in which the electric field is limited to region between two plates. But in this case, such a state can not be reached since the charge diffusion was limited by the separation between nanocrystals. The field-enhanced charge diffusion stopped after a distance, resulting in a charged disk in the nanocrystal layer.

After the charge injection, the stored charges in Si nanocrystals may dissipate both laterally and vertically (Fig 4.4) through several possible mechanisms including direct tunneling, Fowler-Nordheim tunneling, thermionic emission, and hopping conduction. Charges on nanocrystals close to a sample surface may dissipate back onto the surface

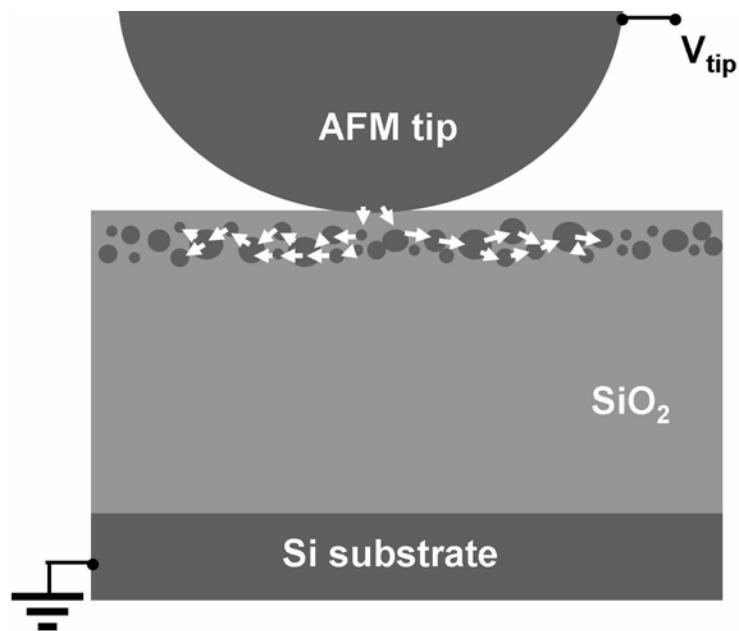


Figure 4.3. Schematic of the mechanism of charge injection with a biased AFM tip.

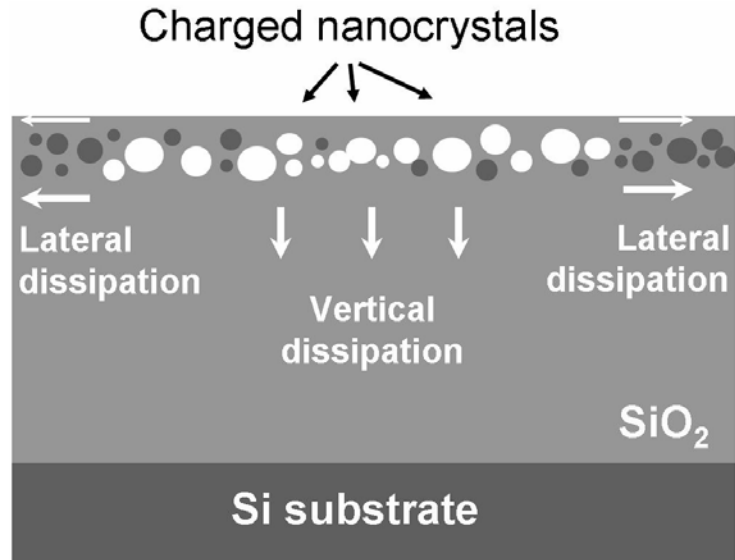


Figure 4.4. Schematic of the charge dissipation mechanisms.

driven by the electric field produced by other charges. Similarly, charges at the lower part of the nanocrystal layer may be trapped into nanocrystals and defects at larger depths, or even dissipate into the substrate through some high conductance paths. The lateral dissipation includes the dissipation on the sample surface (for surface charges) and the dissipation within the nanocrystal layer (for those charges still in nanocrystals). The latter is believed to have a strong dependence on the density of Si nanocrystals. During charge dissipation, both the loss of charges and the evolution of charge distribution change the electric field, which can be detected by the sensitive UHV nc-AFM. By analyzing time-dependent nc-AFM signals, abundant information regarding charge dissipation dynamics can be obtained.

4.3 Charging and discharging with electrons

A tip bias of -10 V for 10 s was applied to inject electrons into the SiO₂ film containing Si nanocrystals. The electron injection and imaging experiments were first tried on the “high dose” sample, but no electrons could be detected. However, when the experiments were repeated on the “low dose” sample, localized charging was clearly observed.

Figure 4.5 shows a series of nc-AFM images ($400 \times 400 \text{ nm}^2$) acquired after the charge injection. The frequency shift was set at -30 Hz. In the first image that was taken 10 minutes after the charge injection, there is a protrusion on the surface with a height of 5.5 nm. In the following scans the height of the protrusion decreased continuously. It was fairly clear that the protrusion was due to the electrostatic interaction between the doped silicon tip and injected electrons at the center of the scanned area. After around 1 hour,

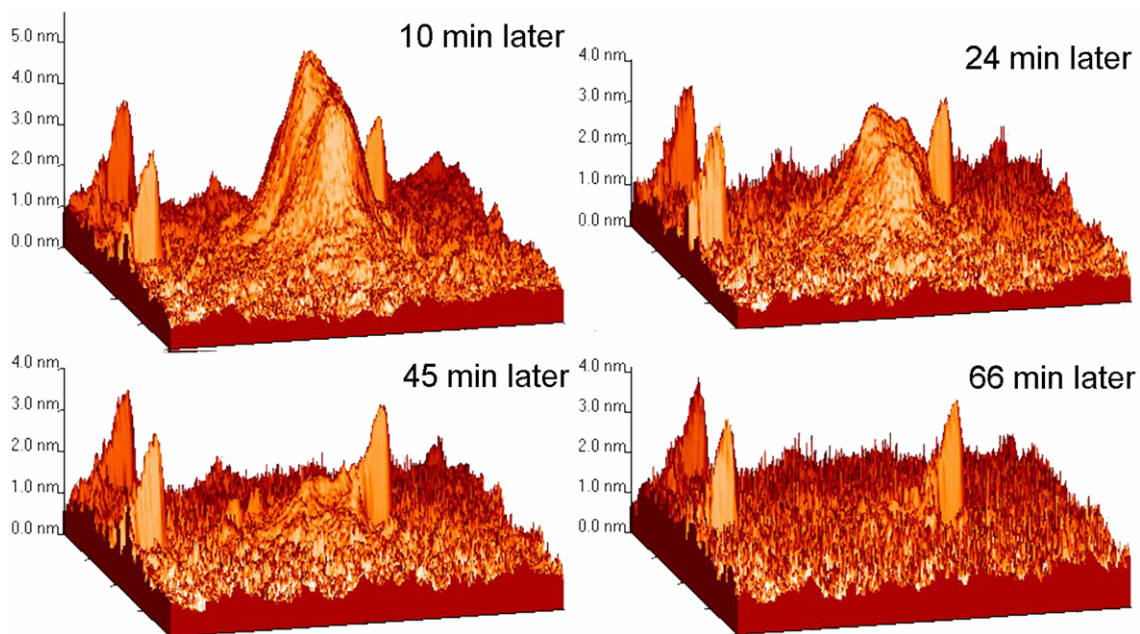


Figure 4.5. Noncontact AFM images acquired during the charge dissipation after charge injection into the low dose sample with a tip bias of -10 V for 10 s. The scanned area is $400 \text{ nm} \times 400 \text{ nm}$.

the protrusion was almost gone, indicating that the remaining charge amount was already below the detection limit of the system. In contrast, there were also three protrusions with no changes in shapes and peak heights. We believe these invariant protrusions were small debris dropped off from the silicon tip during the charging period. Because of the tip convolution effect, the tip shape rather than the shapes of the debris pieces were obtained (which is also called an “artifact” in AFM terminology). These debris pieces helped to provide references in the charging experiments.

Figure 4.6 shows the discharging series with the line profiles through the center of the protrusion. The inset shows time dependence of the peak heights. A fit with first order exponential decay function gives a time constant of 35 minutes, which is the time needed for the total charge to decay to 37% of the original amount.

There was a time gap of 6.5 minutes between charge injection and the first scan, and it took about 7 minutes to finish one frame, so it was estimated that the injected electrons had dissipated for 10 minutes before being detected. In more experiments for the “high dose” sample, the time gap was reduced to around 3 minutes and the scan time for each frame was reduced to 5 minutes, but there was still no charging phenomenon. The electrons must have dissipated away within 5.5 minutes, which is much shorter than the dissipation time of electrons in the “low dose” sample (~1 hour). The ion implantation dose of the “high dose” sample (1.27×10^{16}) is only 34% more than that of the “low dose” sample (0.95×10^{16}), which leads to fairly small differences in nanocrystal sizes and density between two samples. Assuming that the nanocrystal size distribution is the same, the average center-to-center spacing between nanocrystals in the ‘low dose’ sample

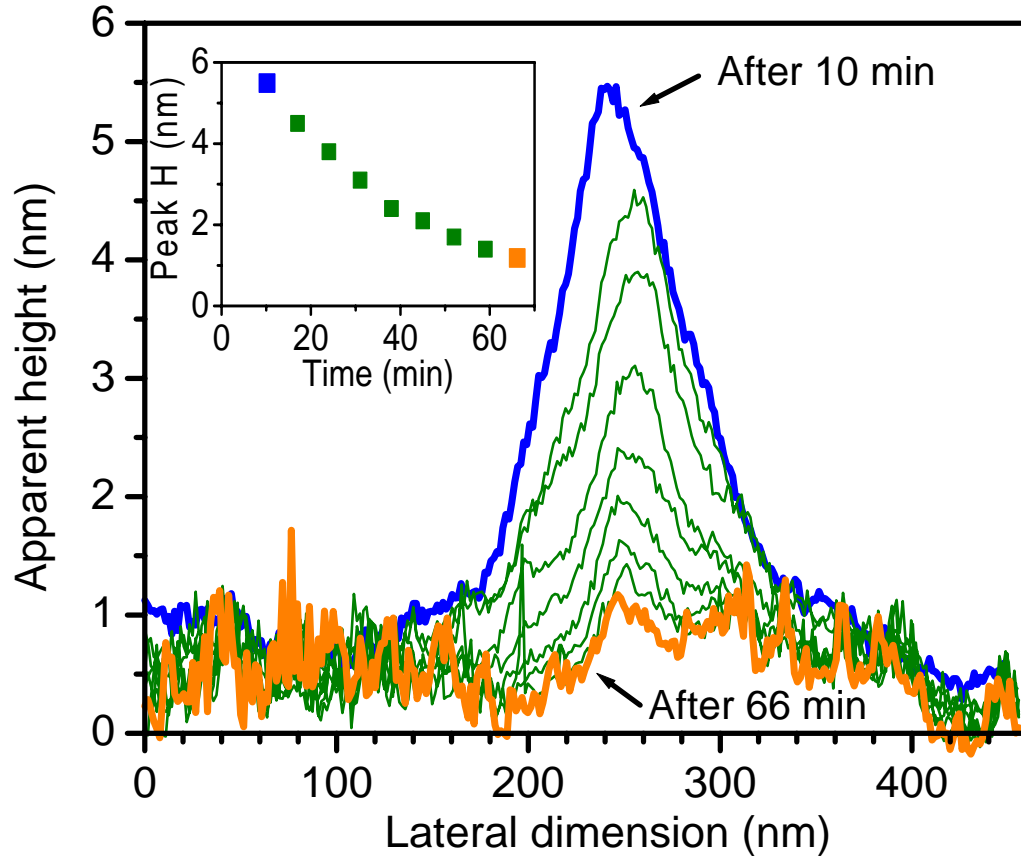


Figure 4.6. Series of line profiles showing the charge dissipation process after charge injection at -10 V. The first trace was taken approximately 10 min after the charge injection, and each subsequent trace at 7 min intervals. Inset shows the decrease of the peak height with time. A first order exponential decay fit gives $y = 0.064 + 7.243e^{-x/35.1}$.

is only about 10% more than that in the 'high dose' sample. The strong dependence of retention characteristics on ion implantation dose supports the analysis in chapter 3, which indicates that the concentration of excess Si in the SiO₂ matrix is close to the percolation threshold. In this situation, a small decrease in the ion implantation dose will largely reduce the chance to forming percolation paths, which improves charge retention.

4.4 Charging and discharging with holes

A tip bias of +10 V was applied for 10 s to inject holes into the SiO₂ film containing Si nanocrystals. In subsequent charge imaging, localized holes were detected in both the ‘high dose’ and the ‘low dose’ samples. As expected, the charge dissipation rate in the ‘low dose’ sample is smaller than that in the ‘high dose’ sample.

Figure 4.7 shows a series of noncontact AFM images ($400 \times 400 \text{ nm}^2$) obtained after injection of holes into the ‘high dose’ sample. The frequency shift was also set at -30 Hz. In the first image taken about 12 minutes after the injection of holes, a large protrusion with a peak height of more than 30 nm and a full-width half-maximum (FWHM) of around 150 nm was observed, indicating a much more total charge than that was recorded

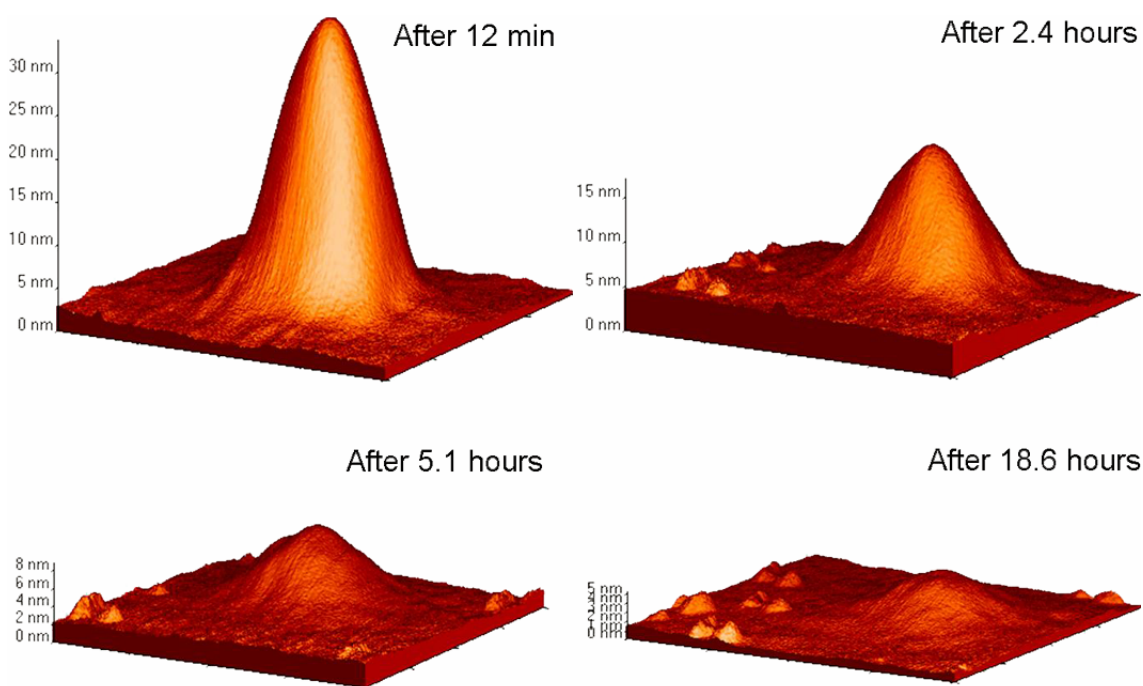


Figure 4.7. Noncontact AFM images acquired during the charge dissipation after charge injection the high dose sample with a tip bias of +10 V for 10 s. The scanned area is $400 \text{ nm} \times 400 \text{ nm}$.

in the electron charging experiments. Since then, it took 2.2 hours, 4.9 hours, and 18.4 hours for the peak height to drop to approximately 50%, 25%, and 12.5 % of 30 nm, respectively. Holes obviously show much better retention characteristics than electrons.

More detailed data can be found in Figure 4.8, which shows the discharging series of AFM line profiles through the center of the protrusion. A first order exponential decay fit to the curve of peak height versus time gives a time of 2.4 hours for the total charge to decay to 37% of the original amount. We attribute the much longer retention of holes to

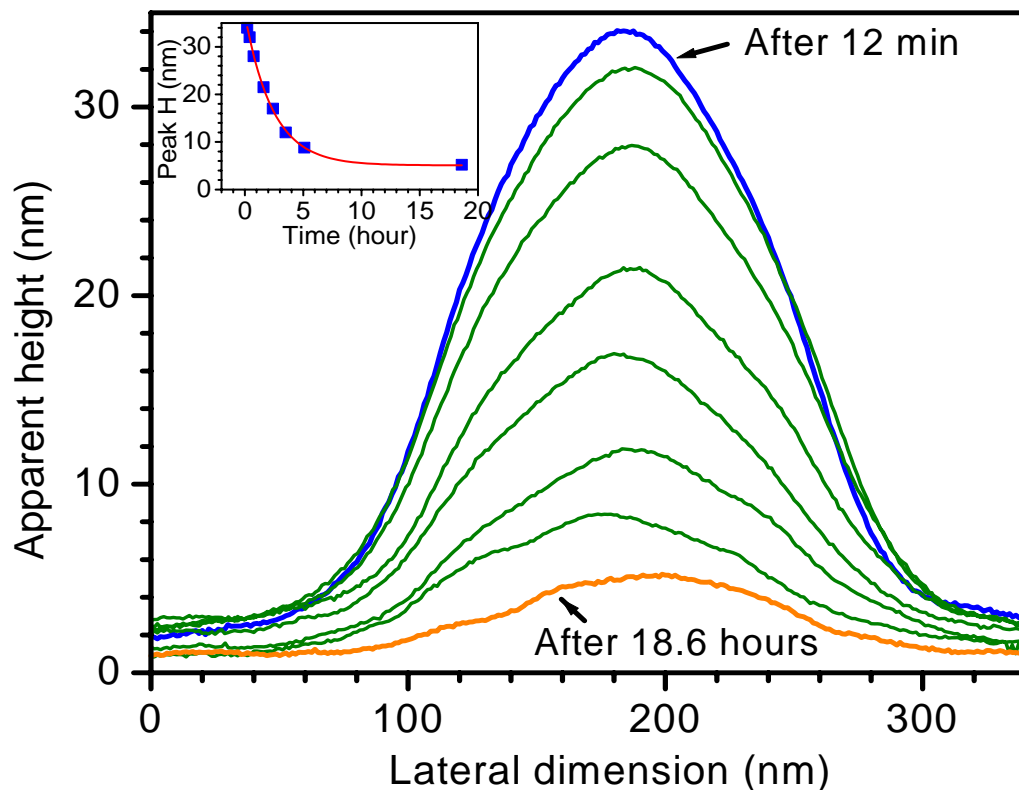


Figure 4.8. Series of line profiles showing the dissipation process after charge injection at +10 V. The first trace was taken approximately 12 min after the charge injection, and the last was taken after 18.6 hours. Inset shows the decrease of the peak height with time. A first order exponential decay fit gives $y = 5.08 + 31.6e^{-x/2.4}$.

the difference in the tunneling barrier heights: 4.7 eV and 3.1 eV for holes and electrons, respectively. These results are consistent with previous charge retention characteristics from electrical characterization of nanocrystal floating gate MOS capacitors in Chapter 2 and time resolved photoluminescence measurements by Walters et al.¹¹⁰

4.5 Control samples

Before further analysis of the experimental data, it is important to determine whether the detected charges were really stored in Si nanocrystals or just some other traps such as surface states and oxide defects. For this purpose, two types of control samples were investigated: one has 100 nm dry SiO₂ on Si without ion implantation and another has 100 nm SiO₂ on Si with the same ion implantation as the “high dose” sample but without high temperature annealing. Similar charge injection and imaging experiments were performed on the control samples. No injected electrons were observed for either sample. However, injected holes were observed in both samples.

Figure 4.9 shows the discharging series of holes in the control sample of SiO₂ without ion implantation. The peak height of the protrusion in the first image obtained 6 minutes after injection of holes is less than 10 nm. The time constant in the fit with first order exponential decay function is only 14 minutes. After 1.5 hours, most of the injected holes were gone. This result suggests that surface states of SiO₂ film did trap charges, but the trapped charges dissipated much faster than in the nanocrystal samples, which means the majority of the injected charges in the nanocrystal sample were not trapped at the sample surface.

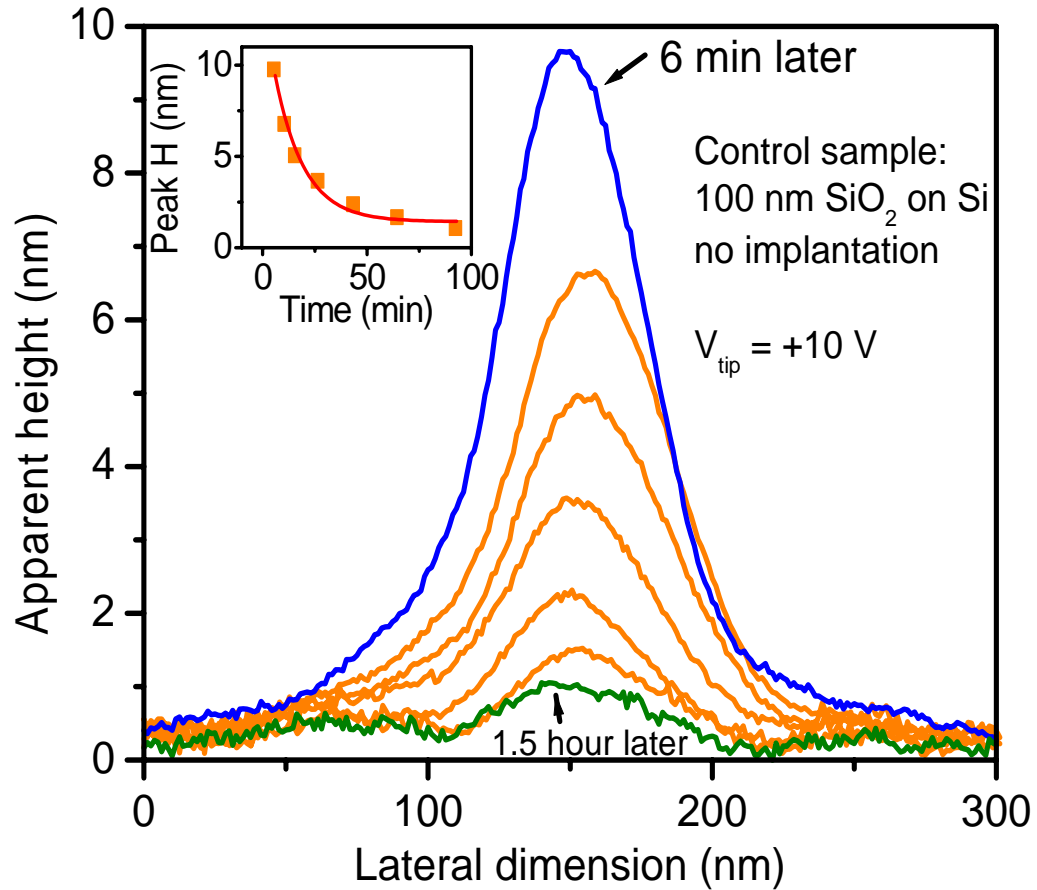


Figure 4.9. Series of line profiles showing the charge dissipation process after charge injection at +10 V into control SiO₂ sample without ion implantation. The first trace was taken approximately 6 min after the charge injection, and the last was taken after 1.5 hours. Inset shows the decrease of the peak height with time. A first order exponential decay fit gives $y = 1.42 + 12.3e^{-x/13.95}$.

Figure 4.10 shows the discharging series of holes in the control sample of Si⁺ implanted SiO₂ film without thermal annealing. The time constant in the fit with first order exponential decay function is 0.34 hour, and it took more than 4 hours to dissipate most injected holes. Compared with the SiO₂ control sample, more holes were detected and the dissipation was slower, revealing that a significant part of injected holes were not located at sample surface. However, the fact that the dissipation rate of holes in the ion

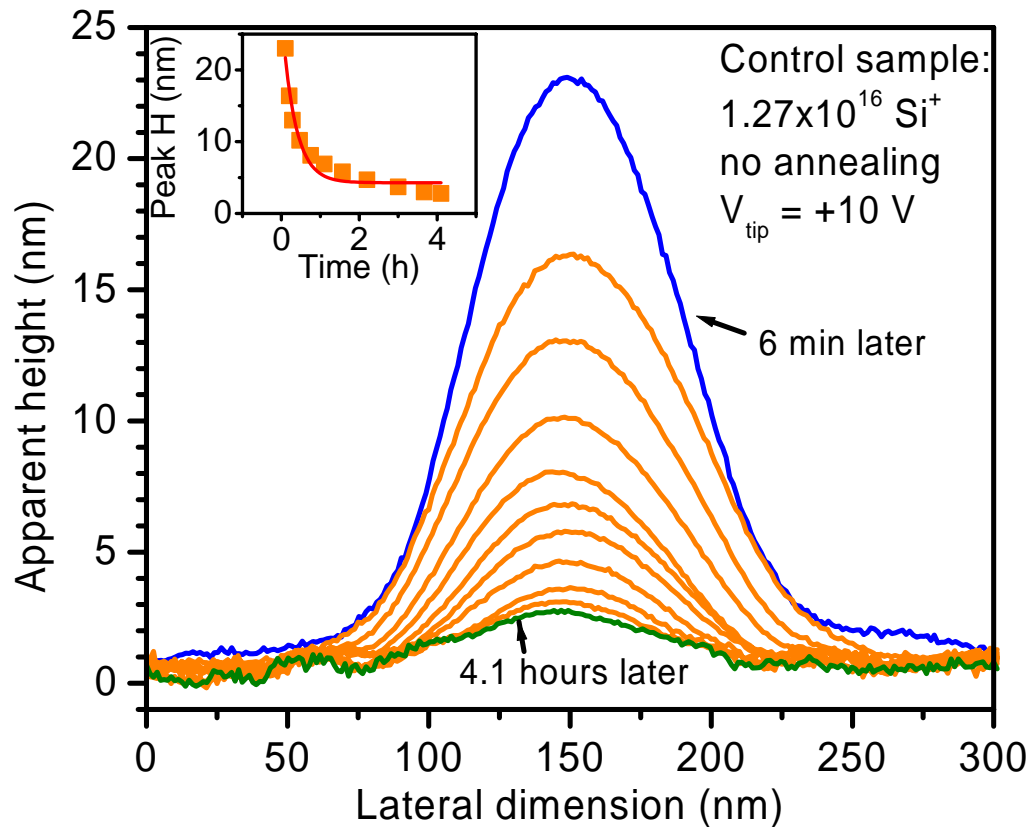


Figure 4.10. Series of line profiles showing the charge dissipation process after charge injection at +10 V into control sample with Si^+ ion implantation but without thermal annealing. The first trace was taken approximately 6 min after the charge injection, and the last was taken after 4.1 hours. Inset shows the decrease of the peak height with time. A first order exponential decay fit gives $y = 4.28 + 23.3e^{-x/0.34}$.

implantation control sample is still much larger than that in the nanocrystal sample indicates that oxide defects are unlikely the dominant charge traps in both situations. In fact, Boer et al. already demonstrated that charges can be trapped in or on Si nanocrystals or in surface states, but not in bulk oxide defects,¹⁰⁹ so the holes in the ion implantation control sample must be trapped in the Si-related defects,¹¹¹ amorphous Si clusters, or even very small Si nanocrystals that precipitated in ion implantation. The average size of these

nanostructures is smaller than the average size of nanocrystals formed in the high temperature annealing. According to the percolation theory, the average spacing between these nanostructures is also smaller than the average spacing between nanocrystals in the “high dose” sample, resulting in poorer retention characteristics for the ion implantation control sample.

Since surface states and Si-related nanostructures constitute faster charge dissipation paths with respect to those in the “high dose” nanocrystal sample, it is reasonable that no electron charging could be detected in both control samples. From the discussion, it can be concluded that during the charging of the nanocrystal samples most of the charges were trapped in the nanocrystals.

4.6 Discussion and qualitative analysis

Since the retention of holes was much longer than the retention of electrons, the analysis of discharging process was focused on holes. Figure 4.11 shows a 2D view of the nc-AFM images obtained after hole injection into the “high dose” nanocrystal sample. No obvious change can be noticed for the size of the “bright” area which corresponds to the protrusion in the 3D view. However, this phenomenon does not guarantee that holes dissipated only vertically. Electrostatic simulation indicated that areas of protrusion in the nc-AFM signal can remain almost unchanged even if the localized charges spread out laterally (see Chapter 5). In fact, indirect proof of the lateral charge diffusion can be noticed from the shape change of the bright spot. The spot is like an ellipse in the first image, which could be due to a small movement of the tip or asymmetric contact area

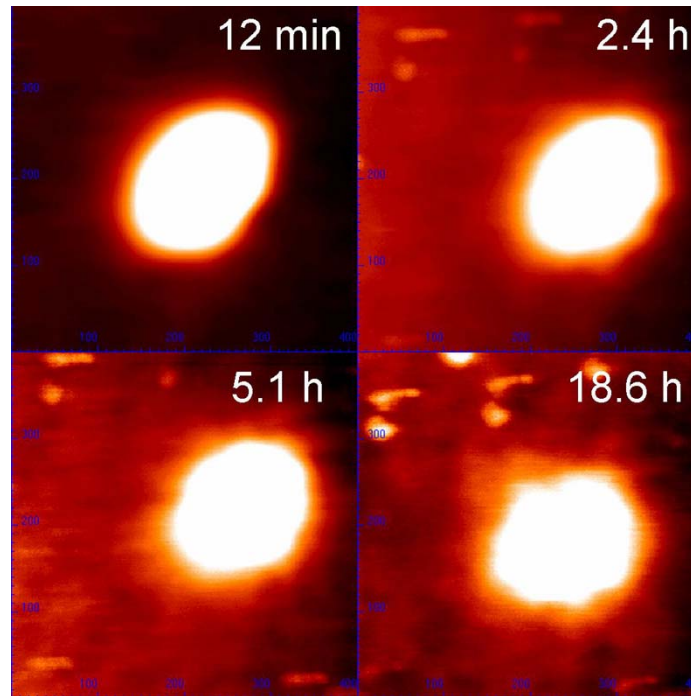


Figure 4.11. Noncontact AFM images acquired 12 min (scale is 16.5 nm), 2.4 hour (scale is 9 nm), 5.1 hour (scale is 4.6 nm), and 18.6 hour (scale is 2.86 nm) after charge injection into the high dose sample with a tip bias of +10 V for 10 s. The scanned area is 400 nm \times 400 nm.

during the charge injection. The difference between the long axis and short axis gradually decreased in the subsequent images until the spot become a circle in the last one.

Since the lateral charge diffusion happened very slowly, it is most likely not the reason responsible for the remarkable drop of the peak heights in nc-AFM line profiles. Instead, vertical dissipation into deeper charge traps or the substrate or back onto the surface followed by fast lateral dissipation through surface states could explain the nc-AFM results. Assuming the total charge is proportional to the peak height of nc-AFM signal, the charge loss rate can be directly obtained from the inset of Fig. 4.8. It should be noted that the fit to the exponential decay function provides only a guide for the eye and a rough trend of the charge dissipation. Because the constant term of 5.08 nm included in the obtained formula is obviously not the background apparent height without local

charges, the fit actually indicates that the exponential decay law cannot be used to describe the dissipation process. To make the issue more clear, the curves of peak heights of nc-AFM signal vs. time were plotted with different scales for holes in Fig. 4.12(c) and (d). With the logarithmic scale on the ‘peak’ axis (c), it can be noticed that the dissipation process is even slower than exponential decay, but the initial stage can be described with exponential decay very well. With the logarithmic scale on the ‘time’ axis (d), no good linear fit can be found, which is different from the discharging characteristics obtained from the capacitance decay measurements in Chapter 2. In comparison, Fig. 4.12(a) and (b) show similar plots for the electron discharging process, which indicate good linear fits

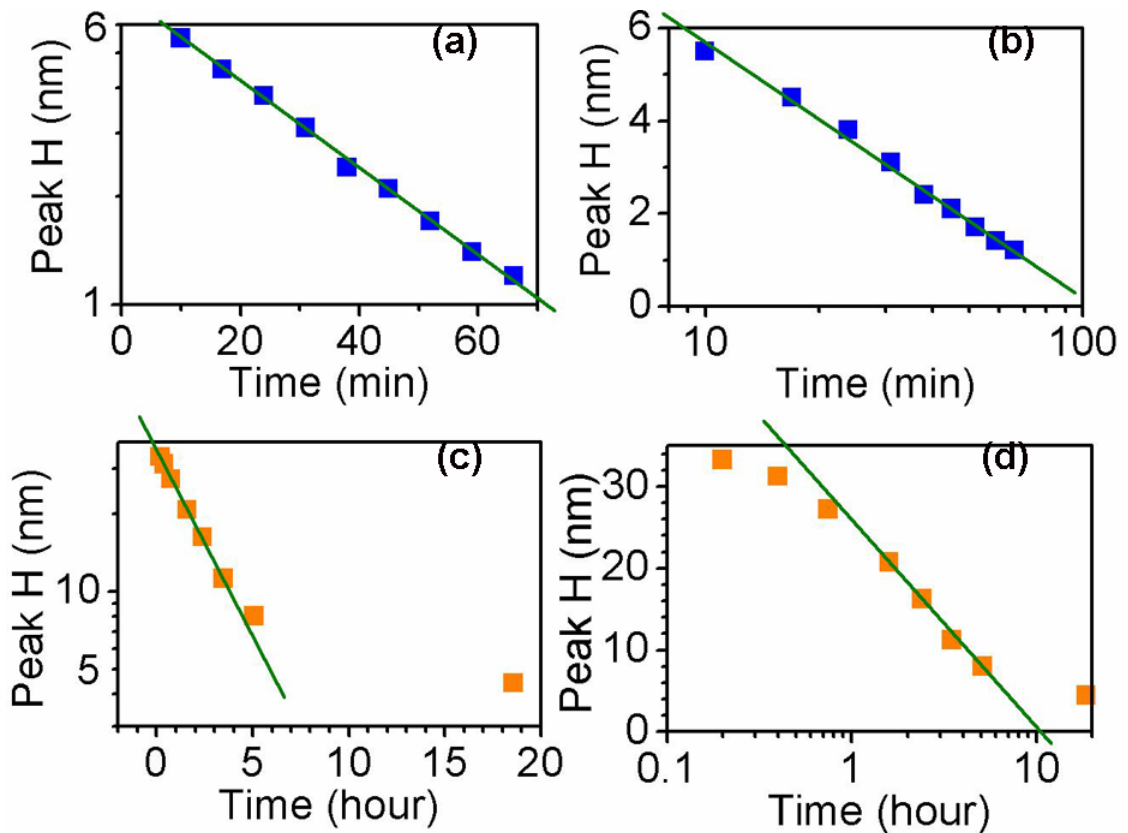


Figure 4.12. The time dependence of peak height in the charge imaging of localized electrons [(a), with log scale in “peak” axis; (b), with log scale in “time” axis] and holes [(c), with log scale in “peak” axis; (d), with log scale in “time” axis].

in both cases. We attribute this to the data points having been collected only within a limited period at the end of the discharging process.

The smaller charge dissipation rate than that in the exponential decay model can be understood in this way: If we assume the tunneling probability is a constant, the vertical tunneling current (i.e., loss rate of charges) upward or downward should be proportional to the total remaining charge, meaning that the relative loss rate of charges is always a constant which will result in exponential decay. However, the loss of charges will reduce the tunneling probability due to the decrease of the self-produced electric field [Fig. 4.13(a)], leading to even slower charge dissipation.

A similar energy band diagram can be drawn for the lateral charge dissipation [Fig. 4.13(b)]. The electric field or band bending is determined by the specific charge distribution. The lateral component of the electrical field produced by the 2D charge distribution is generally small, which results in a small tunneling probability between

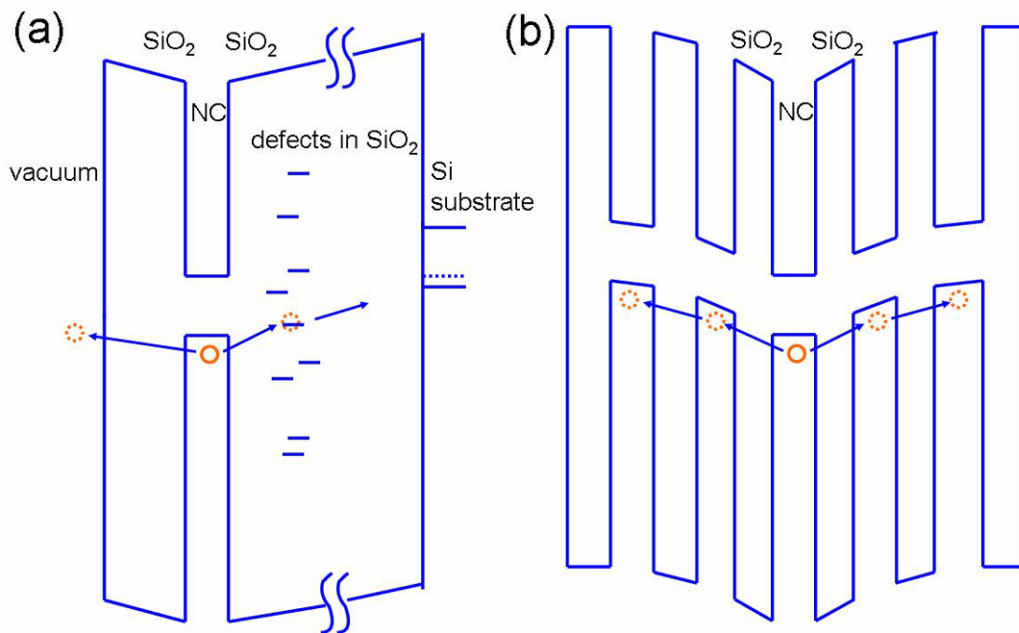


Figure 4.13. The Energy band diagrams showing field-enhanced diffusion of holes both in the vertical direction (a) and lateral direction (b).

nanocrystals. Hence it took a long time (18.4 hours) for the charged area to change shape from an ellipse to a circle by charge diffusion. However, the energy band diagram may also represent the charging process in which the large tip bias provided a stronger electrical field in both vertical and lateral directions. The charges tunneled from the Si tip to the nanocrystals underneath the tip, and tunneled further into surrounding nanocrystals to a distance where the electrical field is small enough. With the electric field due to the biased tip, the tunneling probability must be significantly increased since it took only several seconds to charge an area with a diameter of a few hundred nanometers.

4.7 Quantitative charge analysis through electrostatic simulation

UHV nc-AFM guarantees high detection sensitivity and stability in charge imaging experiments due to a lack of air damping, so a 3D electrostatic model can be developed to provide quantitative information regarding the distribution and evolution of the localized charges. The details of the model can be found in chapter 5. Simply speaking, nc-AFM scanning was simulated to obtain a curved surface with a specified force gradient. The forces include the van der Waals interaction and the electrostatic interaction between the Si tip and the sample. The highly doped Si tip was simulated with a conductive sphere, and the electrostatic force was calculated by summing up all the forces between the injected local charges and their image charges in the tip, with the polarized charges at dielectric interfaces taken into account. The van der Waals force was calculated using the Lennard-Jones pair potential by assuming a spherical shape for the tip and a flat plane for the sample.

In the simulation the initial tip height was set at 1 μm at one corner of the scan area, usually far away from local charges. Then a calculation was repeated to find the height corresponding to the preset force gradient. After the height was obtained, the value was then used as the initial value to find the height for a neighboring spot. Such operations were continued in an order such that the tip scans back and forth on a sample surface. Since the change of the force field from one spot to a neighboring spot is generally small, this method guarantees stability in the calculation.

In the nc-AFM, an attractive probe-sample interaction with $\partial F/\partial z > 0$ (the amplitude decreases with z , but the sign is negative) will effectively soften the cantilever, while a repulsive interaction with $\partial F/\partial z < 0$ will make it effectively stiffer. The change of apparent spring constant will modify the cantilever's resonant frequency to

$$\omega_0' = \omega_0 \sqrt{1 - \frac{1}{k} \frac{\partial F}{\partial z}}. \quad (4.1)$$

The original resonant frequency ($\omega_0/2\pi$) of the cantilever is 284192 Hz, and the force constant (k) is 42 N/m. The frequency shift in the experiment is -30 Hz, or the modified resonant frequency ($\omega_0'/2\pi$) is 284162 Hz. So the force gradient ($\partial F/\partial z$) is 0.008867 N/m.

Another preset parameter is the tip radius. Due to the damage incurred during the charge injection period, the tip was usually blunted,¹⁰⁹ which leads to poorer lateral resolution. However, a blunted tip can make better contact with the sample surface and make the charging process more efficient. The effective tip radius was determined in the simulation by finding the value that makes the van der Waals force gradient to be 0.008867 N/m at the 10 nm scanning height, which is 80 nm.

To extract information regarding the charge distribution from nc-AFM signals, an iterative method was used: in each round, a 3D charge distribution was assumed and the

corresponding nc-AFM signal was calculated and compared with the experimental signal, followed by a revision of the charge distribution based on the comparison. Such steps were repeated until a satisfactory match was achieved.

Figure 4.14 shows the experimental discharge time series after background correction and corresponding fits to these data. Except for the first one, all curves were fitted by assuming a 2D Gaussian distribution in the Si nanocrystal layer. It should be noted that

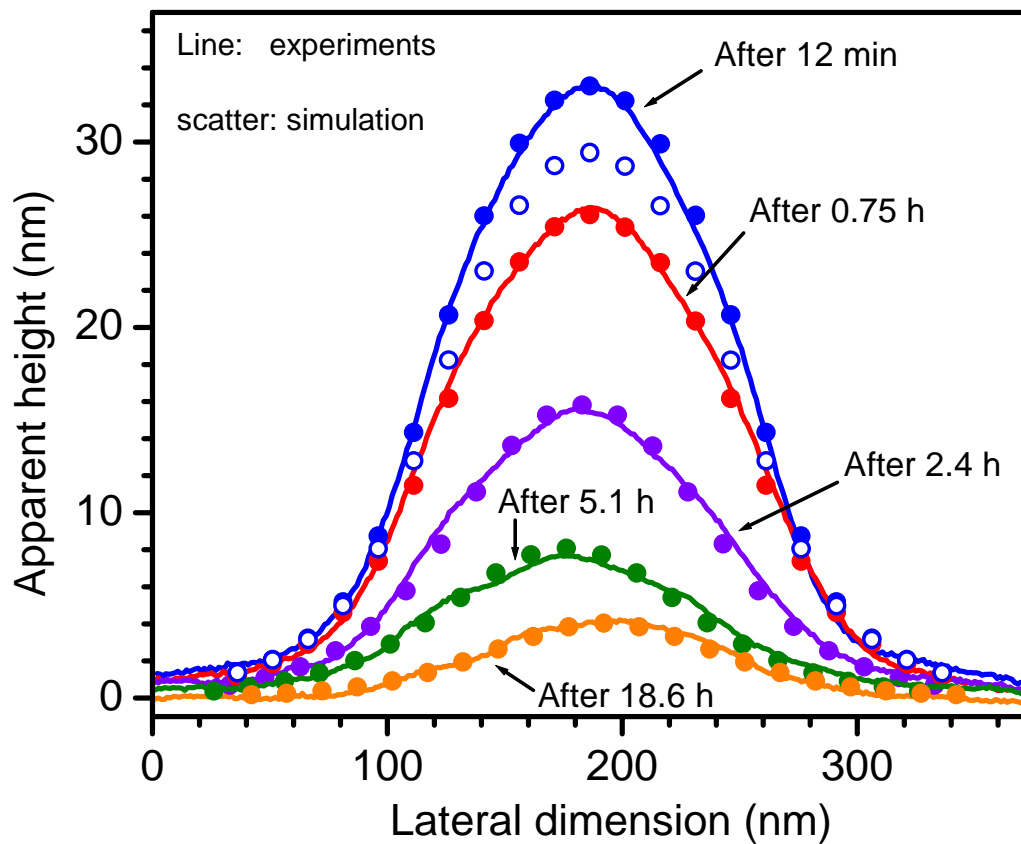


Figure 4.14. Experimental discharge time series (curves) and corresponding fits (filled circles) to the data. The fit to the nc-AFM line profile after 12 min assumes a 2D complementary error function distribution of holes in the nanocrystal layer and a 2D Gaussian charge distribution on the sample surface. The hollow circles show the simulated nc-AFM line profile without the surface charges. All fits to the subsequent curves were based on a 2D Gaussian charge distribution in the nanocrystal layer.

there may exist more than one solution of charge distribution to a given nc-AFM image, so some knowledge about the charge distribution is important for making a good “guess” and getting the correct solution. In this case, the charge dissipation process was found to be similar to the classical diffusion problem with a fixed amount of diffusion element, which follows a Gaussian distribution. Although the total charge decreased continuously due to vertical charge dissipation, it was assumed that the charges that remain in the nanocrystal layer followed 2D Gaussian distribution at anytime.

However, this assumption met serious problems when it was used to fit the first curve. It can be noticed that the peak in the first curve is narrower than the peak of the second curve. In another words, compared with the second curve, the first curve has a higher peak but has similar heights at the base of the peak. This phenomenon was only observed between the first and the second curve. In fact, a similar situation was also noticed in the ion implantation control sample (Fig. 4.10). When a 2D Gaussian distribution was applied to fit the first curve, the total charge was calculated to be only about 90% of the total charge corresponding to the second curve, which is obviously wrong. More efforts were made by including surface charges which could account for a narrower peak. However, doing so only helped to explain part of the peak increase but did not fundamentally change the phenomenon mentioned above, and the calculated total charge was still smaller than that for the second curve.

Recalling that the lateral charge dissipation is a slow process, the charge distribution probably did not change much between charge injection and the first scan. Since the charging process is similar to the classical diffusion problem with a source, which follows the complementary error function distribution, we applied a 2D complementary

error function distribution to holes in the nanocrystal layer and a 2D Gaussian distribution to holes on the sample surface, and the obtained results matched the charge dissipation trend very well.

Figure 4.15 shows the cross-sections of the 2D complementary error function distribution and the 2D Gaussian distributions that fit the experimental nc-AFM line

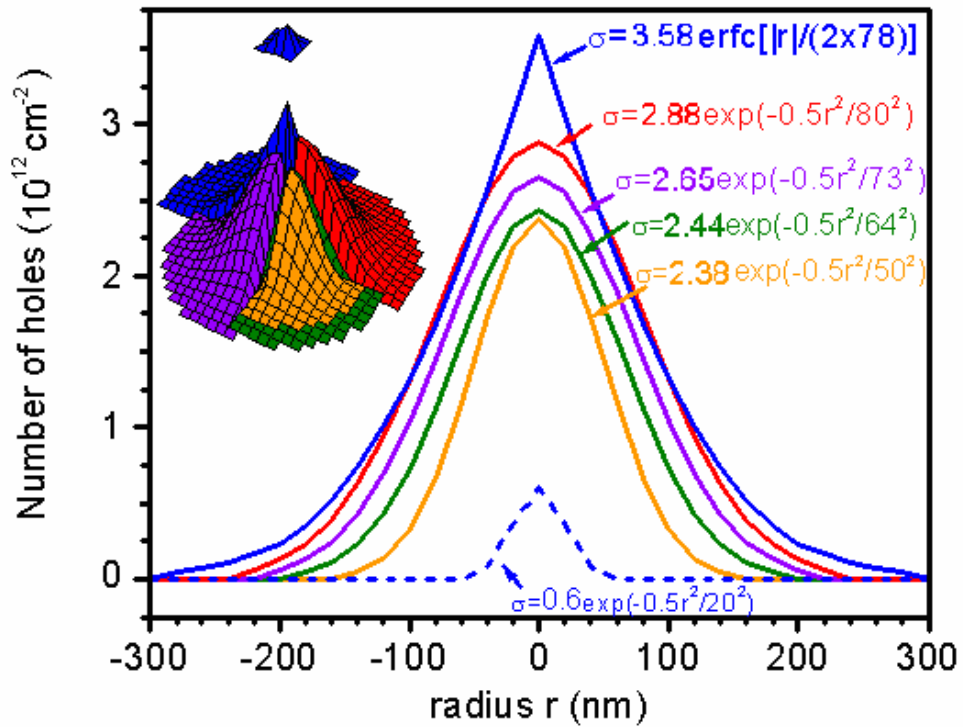


Figure 4.15. The cross-sections of the 2D complementary error function distribution and the 2D Gaussian distributions that fit experimental nc-AFM line profiles shown in Figure 4.14. The dashed curve corresponds to the hole distribution at sample surface. The inset shows schematics of these distributions.

profiles. The dashed curve corresponds to the distribution of holes at the sample surface, which includes 15 holes. It should be noted this charge is much less than the charge detected 11 minutes after injection of holes onto the surface of the control SiO₂ sample, which is 111 holes. This result can be explained by either a faster surface charge dissipation that was due to the higher density of surface states produced by ion implantation or repulsive electrostatic forces exerted by holes in the nanocrystal layer, or by insufficient surface charging since most holes were injected into the nanocrystal layer during charge injection. Except for the fitting of the first nc-AFM profile, holes distributed at sample surface were found to be negligible. In addition, it is very interesting that 15 charges can lift the peak of the nc-AFM profile up 5 nm (Fig. 4.14, from hollow circles), while electrostatic simulation indicated that they would be almost below the detection limit of nc-AFM if they were located on the surface of the control SiO₂ sample. This fact revealed an interesting feature of nc-AFM in detecting electrostatic force: the detection sensitivity increases with tip-sample distance (See chapter 5). With proper design, this feature may be employed to achieve single charge detection.

The evolution of charge distribution in the nanocrystal layer can be explained as follows: The initial charge distribution (2D complementary error function distribution) was similar to a cone, with very high number density of holes at the center. It could be inferred that both the vertical and lateral electric fields were strongest in the central area, and so were the tunneling probabilities. The number of tunneling events is proportional to both local number density of holes and tunneling probability, so the self-field driven diffusion in the lateral direction resulted in reduced peak but elevated side in the charge

distribution (evolving toward Gaussian distribution). At the same time, vertical charge dissipation reduced the total charge in the nanocrystal layer, which resulted in shrinking of the charge distribution. However, it was noticed that after the charge distribution evolved into a Gaussian distribution, the number density of holes dropped at an even smaller rate in the central area than that in the edge area. If this was not an error arising from the electrostatic simulation, we tend to believe the dominant vertical dissipation direction was toward the substrate, and the dissipation rate could be limited by the total number density of oxide defects.

Figure 4.16 shows the quantity of detected holes in the nanocrystal layer as a function

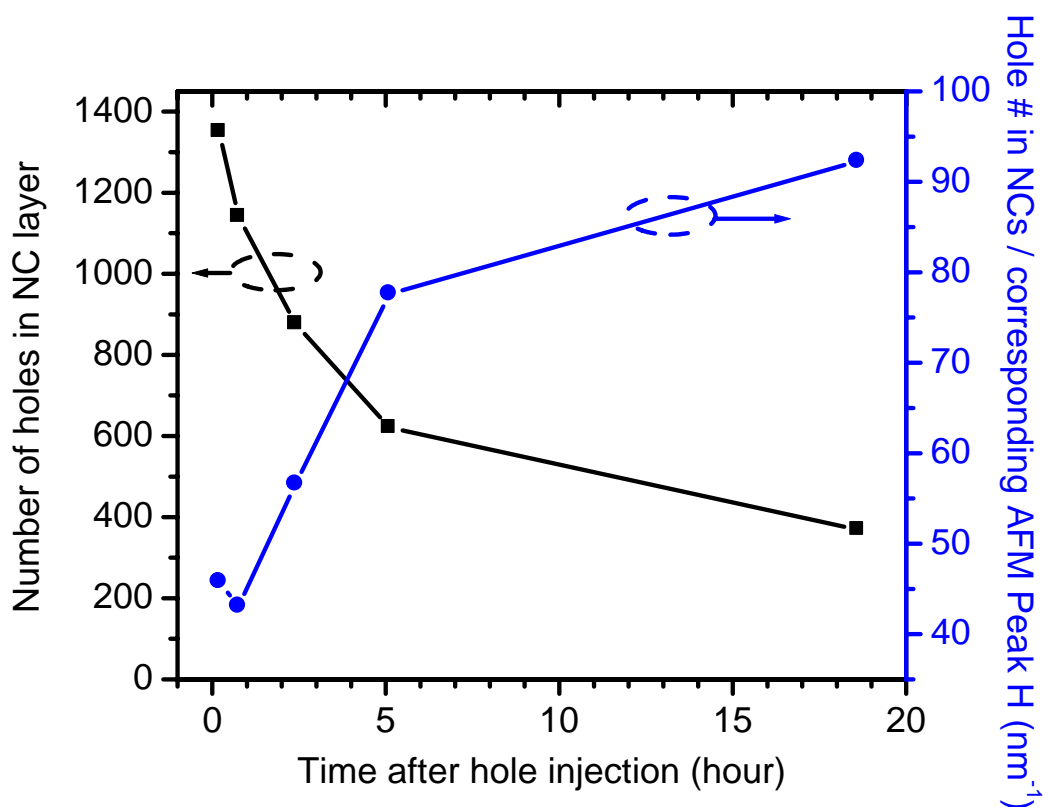


Figure 4.16. Quantity of detected holes in the nanocrystal layer as a function of time as determined from the simulation results (squares) and the corresponding ratios of charge number over nc-AFM profile peak height (circles).

of time determined from simulation. 1351 holes were detected, with 369 left after 18.4 hours. Generally the corresponding ratios of charge number to peak height of nc-AFM profile increases when the peak height decreases, ranging from 43 to 92.5 nm⁻¹. It is thus inaccurate to use peak height of nc-AFM signal to represent total local charge, otherwise the change of total charge will often be overestimated. A decrease was also noticed from the first to the second data point, which was attributed to the different type of charge distributions mentioned above. In another words, nc-AFM is more sensitive to Gaussian charge distributions than to complementary error function distributions.

The evolution of the Gaussian distribution of holes in the Si nanocrystal layer is shown in Fig. 4.17. The areal number density of holes in the central area decreased with a

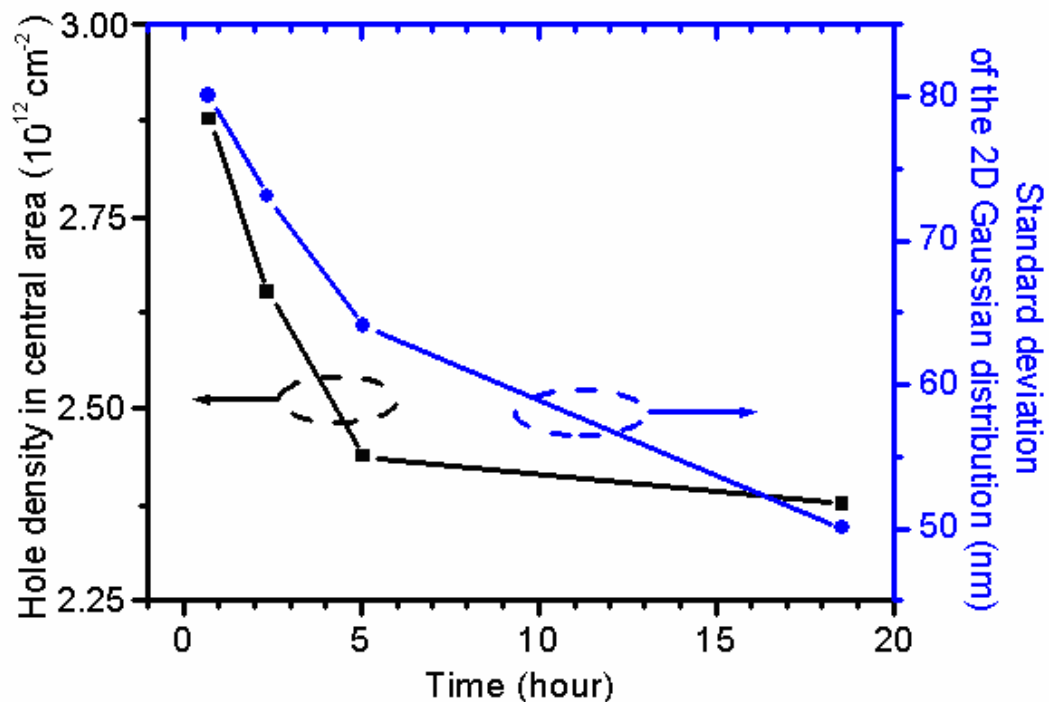


Figure 4.17. The evolution of Gaussian charge distributions in the Si nanocrystal layer.

smaller rate compared to that accompanying the transition from complementary error function distribution to Gaussian distribution, while the standard deviation of the Gaussian distribution shrinks noticeably. It should be noted that the total charge of the 2D Gaussian distribution was given by

$$Q = 2\pi\sigma_{\max} \cdot S^2. \quad (4.2)$$

So the shrinking of standard deviation played a more important role in reducing the total charge. We attribute the decrease of the spatial extent of the charge distribution to both the vertical dissipation that brought holes back to the sample surface followed by a fast lateral dissipation through surface states and the vertical dissipation that trapped holes in deeper defects. The latter was probably more important and was limited by the number density of deep defects, which made it more effective for the dissipation of holes at the edge of the distribution, as discussed above.

The quantity of detected holes in the nanocrystal layer as a function of time was re-plotted in Fig. 4.18 with logarithmic scale in either axis. Fig. 4.18 (a) verifies the argument made in the analysis of Fig. 4.12(c): charge dissipation rate is slower than exponential decay. Unlike Fig. 4.12(d), a logarithmic dependence of charge quantity on time was found to be quite accurate. Considering that the peak values of nc-AFM profiles cannot represent total charge accurately, this result is obviously more convincing and is consistent with previous capacitance decay measurements in Chapter 2.

4.8 Temperature dependence

At room temperature, more than 2/3 of the total charge dissipated within 18.4 hours. However, because of the continuously decreasing rate of charge dissipation due to the

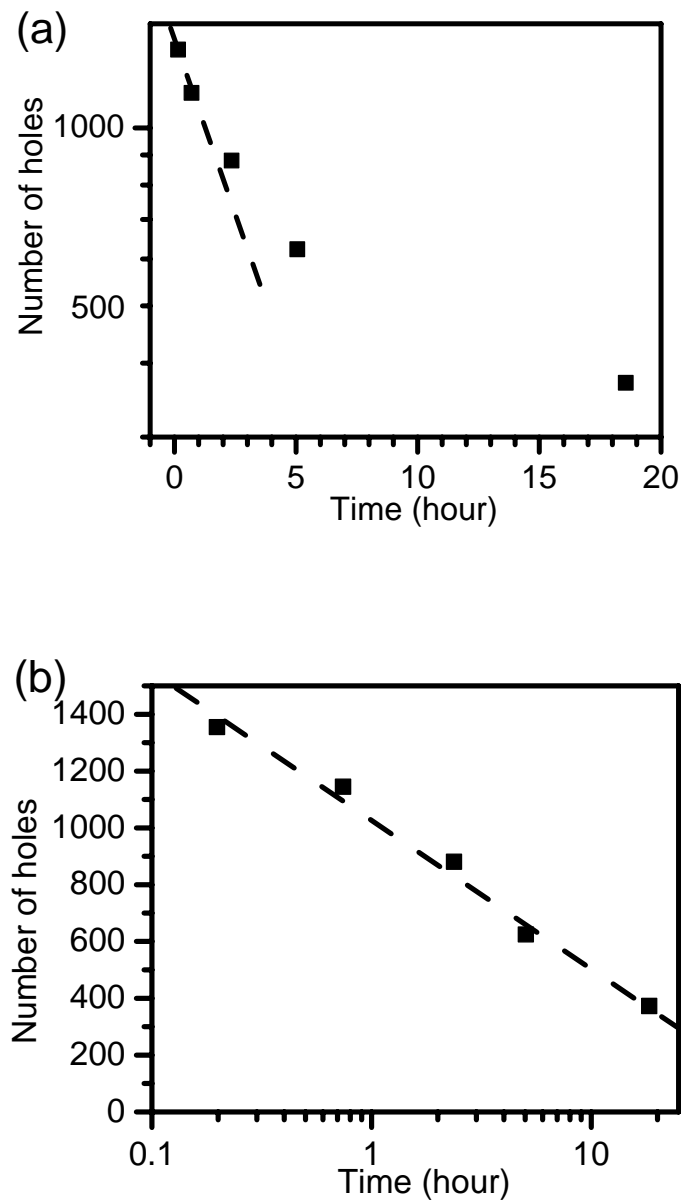


Figure 4.18. Quantity of detected holes in the nanocrystal layer as a function of time as determined from the simulation results, re-plotted with logarithmic scale in (a) vertical axis and (b) horizontal axis. The charge dissipation rate is slower than the exponential decay. A logarithmic dependence of charge quantity on time approximately matches the charge dissipation process.

decreasing of self-produced electric field and blocking of dissipation paths toward the substrate, a much longer time was anticipated before complete charge dissipation. Unlike

STM, minor manual adjustments are needed from time to time during charge imaging experiments with nc-AFM, which makes it inconvenient to observe a charge dissipation process that could last several days. So the charging experiments were performed at elevated temperatures as an alternative way to study the complete charge dissipation process as well as provide some reference regarding high temperature charge retention characteristics.

Figures 4.19 and 4.20 show the retention characteristics of holes at 400 K and 500 K, respectively. At 400 K it took 75 minutes for a similar hole dissipation process as that

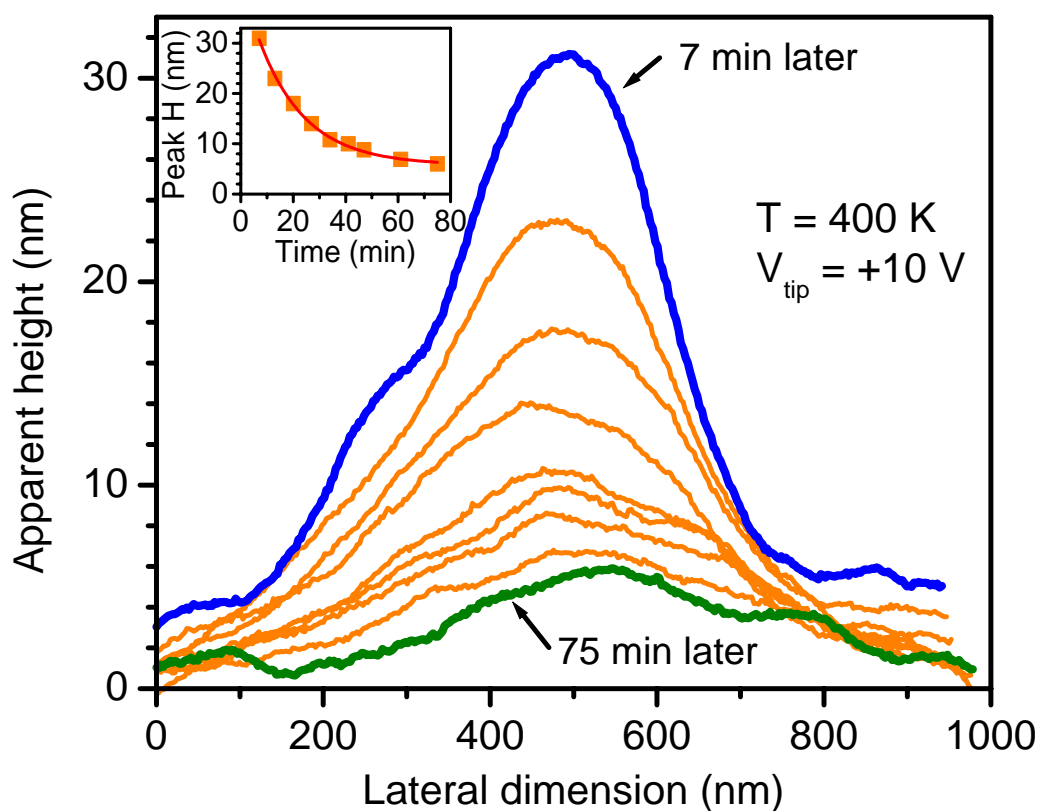


Figure 4.19. Series of line profiles showing the dissipation process after charge injection at +10 V at 400 K. The first trace was taken approximately 7 min after the charge injection, and the last was taken after 75 min. Inset shows the decrease of the peak height with time. A first order exponential decay fit gives $y = 5.77 + 36.9e^{-x/17.84}$.

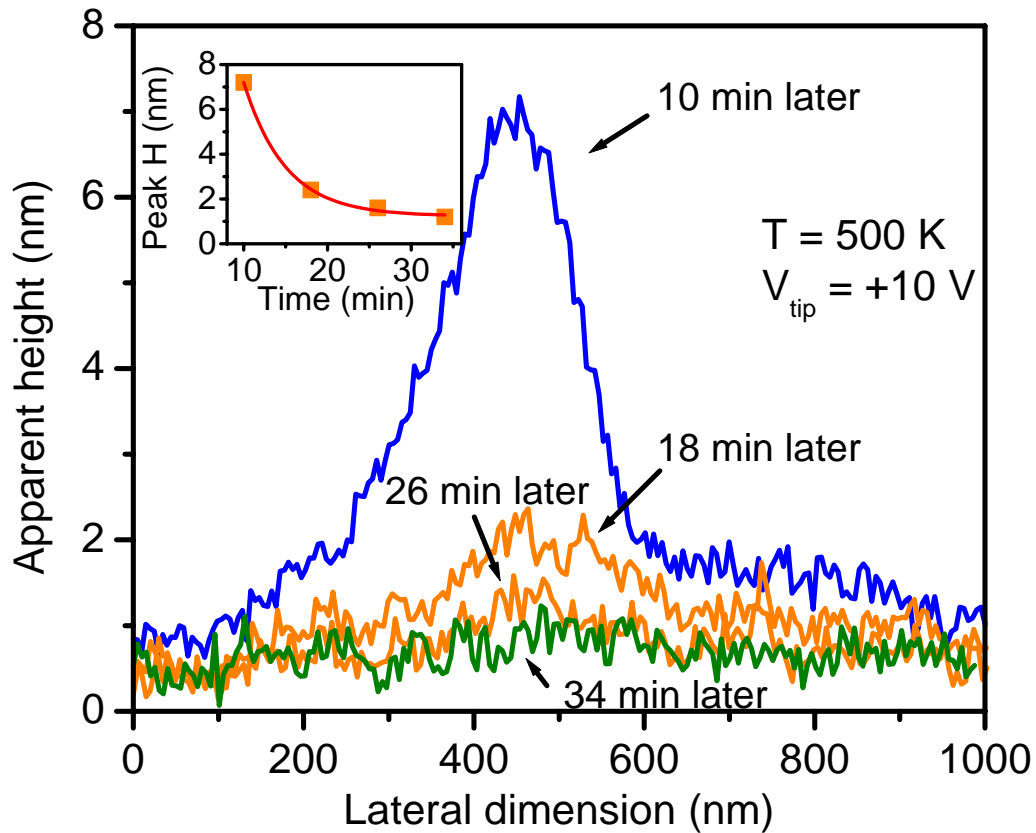


Figure 4.20. Series of line profiles showing the discharging process after charge injection at +10 V at 500 K. The first trace was taken approximately 10 min after the charge injection, and the last was taken after 34 min. Inset shows the decrease of the peak height with time. A first order exponential decay fit gives $y = 1.24 + 44.14e^{-x/4.99}$.

happened at room temperature to accomplish, while the whole dissipation process only took about half an hour at 500 K. This data not only presents holes as a possible choice for memory devices that could work at high temperature, but also opens the door of further study on charge tunneling mechanisms.

The question of the charge tunneling mechanism and the determination of relevant parameters such as energy barrier height and life time is a difficult one. The results from variable temperature charging experiments can be used to test possible mechanisms

through modeling of the charge diffusion processes. In addition, a clearer understanding of the theoretical model will help to improve the designs of nanocrystal memory devices and provide predictions of memory operation (e.g., extrapolate room temperature retention characteristics from high temperature measurements).

4.9 Summary

In this chapter, UHV nc-AFM was used to inject charges into a Si nanocrystal layer and monitor the subsequent charge dissipation processes, and was proved to be an effective tool for microscopic charge analysis. Through electrostatic simulation of nc-AFM scanning, quantitative information such as total charge, charge distribution, and evolution was extracted from time-dependent nc-AFM signals. It was demonstrated that holes have much longer retention time than that of electrons. In addition, the lateral dissipation was noticed to be very limited and charge loss was primarily attributed to vertical dissipation.

In the conventional continuous floating gate memories, electrons are commonly selected as stored charges [Fig. 4.21(a)]. By replacing the continuous floating gate with discrete silicon nanocrystals, a very thin tunnel oxide can be applied, thus making hole storage an interesting possibility. Holes showed much better retention characteristics in the device structure that was proved to be quite leaky for electrons, and the extremely small lateral dissipation rate can help to keep stored holes underneath the gate area, making nanocrystal memory programming with holes [Fig. 4.21(b)] a possible choice in further device scaling.

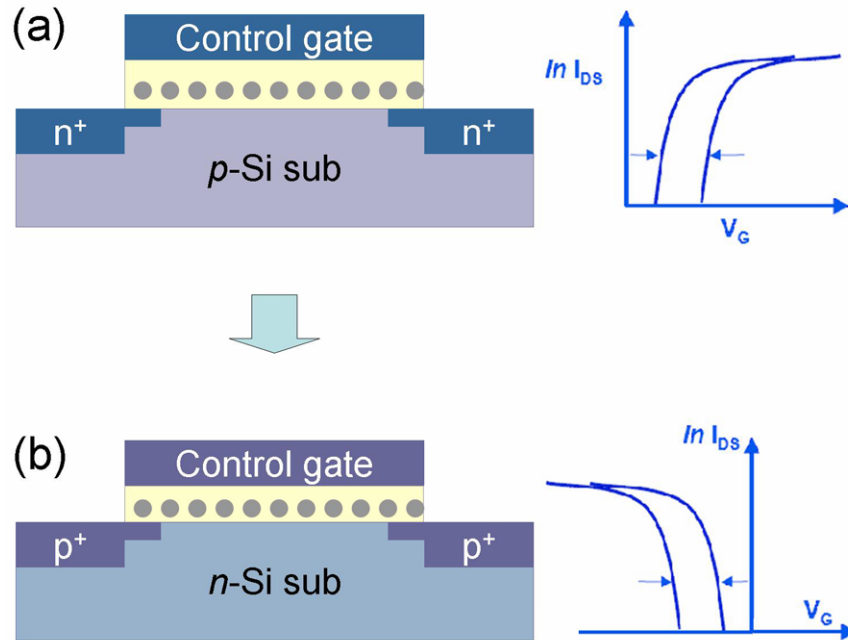


Figure 4.21. Schematics of an n -channel (a) and a p -channel (b) silicon nanocrystal floating gate memory device and the corresponding turn-on characteristics with and without electrons/holes in the nanocrystal floating gate.

The biggest concern regarding this idea is hole induced oxide degradation, which is also a general concern for p^+ -poly Si gated p -MOSFETs with ultra-thin gate oxides. However, it has been found that the oxide degradation caused by the hole direct tunneling strongly depends on the conditions of hole injection such as hole energy, hole fluence and oxide field. Cold hole injection from the inversion layer does not affect oxide reliability.¹¹² Endurance characteristics of a p -channel Si nanocrystal memory device working with low energy holes in the direct tunneling regime did not show hot carrier degradation within 10^5 write/erase cycles.⁸³ More experimental work is needed to test the feasibility of the p -channel Si nanocrystal memory working with holes.

Chapter 5

Improved models for quantitative charge imaging by noncontact atomic force microscopy

5.1 Introduction

In chapter 4 conductive tip nc-AFM was proven to be a sensitive tool for microscopic charge analysis. 3D electrostatic simulation was employed to extract quantitative information from experimental results, which becomes the basis for further analysis of charging and discharging mechanisms. For this purpose, a model that can describe tip-sample interaction as accurately as possible is always needed.

Various methods, from parallel capacitor models to complex numerical simulations, have been presented. Elizabeth Boer approximated the conductive tip as a grounded, metallic sphere, so the electrostatic force between the tip and local charges can be calculated by summing up all the interactions between the charges and their image charges within the metallic sphere, which is an application of classical method of images. Based on this, two electrostatic models were suggested to describe noncontact mode operation and tapping mode operation, respectively. For simplicity, local charges were always supposed to distribute homogeneously with some disk area. The effects of dielectric layers, air damping, as well as charges in the substrate, etc., were all ignored. These factors were listed at the end of the simulation work but not solved.¹⁰⁹

In this chapter we describe an improved model for quantitative charge imaging by nc-AFM. The dramatic influence of dielectric environment was included with a method of

images algorithm for multiple interface electrostatic problems. Space charge distribution in Si substrate was calculated and proved to be an unimportant factor in most cases. With the help of the self-installed UHV nc-AFM system, the problem of air damping was completely removed, and the electrostatic simulation could be focused on noncontact mode operation. In addition, we believe Gaussian distribution is more realistic in the discharging process and used that to replace disk distribution in most situations.

5.2 Electrostatic model

Figure 5.1 shows a schematic of charge imaging by non-contact AFM. The conical tip is usually highly doped and even coated with a thin layer of metal, and most induced surface charges are distributed at the end of the tip so it can be approximated as a metallic sphere with satisfactory accuracy.

Noncontact AFM usually involves a sinusoidal excitation of the cantilever with a frequency close to or at the main resonant frequency

$$\omega_0 = \sqrt{\frac{k}{m}} \quad (5.1)$$

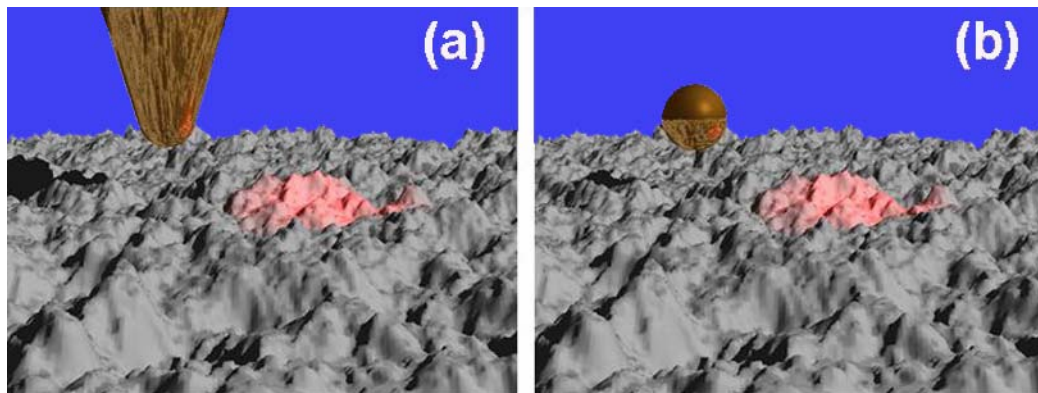


Figure 5.1. Computer-generated schematic of charge imaging experiment by nc-AFM (a) and the electrostatic model in which the tip was approximated as a grounded, metallic sphere (b).

A detailed theoretical description of nc-AFM can be started from the equation of motion:¹¹³

$$\frac{\partial^2 z}{\partial t^2} + \frac{\omega_0}{Q} \frac{\partial z}{\partial t} + \omega_0^2 (z - z_0) = A_0 \omega_0 \cos(\omega \cdot t), \quad (5.2)$$

where z and z_0 are the momentum and average tip-sample distance, respectively. Q is determined by the damping factor γ :

$$Q = \frac{m\omega_0}{2\gamma}. \quad (5.3)$$

The Q factor is usually below 100 for liquids, air, or other gases, but can be more than 10^5 in UHV. The steady-state solution of the equation for the forced oscillator is

$$z(t) = z_0 + A \cos(\omega \cdot t + \alpha) \quad (5.4)$$

with amplitude $A = \frac{A_0 \omega_0^2}{\sqrt{(\omega_0^2 - \omega^2)^2 + 4\gamma^2 \omega^2}}$ and phase shift $\alpha = \arctan \frac{2\gamma\omega}{\omega^2 - \omega_0^2}$.

Under the influence of a force field, the oscillation is usually not harmonic. But for $A_0 \ll z_0$, force can be substituted by a first order Taylor approximation, and the cantilever will behave as if it has a modified spring constant

$$k' = k - \frac{\partial F}{\partial z}. \quad (5.5)$$

An attractive tip-sample interaction (negative) with $\partial F/\partial z > 0$ will thus “soften” the cantilever, while a repulsive interaction (positive) with $\partial F/\partial z < 0$ will make the cantilever “stiffer.” The change of the effective spring constant will modify the resonant frequency of the cantilever:

$$\omega'_0 = \omega_0 \sqrt{1 - \frac{1}{k} \frac{\partial F}{\partial z}} \quad \text{or} \quad (5.6)$$

$$\frac{\Delta\omega_0}{\omega_0} \approx -\frac{1}{2k} \frac{\partial F}{\partial z} \text{ if } |\partial F/\partial z| \ll k, \quad (5.7)$$

which is generally satisfied. The modification of the resonant frequency will further change the oscillation amplitude and phase shift. All of these quantities can be monitored in experiments depending on the specific feedback mechanism.

In the operation of ambient nc-AFM, the driving frequency is slightly off resonance. The feedback mechanism monitors the oscillation amplitude. A change in the force gradient will bring a shift of resonant frequency ($\Delta\omega_0$) and a change in oscillation amplitude (ΔA). By maintaining a constant ΔA , the contour of a constant force gradient can be mapped. This method is called ‘‘slope detection.’’ UHV nc-AFM uses an alternative method call ‘frequency modulation’ (FM) in which a high-Q cantilever is kept oscillating at its resonant frequency utilizing a positive feedback. Many methods such as digital frequency counters and phase-locked loops can be applied to measure the oscillator frequency with very high precision.¹¹³

No matter which method is applied, a constant shift of resonant frequency which corresponds to a constant force gradient is maintained, so the dynamic problem was simplified to an equation

$$\left(\frac{\partial F_z}{\partial z}\right)_{total} = \left(\frac{\partial F_z}{\partial z}\right)_{vdW} + \left(\frac{\partial F_z}{\partial z}\right)_{electrostatic} \approx -2k \frac{\Delta\omega_0}{\omega_0}. \quad (5.8)$$

The van der Waals force gradient was computed using the Lennard-Jones pair potential, assuming a spherical shape for the tip and a flat plane for the sample surface, which is valid for $z \ll R_{tip}$.¹⁰⁹ The computation of electrostatic force gradient is the especially important in the simulation of charge imaging experiments. A method of images

algorithm was applied to achieve a better accuracy in the estimation of total charge, charge distribution, and evolution.

5.3 Method of images algorithm for multiple interface electrostatic problems

In principle, all electrostatic problems can be solved via a Poisson equation that incorporates the matching of boundary conditions at all interfaces of the system. But this is usually a difficult task in practice. Numerical methods such as Poisson solver may be applied with well-defined boundary conditions. In some special situations, however, the method of images is much more convenient and efficient as a non-iterative approach. For example, an image point charge could be used to solve the problem in the case of a point charge placed near a conductive plane. A similar approach can be applied to a conductive sphere¹¹⁴ or a planar dielectric interface.^{115,116} For a dielectric sphere, the image charge is no longer a point charge.¹¹⁷ Such a situation makes calculation complex and will not be discussed in this paper. When there are two interfaces, an infinite series of point image charges is theoretically required.¹¹⁸ But in practice, the magnitudes of these point image charges decrease rapidly, and usually inclusion of several of them is enough to achieve good accuracy. However, another problem appears along with the increase of total number of interfaces: it is not straightforward to specify the locations and magnitudes of image charges for more than one interface.^{119,120} When the number of interfaces is increased, the image charge specification becomes more difficult and tedious so that the method of images loses its biggest advantage: simplicity.

In order to make the method of images work to an advantage in complicated situations, we have employed an efficient algorithm similar to the “ray-tracing” approach to find image charge positions and magnitudes conveniently. While ‘ray-tracing’ approach generally applies to multiple planar interfaces, this algorithm can handle multiple planar interfaces as well as conductive spheres. Some examples are discussed to illustrate the feasibility of this method. In the discussing the influence of space charge in Si substrate on the charge imaging experiments, an iterative finite difference approach is applied with the aid of the algorithm, and proved to be effective.

5.3.1 Two and three dielectric layers

As described in the literature,¹¹⁶ the method of images can be extended to handle boundary-value problems with dielectrics. Figure 5.2 shows the simplest case including a semi-infinite dielectric layer ε_1 and another semi-infinite dielectric layer ε_2 with a planar interface at $z=0$. A point charge q is embedded in dielectric layer ε_1 . The corresponding potential distribution, subject to the boundary conditions at the interface, can be proved analytically to be

$$\phi = \begin{cases} \frac{1}{4\pi\varepsilon_1} \left(\frac{q}{R_1} + \frac{q'}{R_2} \right) & , \quad z > 0 \\ \frac{1}{4\pi\varepsilon_2} \frac{q''}{R_1} & , \quad z < 0 \end{cases} \quad (5.9)$$

where

$$q' = r_{12}q, \quad q'' = (1 - r_{12})q, \quad r_{12} = (\varepsilon_1 - \varepsilon_2) / (\varepsilon_1 + \varepsilon_2).$$

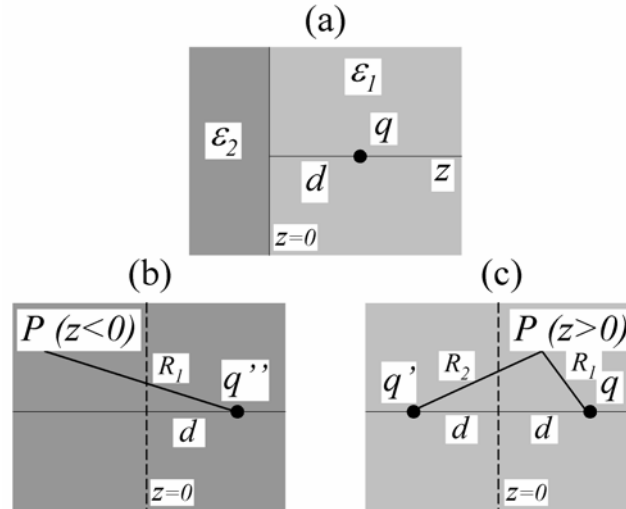


Figure 5.2. Method of images construction for a problem including a point charge and a planar dielectric interface. (a) Actual physical system of a point charge q at a distance d from the interface between two dielectric half-spaces. (b) The image charge q'' that gives field distribution in the left half-space. (c) The original point charges q and image charge q' that give field distribution in the right half-space. $q'=r_{12}q$, $q''=(1-r_{12})q$, and $r_{12}=(\epsilon_1-\epsilon_2)/(\epsilon_1+\epsilon_2)$.

With the application of image charges q' and q'' , the boundary is removed and the problem is simplified.

Figure 5.3(a) shows three dielectric layers with a point charge in the middle region. Figure 5.3(b), (c), and (d) indicate the image charges needed for calculation of electric field in regions *I*, *II* and *III* respectively. The validity of these results is demonstrated first, and the approach to find the image charges is discussed later. According to the uniqueness theorem, all boundary conditions should be met. This requires that i) electric potential vanishes at infinity; ii) the perpendicular component of the electric displacement D and the parallel component of the electric field E are continuous through the interfaces; and iii) there is only one singularity at the position of the original point charge. That the first requirement is met can be seen by considering the rapidly decreasing magnitude of

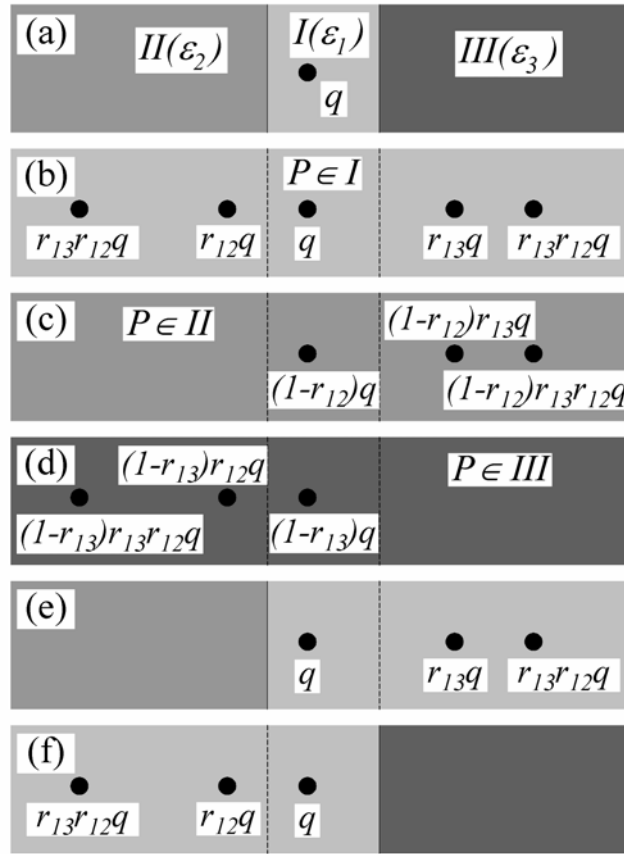


Figure 5.3. Method of images construction for a problem including a point charge between two planar dielectric interfaces. (a) Actual physical system. (b) The infinite series of charges that gives the electric field distribution in region I . There are in fact two series of image charges which can be specified in the following way: For one series the first image charge was put at the mirror image position of q with respect to the interface I/II , with magnitude multiplied by a factor r_{12} . The second image charge was put at the mirror image position of the first image charge with respect to the other interface I/III , with magnitude multiplied by a factor r_{13} . Such steps are repeated to produce new image charges with magnitudes multiplied by corresponding factors. For the other series the process is similar except that the first step is with respect to interface I/III . Due to limited space, only a finite number of image charges are shown in the figure. (c) and (d) show the infinite series of image charges that give field distribution in region II and region III , respectively. The charge positions correspond to that of q and all image charges to its right [for (c)] or left [for (d)] in (b), but charge magnitudes are multiplied by $(1-r_{12})$ [for (c)] or $(1-r_{13})$ [for (d)]. (e) and (f) show physical systems with an infinite series of charges and one dielectric interface. The positions and magnitudes of these charges correspond to those of q and all images charges to its right [for (e)] or left [for (f)] in (b).

the image charges on both sides of the original point charge. That the third requirement is met by the solution can be seen directly. Requirement ii) needs to be discussed in detail. Instead of direct proof, the result from Figure 1 and the superposition principle were utilized. Fig. 5.3(e) and (f) were introduced to describe the reasoning. In Fig. 5.3(e), there is only one dielectric interface, so superposition can be applied and the problem simplified to the case in Fig. 5.2. Since \mathbf{D} and \mathbf{E} produced by one point charge and its image charges meet requirement ii), the sum of them produced by multiple point charges and corresponding image charges still meets the requirement. A little more observation indicates Fig. 5.3(b) and (c) are exactly the solutions to Fig. 5.3(e) if the charges in Fig. 5.3(b) are used to calculate electric field in region *III* as well. Requirement ii) is thus met by \mathbf{D} and \mathbf{E} on both sides of the left interface, which are given by charges in Fig. 5.3(b) and (c), respectively. The same approach can be applied to the right interface with the aid of Fig. 5.3(g). With all three requirements satisfied, the result we obtained is the unique solution to electrostatic problem Fig. 5.3(a).

Figure 5.4 shows a slightly different problem in which a charge is located in region *III*. A broadly similar approach is used as in the situation in Fig. 5.3, with a difference that appears in the evaluation of requirement ii) at the right interface. In Fig. 5.4(f), which is introduced to describe the reasoning, point charges are distributed on both sides of the interface and need to be considered separately when compared with Fig. 5.2.

5.3.2 Method of images algorithm

The process to find solutions to problems involving two dielectric interfaces depends on finding a trial solution and verifying its correctness. This is difficult for more

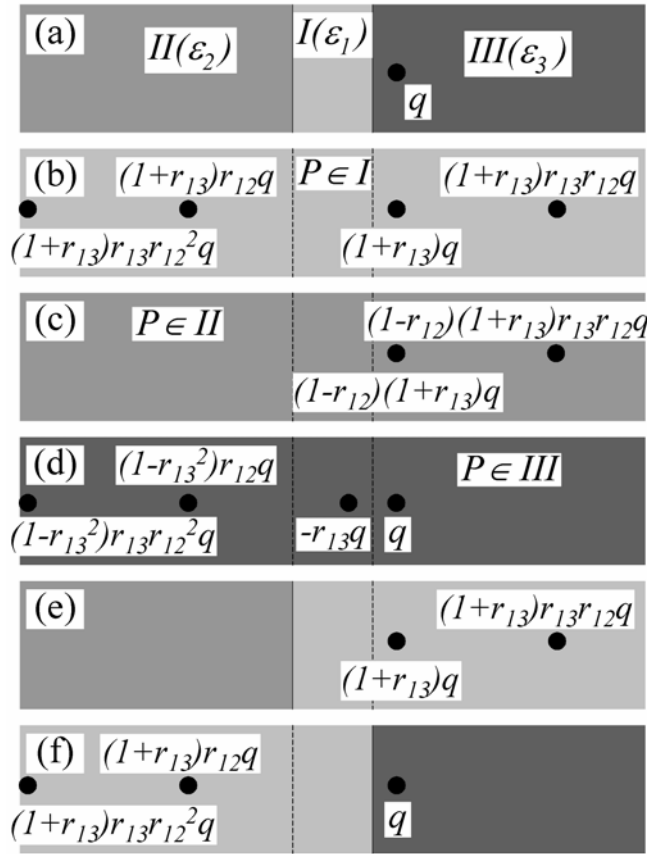


Fig. 5.4. Method of images construction for a problem including a point charge to the right of two planar dielectric interfaces. (a) Actual physical system. (b) The infinite series of charges that gives field distribution in region I , which can be specified in the following way: The first image charge is $(1+r_{13})q$ at the original position of q . The second image charge is put at the mirror image position of $(1+r_{13})q$ with respect to the interface I/II , with magnitude multiplied by a factor r_{12} . The third image charge is put at the mirror image position of the second one with respect to the other interface I/III , with magnitude multiplied by a factor r_{13} . Such steps are repeated to produce new image charges with magnitudes multiplied by corresponding factors. Due to limited space, only a finite number of image charges are shown in the figure. (c) and (d) show the infinite series of image charges that give field distribution in region II and region III , respectively. The positions of image charges not shown correspond to those image charges not shown on the right [for (c)] or left [for (d)] side in (b), but their magnitudes are multiplied by a factor $(1-r_{12})$ [for (c)] or $(1-r_{13})$ [for (d)]. (e) and (f) show physical systems with an infinite series of charges and one dielectric interface. The positions and magnitudes of those image charges not shown correspond to those image charges not shown on the right [for (e)] or left [for (f)] side in (b).

complex situations. The best general approach is therefore to apply a standard algorithm, if any, to find image charge positions and magnitudes. In the literature, there was a “ray-tracing” method that dealt with multiple planar interfaces. We introduced a similar algorithm that handles conductive spheres as well. Both methods were based on the classical method of images and nothing new in theory; the application is easy, but the deduction is not straightforward and need to be clarified as follows:

With further observation on Figures 5.3 and 5.4, a simple rule can be found for the generation of all image charge positions and magnitudes. It can be imagined that the original point charge is a “light source” and the dielectric interfaces act as “mirrors” with specified reflectivity and transmissivity. For an observer in region I of Fig. 5.3(a), the images of the “light source” he can see through the reflections of two interfaces are distributed exactly in the same way as in Fig. 5.3(b). In fact, no matter in which region the observer is located, the distribution of the “light sources” always corresponds to the set of image charges for the calculation of electric field in that region. Each time a reflection or transmission happens, the magnitude of the image charge is multiplied by a reflectivity r_{ij} or transmissivity $(1-r_{ij})$. Beyond the cases illustrated in Fig. 5.3 and Fig. 5.4, this rule is found to be a general rule for more complex situations. Based on this idea, a standard algorithm can be defined with repeated applications of the operation described in Fig. 5.2 to specify all image charge positions and magnitudes.

Suppose there are X dielectrics $\epsilon_1, \epsilon_2, \dots, \epsilon_i, \dots, \epsilon_X$ with such order in space. A point charge $q_1^i = q_0$ is embedded in ϵ_i . Initially the sets of point charges for electric field computation in all the dielectric layers can be expressed as:

$$S^1 = \{NULL\}, \quad \dots \quad S^{i-1} = \{NULL\}, S^i = \{q_1^i\}, S^{i+1} = \{NULL\}, \quad \dots \quad S^X = \{NULL\}. \quad (5.10)$$

Such oversimplification ignores sample structure information and does not meet the continuity condition for \mathbf{E} and \mathbf{D} at interfaces. Thus we define an operation $O_n^{j \rightarrow k}$ for the point charge q_n^j (the n 'th point charge in S^j , $1 \leq j \leq X$, $n \geq 1$) with respect to the interface between layer ε_j and its neighboring layer ε_k . With the operation $O_n^{j \rightarrow k}$, a new image charge is added to each side as was done for the case in Fig. 5.2. Since there are two interfaces for layer ε_i , application of $O_1^{i \rightarrow i+1}$ followed by $O_1^{i \rightarrow i-1}$ leads to

$$S^1 = \{NULL\}, \quad \dots \quad S^{i-1} = \{q_1^{i-1}\}, S^i = \{q_1^i, q_2^i, q_3^i\}, S^{i+1} = \{q_1^{i+1}\}, \quad \dots \quad S^X = \{NULL\} \quad (5.11)$$

$$q_2^i = r_{i,i+1} q_1^i, \quad q_1^{i+1} = (1 - r_{i,i+1}) q_1^i, \quad q_3^i = r_{i,i-1} q_1^i, \quad q_1^{i-1} = (1 - r_{i,i-1}) q_1^i, \quad r_{ij} = (\varepsilon_i - \varepsilon_j) / (\varepsilon_i + \varepsilon_j),$$

where q_1^{i+1} and q_1^{i-1} are both at the original position of q_1^i , while q_2^i and q_3^i are at mirror image positions of q_1^i with respect to corresponding interfaces. The discontinuity of \mathbf{E} and \mathbf{D} at both interfaces calculated based on (5.10) is caused by q_1^i . It is cancelled by image charges produced in operations $O_1^{i \rightarrow i+1}$ and $O_1^{i \rightarrow i-1}$. A new image charge q_n^j helps to solve the discontinuity problem at the interface through which it is produced. However, it causes a new discontinuity at the other interface of layer ε_j unless the image charge belongs to S^1 or S^X , which corresponds to a set of image charges for an outermost layer of the overall structure. These new discontinuities are smaller than those presented before the operation because of decreased charge magnitudes and increased distances to corresponding interfaces. Similar operations can be repeated to replace these

discontinuities with even smaller ones until the unaccounted image charges are far away from interfaces and the charge magnitudes are negligible.

Conductive planar layers or spheres can also be incorporated into this algorithm conveniently, with appropriately modified operations. Since the electric field inside a conducting region is zero and such region always act as end regions, there is no need to define a set of point charges for electric field computation in the conductive region. The operation to generate image charges that give the electric field outside of a grounded conductive plane or sphere belongs to the classical method of images, which can be found in textbooks.^{115,116} For a conductive sphere at potential V , a point charge can be viewed as at the center of the sphere. The detectable charge in surrounded region ε_1 is

$$Q'' = 4\pi\varepsilon_1 R V . \quad (5.12)$$

For an isolated conductive sphere, the total charge must be kept constant. Whenever an image charge is produced through its spherical interface, another charge with the same magnitude but opposite sign must be put at the center of the sphere. All these arguments apply to planar conductive layers as well if they are treated as spheres with very large radii.

In summary, the algorithm to find image charge magnitudes and positions for multiple interface systems includes the following steps.

- i) Specify a set of charges for each dielectric layer (S^j), which can be used to calculate electric field in that layer. For a conductive sphere with known charge, the charge goes into the set for the surrounding dielectric region. This also applies to charges computed with formula (5.12).

- ii) For every original charge q_n^j , perform an operation $O_n^{j \rightarrow k}$ with respect to interface between ε_j and each of its neighboring layers ε_k .
- iii) For every image charge q_n^j , perform operation $O_n^{j \rightarrow k}$ with respect to interface between ε_j and each of its neighboring layers ε_k , except for the interface through which it is generated, which also means that no operation is performed for image charge q_n^j if j represents an end layer.
- iv) Repeat step iii) until the unaccounted image charges are far away from interfaces and/or the magnitude of these image charges are negligible.

5.3.3 Example

As a direct application of this algorithm, a notional example of a complex electrostatic problem that may be encountered in the simulation of local charge imaging experiments by nc-AFM is depicted in Fig. 5.5(a). There are 4 dielectric layers (including air/vacuum; space charge in the Si substrate is ignored here) and 3 conductive spheres. Two spheres represent metallic nanoparticles which have fixed charge of $+3q_0$ and 0, respectively. The other one represents a highly doped AFM tip, which is grounded. For convenience in showing results, the centers of all spheres were chosen to be in the same vertical plane, although other choices can be achieved with no extra calculation. A program based on the algorithm was written to find image charge set for each dielectric layer. Using these sets of image charges, the electric potential distribution as well as the force on the AFM tip was calculated directly, as shown in Fig. 4(b). The force gradient can be calculated at the same time (not shown). The black region (negative electric

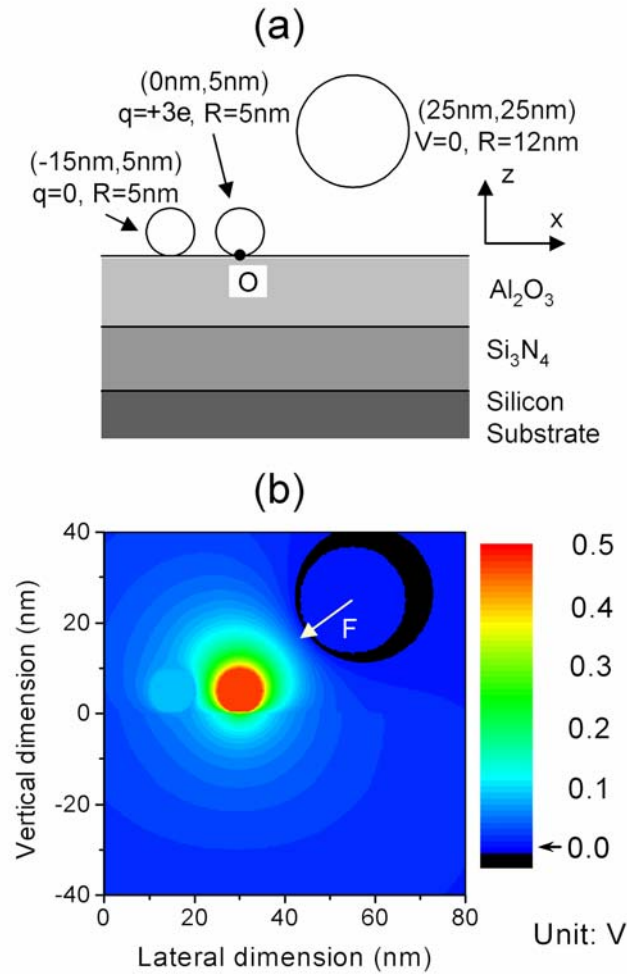


Figure 5.5. (a) An electrostatic geometry representing an apparatus for local charge imaging by conductive-tip nc-AFM. The sample structure includes two metallic nanoparticles with $R=5$ nm which sit on Al_2O_3 ($\epsilon_r=9.0$, thickness=15 nm) / Si_3N_4 ($\epsilon_r=7.6$, thickness=15 nm) / Si ($\epsilon_r=11.7$). For simplicity, the conductive tip is grounded and assumed to be a sphere with radius $R=12$ nm. The centers of all spheres are chosen to be in the same vertical plane. (b) Profile of electric potential distribution and electrostatic force on the tip. $F_x=-1.592\times 10^{-13}$ N. $F_z=-1.174\times 10^{-13}$ N.

potential) is due to negative induced charges at the tip surface. In this example, the process of image charge generation was stopped when the number in a set exceeded 10,000. With a 1GHz Intel Pentium III processor, it took 5 seconds to generate image charges and 40 seconds to finish the entire calculation. For comparison, it took a standard

Poisson solver (Quick Field) 4 seconds to solve a similar problem in 2D numerically with a 2.3 GHz Pentium IV processor. We did not find a suitable 3D solver, but generally the transition from 2D to 3D costs much more time. Compared with numerical methods, the method of images algorithm provides fast solution that is differentiable, which is very convenient to use in the simulation of charge imaging by nc-AFM or EFM.

5.4 Effects of dielectrics and space charge in Si substrate

The effects of dielectrics were shown in Fig. 5.6, in which the AFM images due to 99 basic charges with different sample geometries were simulated. The distance between nanocrystal layer and Si substrate was chosen to be 5 nm, and the total oxide thickness was chosen to be 15 nm and 5 nm, the values for the unetched and etched nanocrystal samples in chapter 2. In the charging experiment of the unetched sample, electrons or holes were primarily injected from the substrate, followed by diffusion toward the center of the charged area. In the charging experiment of the etched sample, holes or electrons were primarily injected from the tip, but most of them tunneled into the substrate before diffusion to a larger area in the nanocrystal layer. For both directions of charge injection, charges in the nanocrystal layer were limited to a relatively small area. Considering the size of the tip, a 2D Gaussian distribution with $\sigma_{max} = 4 \times 10^{12} \text{ cm}^{-2}$ (larger than the σ_{max} observed in the charging experiments on the nanocrystal sample with thick oxide layer and similar to the σ_{max} observed in C-V measurements) and $S = 20 \text{ nm}$ (see curve A) were specified. If the dielectric constants of SiO_2 and Si were both ignored and set as 1, the protrusions in simulated AFM images are larger than 10 nm, indicating that the charges can be detected easily in both sample geometries. If only the dielectric constant of SiO_2 is

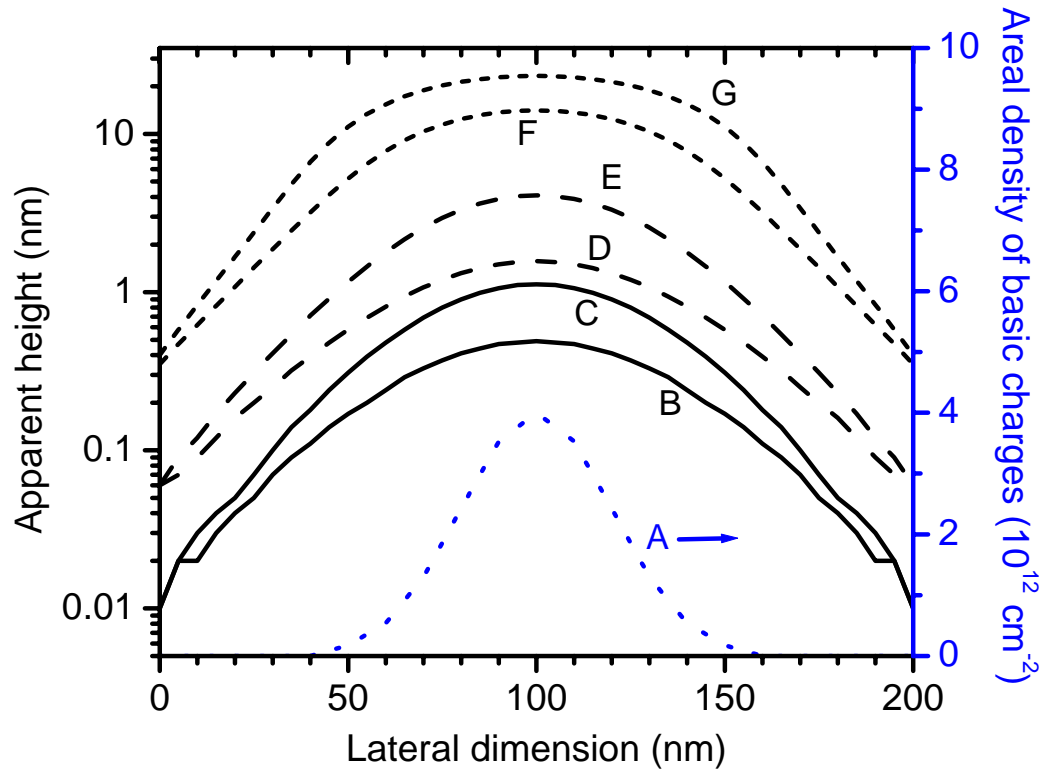


Figure 5.6. Simulated nc-AFM line profiles for a Gaussian distribution of 99 basic charges (curve A, $\sigma_{\max} = 4 \times 10^{12} \text{ cm}^{-2}$, $S = 20 \text{ nm}$) on a nanocrystal layer 5 nm from the substrate. The total thickness of the SiO_2 layer is 15 nm for curves B, D, and F, and is 5 nm for curves C, E, and G. Solid, dashed, and short dashed curves indicate simulation results by assuming relative dielectric constants of Si and SiO_2 to be 11.7 and 3.9, both 3.9, and both 1.0, respectively.

included in simulation, the protrusions drop to a few nanometers, both just detectable considering corresponding sample surface roughness. However, if both dielectric constants were considered in the simulation, the protrusions drop below about 1 nm, inevitably immersed in the background noise of the surface roughness. This result clearly shows the importance of considering dielectric environment in the electrostatic simulation, and provides a probable explanation to the fail of charging experiments on the nanocrystal samples with thin tunnel oxide layers.

To evaluate the influence of space charge in Si substrate, 3D space charge distribution was calculated and included in the electrostatic simulation of nc-AFM. In the example shown in Fig. 5.7, two charged nanoparticles (15 holes each) with a spacing of 60 nm sit on 12 nm of SiO₂ film on *p*-Si substrate. The self-consistent calculation of charge distribution in the substrate was achieved by the combination of numerical method and method of images algorithm, which shows fast convergence [Fig. 5.7(a)]. Two insets show the calculated space charge distribution for substrate doping concentrations of 10¹⁷ cm⁻³ and 10¹⁸ cm⁻³, respectively. It was noticed that the space charge region shrinks as the doping concentration increases, a phenomenon similar to the dependence of maximum depletion layer width versus substrate doping concentration for MOS diode. Simulated nc-AFM images with consideration of the space charge did not show obvious difference from the result that only considers dielectric environment [Fig. 5.7(b)]. The total space charge is nontrivial. In fact, it is always the same as the total localized charge on/in the SiO₂ layer. But since the latter in the charging experiments generally cannot induce strong inversion in the substrate, the space charge is distributed in a broad depletion region, producing an almost homogeneous electric field which is hard to be detected by nc-AFM. In addition, the space charge was below the sample surface and its electrical field was further canceled by the polarized charge at the interfaces. For all these reasons, space charge in the substrate is generally negligible, with possible exceptions of strong inversion or extremely high doping concentration.

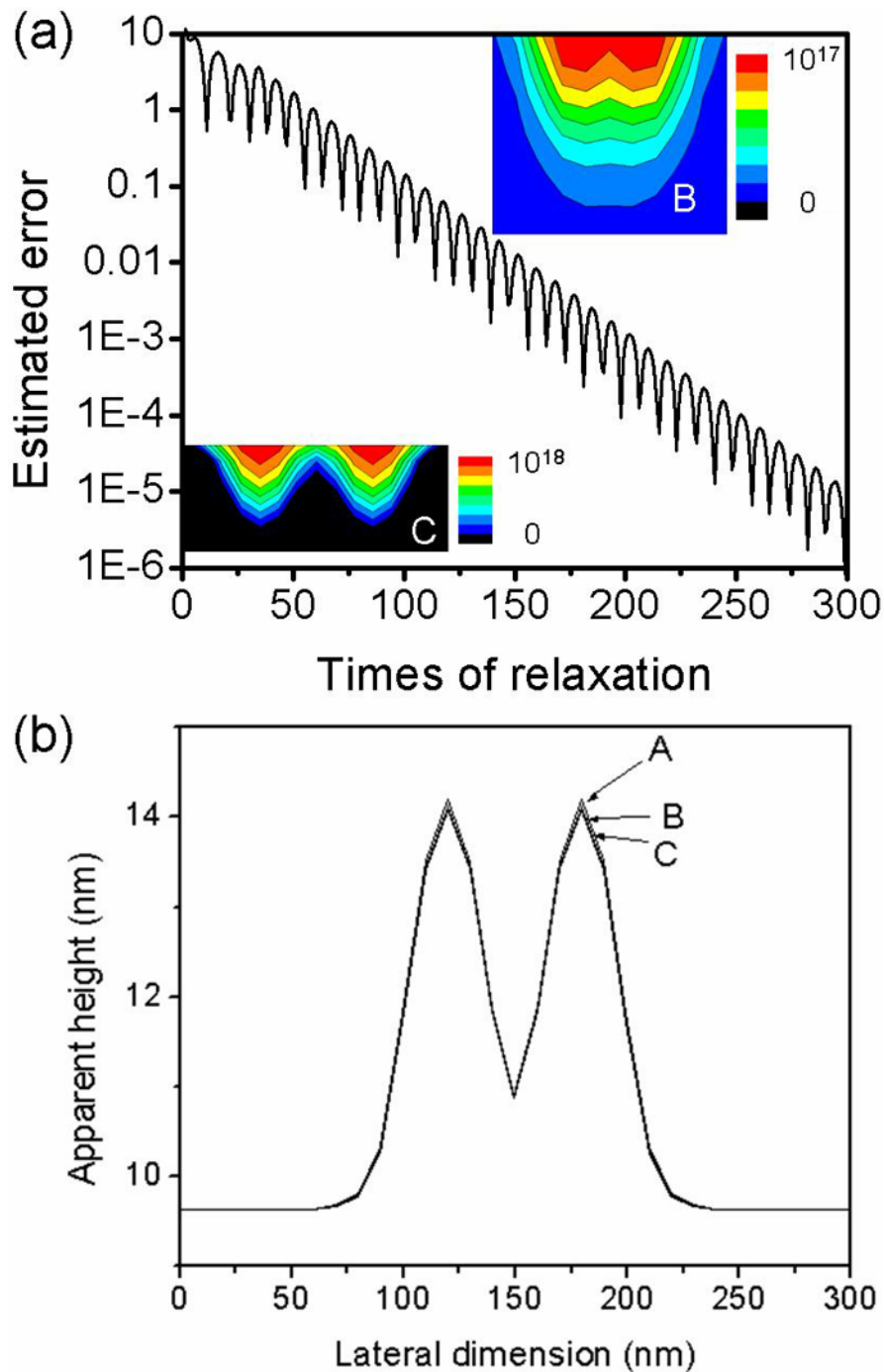


Figure 5.7. (a) Estimated error as a function of number of iterations in a typical electrostatic calculation of 3D space charge distribution in Si substrate. Inset B and C show cross section of calculated space charge distribution (unit: cm^{-3}) due to two charged nanoparticles (15 holes each) with a spacing of 60 nm on 12 nm of SiO_2 film on p -Si substrate. Inset B: $N_A = 10^{17} \text{ cm}^{-3}$, vertical dimension is 50 nm, lateral dimension is 200 nm. Inset C: $N_A = 10^{18} \text{ cm}^{-3}$, vertical dimension is 14 nm, lateral dimension is 140 nm. (b) Simulated nc-AFM profiles. A: Only includes the influence of dielectric environment. B, C: Also include the influence of space charge in Si substrate shown in inset B and C in (a).

5.5 Charge detection sensitivity and lateral resolution

Figure 5.8 shows minimum detectable number of basic charges as a function of the tip-sample spacing. An error of ~ 0.7 nm was used in the determination of the minimum detectable charge magnitude, which will produce a protrusion larger than 0.7 nm at a specified scanning height. The charge detection sensitivity was observed to increase as the height increases. This non-intuitive result can be explained by the long-range nature of electrostatic force and smaller gradient of force gradient at larger tip-sample spacing

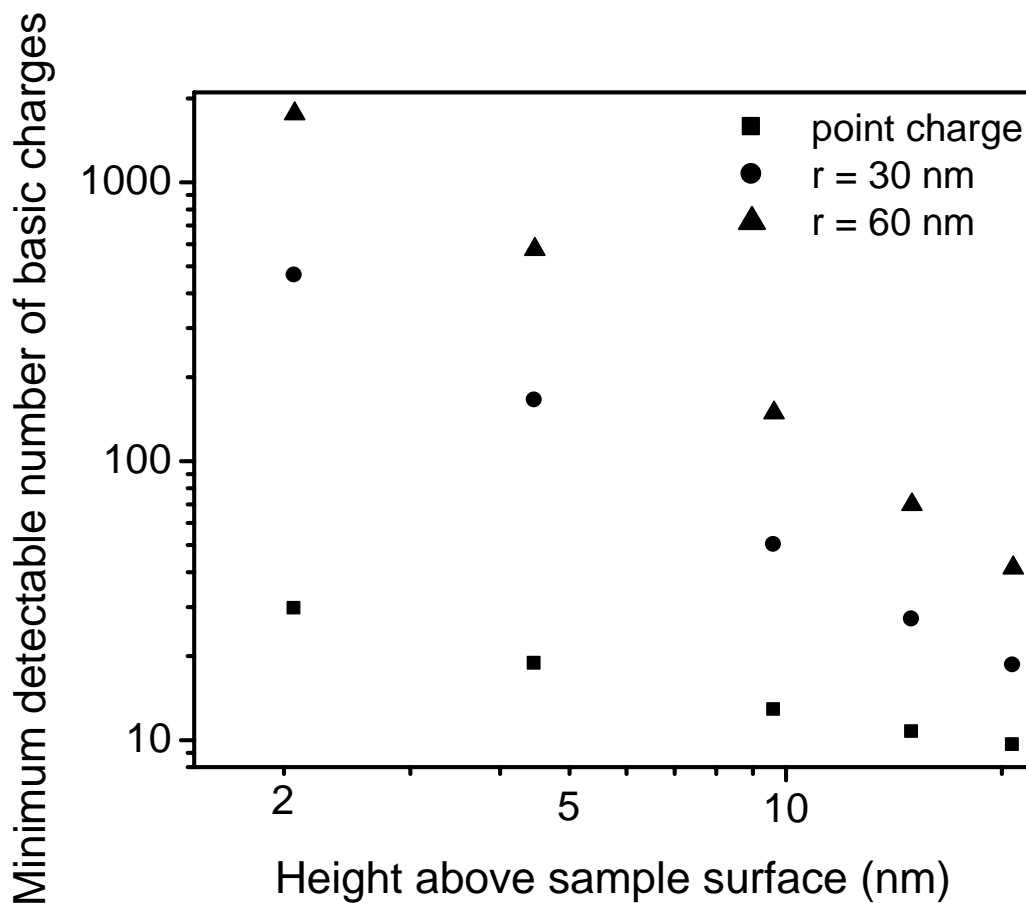


Figure 5.8. Minimum detectable number of basic charges as a function of the tip-sample spacing. Tip radius is 52.5 nm. Charges are distributed homogeneously in a disk area with $r=0, 30,$ and 60 nm on the surface of 12 nm SiO_2/Si . The AFM vertical height resolution is assumed to be 0.7 nm.

(in another words, at larger spacing, the tip need retract a larger distance to maintain the preset force gradient when scanning over localized charges). However, the increase of charge detection sensitivity is ultimately limited by the systematic minimum detectable change in force gradient. This value is estimated to be $\sim 10^{-5}$ to 10^{-6} N/m in ambient AFM, which corresponds to a scanning height of ~ 50 nm. The value in UHV AFM is smaller ($\sim 10^{-8}$ N/m), indicating more space to increase charge detection sensitivity. In addition, nc-AFM is more sensitive to point charges than to disk charge distribution.

Figure 5.9 shows lateral resolution of nc-AFM when scanning two point charges, which decreases as scanning height increases. At the scanning height of 10 nm, such two point charges are resolvable if they are at least 40 nm apart.

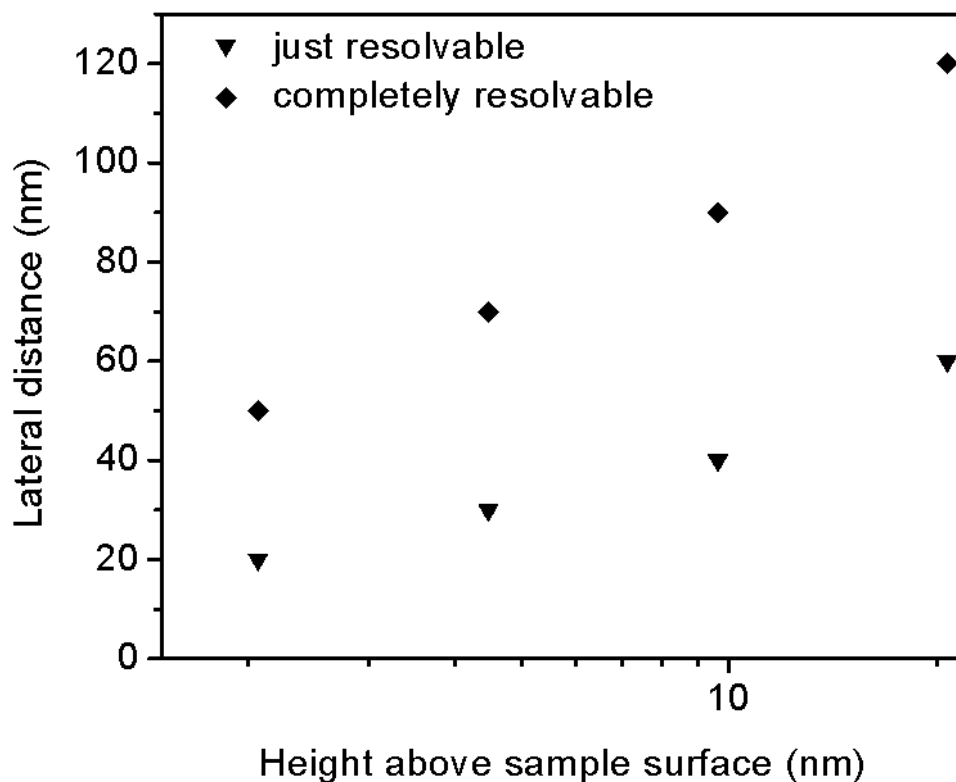


Figure 5.9. Lateral resolution of nc-AFM when scanning two point charges (each has 30 basic charges) on the surface of 12 nm SiO₂/Si as a function of tip-sample spacing. AFM tip radius is 52.5 nm.

5.6 Vertical and lateral charge dissipation

Although nc-AFM has been proven to be a sensitive tool in microscopic charge analysis, the method to extract quantitative information from AFM image is never straightforward. It is not appropriate to view protrusion in the nc-AFM image as the real charge distribution.

Figure 5.10 shows simulated nc-AFM images of localized charges and before and

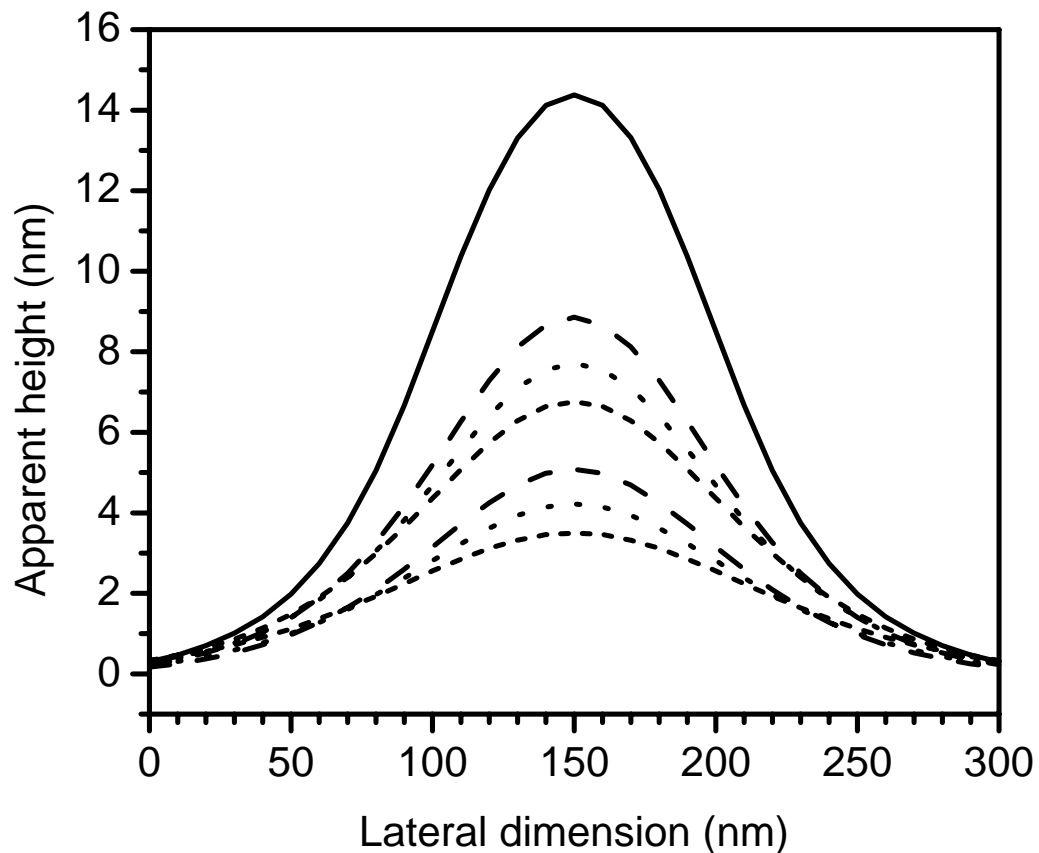


Figure 5.10. Simulated nc-AFM images of localized charges with 2D Gaussian distribution. Solid curve: initial distribution, $Q_{total} = 670 q_0$, $\sigma_{max} = 3 \times 10^{12} \text{ cm}^{-2}$, $S = 60 \text{ nm}$, $z = -10 \text{ nm}$. Dash: proportional charge loss, $Q_{total} = 586 q_0$, $\sigma_{max} = 2.625 \times 10^{12} \text{ cm}^{-2}$; $Q_{total} = 503 q_0$, $\sigma_{max} = 2.25 \times 10^{12} \text{ cm}^{-2}$. Dot: vertical movement without charge loss, $z = -20 \text{ nm}$; $z = -30 \text{ nm}$. Short dash: Lateral spreading without charge loss, $\sigma_{max} = 2.2 \times 10^{12} \text{ cm}^{-2}$, $S = 70 \text{ nm}$; $\sigma_{max} = 1.6875 \times 10^{12} \text{ cm}^{-2}$, $S = 80 \text{ nm}$.

after different means of dissipation, including proportional charge loss, vertical movement toward the substrate without charge loss, and laterally spreading out without charge loss. Compared to the nc-AFM image corresponding to the initial charge distribution, the protrusions drop in all three situations. There are some minor differences such as the protrusion being the narrowest for proportional charge loss and the widest for lateral spreading out, but without careful comparison based on electrostatic calculation, it is neither easy nor dependable to determine the means of dissipation intuitively.

In fact, some knowledge about the real charge distribution is always important in the electrostatic simulation of charge imaging by nc-AFM, which may provide multiple solutions. For example, some lateral charge dissipation plus some proportional charge loss may make the nc-AFM image look like that corresponding to vertical movement toward the substrate. Electrostatic simulation can help to test the validity of a model of charge distribution and draw quantitative information based on that. However, in order to present a reasonable model, other experimental approaches and theoretical analysis are also necessary.

5.7 Summary

By method of images algorithm, the influence of the dielectric environment was included and proved to be critical in the electrostatic simulation of charge imaging by nc-AFM. The air damping problem was completely removed by replacing ambient AFM with a UHV AFM, which also brings higher sensitivity and stability. In addition, the space charge in Si substrate was proven to be negligible in the simulation of most charge imaging experiments. With such improved models, charge detection sensitivity and

lateral resolution were re-evaluated, and the limits for quantitative charge analysis discussed. It was shown that higher detection sensitivity can be achieved by increasing the scanning height. Combined with other theoretical and experimental efforts, the quantitative charge imaging approach can provide useful information regarding microscopic charge dissipation dynamics.

Chapter 6

Electrostatic calculation related to silicon nanocrystal memory device

6.1 Introduction

The synthesis and characterization of nanoscale structures for device applications have motivated the development of methods to calculate charges, fields, and potential in complex three-dimensional nanostructured topologies. In chapter 5, a method of images algorithm was applied to calculate force gradient between conductive AFM tip and localized charges. In addition, the combination of this algorithm and numerical method show fast convergence in the calculation of space charge in Si substrate. Enlightened by the work on simulation of nc-AFM, we noticed that the theoretical analysis of Si nanocrystal memory sometimes involved similar electrostatic problems featuring multiple interfaces in which induced charges at interfaces also play an important role. So the approach mentioned above can also be applied in the simulation of nanocrystal floating gate memory device. A 3D model incorporating realistic nanocrystal distribution can be established to replace the 1D model (for conventional floating gate memory, but may not be valid in nanocrystal memory), providing electric potential distribution and its influence on the channel as well as individual nanocrystals.

6.2 Coulomb charging energy

In describing energy and charge quantization in nanocrystals, Coulomb blockade and quantum carrier confinement effects are two key concepts. These effects can be accounted for numerically with simulations based on three-dimensional Poisson and Schrödinger-like equations.^{121,122,123} For simplicity, the Coulomb charging energy for the first basic charge on a metal nanocrystal was usually calculated by

$$E_{Coulomb} = q_0^2 / 2C, \quad \text{where } C = 4\pi\epsilon_0\epsilon_r R. \quad (6.1)$$

With the method of images algorithm, more accurate values can be obtained with just dozens of image charges. Figure 6.1 shows the position and size dependence of the Coulomb charging energy of a metal nanocrystal in a MOS memory device. The coulomb charging energy decreases when the nanocrystal gets closer to the channel [Fig. 6.1(a)] and increases when the nanocrystal size becomes larger [Fig. 6.1(b)]. The size dependence agrees with formula (6.1), but with lower Coulomb charging energies (The difference is nearly 20 meV).

Using the method of images algorithm, the influence due to inhomogeneous induced charges at all interfaces within sample structures can be calculated conveniently and analytically, even for more complex situations with layered tunnel barrier structures.¹²⁴ In order to show the significant effect of the induced charges on energy in nanocrystals as well as the effectiveness of the method of images algorithm in handling such problems, the Coulomb charging energy of a single metal nanocrystal embedded in different device structures was calculated. The calculated result is given in Fig. 6.2. In addition to the most commonly used structure (I), SiO₂ is replaced partially [structure (II), (III)] or completely [structure (IV)] by high-κ dielectrics, which are believed to have the potential

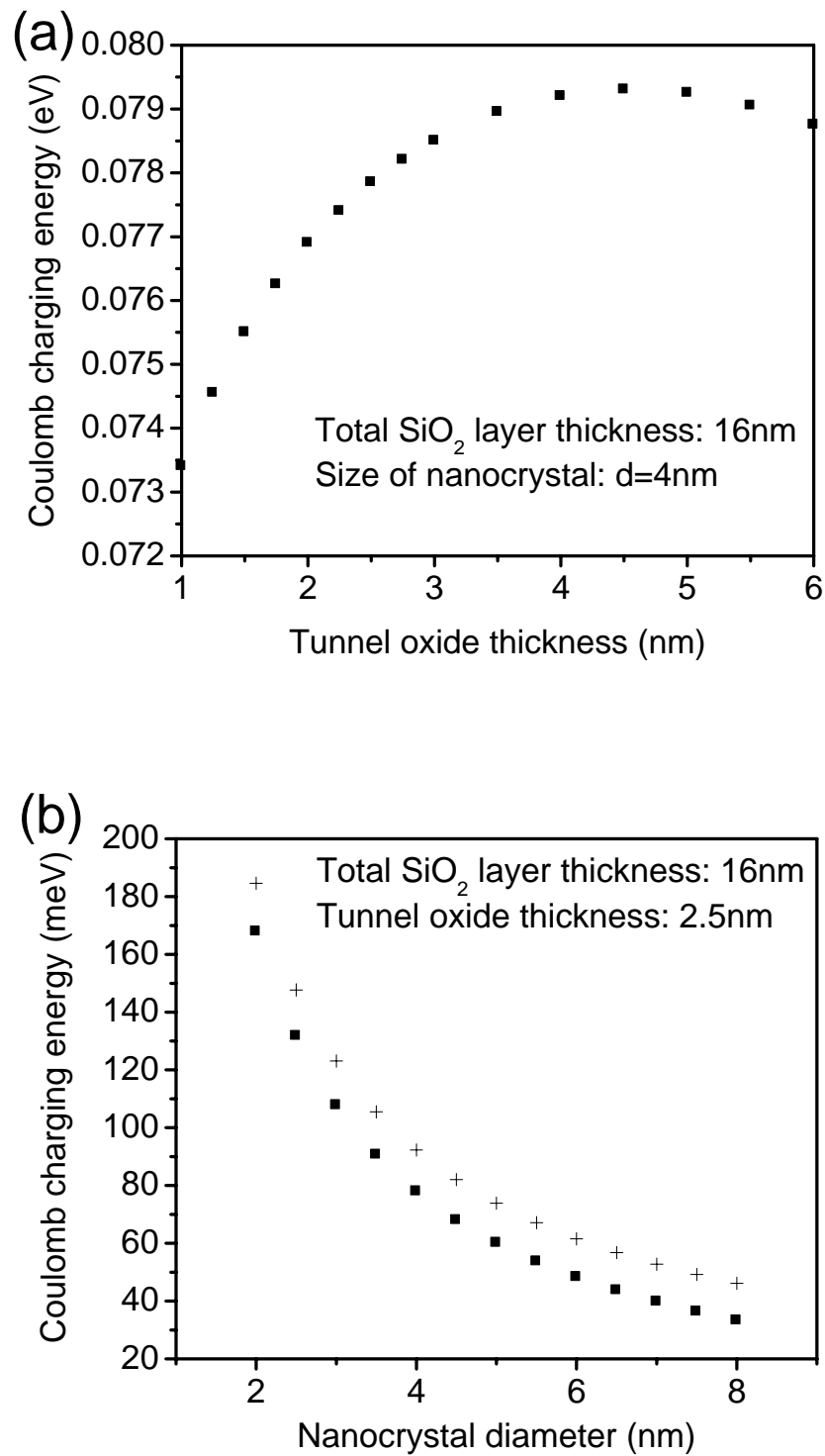


Figure 6.1. Influence of position (a) and size (b) of a nanocrystal in a memory device on Coulomb charging energy for adding the first basic charge. In (b), crosses show the result calculated with the simplest model without consideration of dielectric environment.

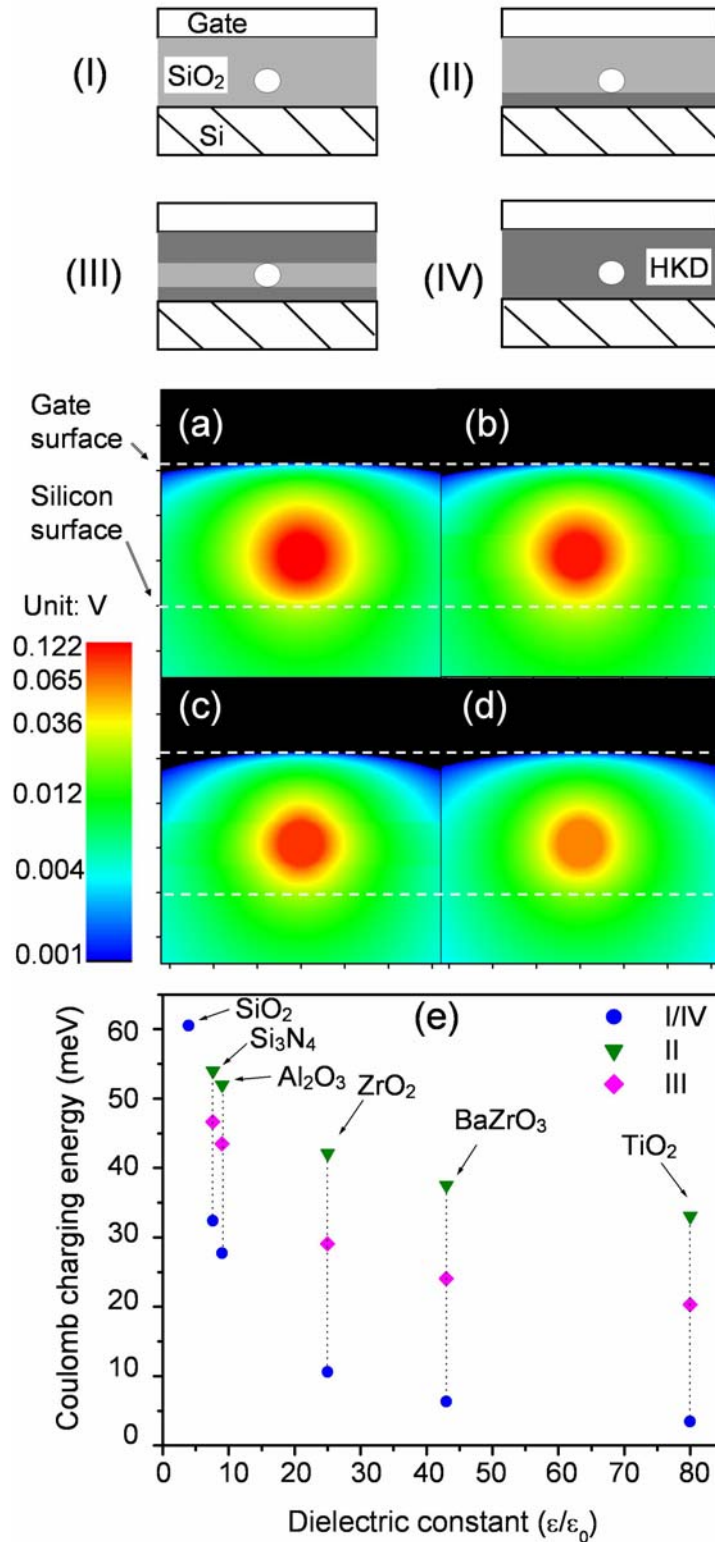


Figure 6.2. (a)–(d) Profile of the electrostatic potential distribution (absolute value) caused by 1 electron in the nanocrystal for device structures (I)–(IV), respectively. For all structures, $d_{NC}=5$ nm, $t_{TO}=3$ nm, and $t_{CO}=8$ nm. In (b), (c), and (d), the high- κ dielectric (HKD) used is Si₃N₄. (e) Coulomb charging energies for device structures (I)–(IV) with different dielectrics.

to overcome the scaling limits for SiO₂ in the complementary metal–oxide–semiconductor technology.¹²⁵ To consider the Coulomb charging energy for one basic charge in the nanocrystal with size of 5 nm, both substrate and gate are grounded. Since the corresponding change of space charge distribution in silicon substrate is a slow process compared with the change of induced charges at interfaces, silicon can be treated as pure dielectric here. Fig. 6.2(a)–(d) shows the profile of electric potential distribution (absolute value) in logarithmic color scale for device structures (I)–(IV) with Si₃N₄ as the high-κ dielectric and one electron in the nanocrystal. We note that Si₃N₄ dramatically reduces the electrostatic energy in the nanocrystal. In Fig. 6.2(e), Coulomb charging energies in these structures with various high-κ dielectric materials are summarized. It should be noted that this energy is 74 meV for SiO₂ according to formula (6.1). For those dielectrics not listed, the value can be estimated by fitting to the data. With a similar approach, the dependence of Coulomb charging energy on nanocrystal areal density was also investigated. These values are important references in the determination of suitable high-κ dielectrics for practical device applications.

6.3 Variation of channel carrier density due to separated charge storage

While numerous reports¹²¹⁻¹²³ have focused on wave function and energy level computation in nanocrystals, only a few results have been reported on the influence of nanocrystal density and distribution on the channel carrier distribution in a field effect transistor based memory device or its effect on the overall device characteristics. By using the concept of an equivalent circuit, Sim et al.¹²⁶ calculated the relationship

between the performance of nanocrystal memories and device parameters including nanocrystal distributions. In our work the method of images algorithm was applied with a finite difference approach to solve this three-dimensional problem self-consistently.

Strictly speaking, the quantized electron motion perpendicular to the channel interface should be taken into account in devices with extremely thin gate oxides and high channel doping levels.¹²⁷ However, in the following examples a semi-classical approximation¹²⁸ is applied in the 3D calculation. The doping concentration (N_A) of the p -type Si substrate is 10^{18} cm^{-3} . The thickness of the tunnel oxide is 3 nm, and the control oxide thickness is 9 nm. In the calculation of electric potential variation in the channel, charged nanocrystals with diameter of 2~3 nm were treated electrostatically as point charges. Figure 6.3 shows a 2D profile of electric potential distribution in the p -Si

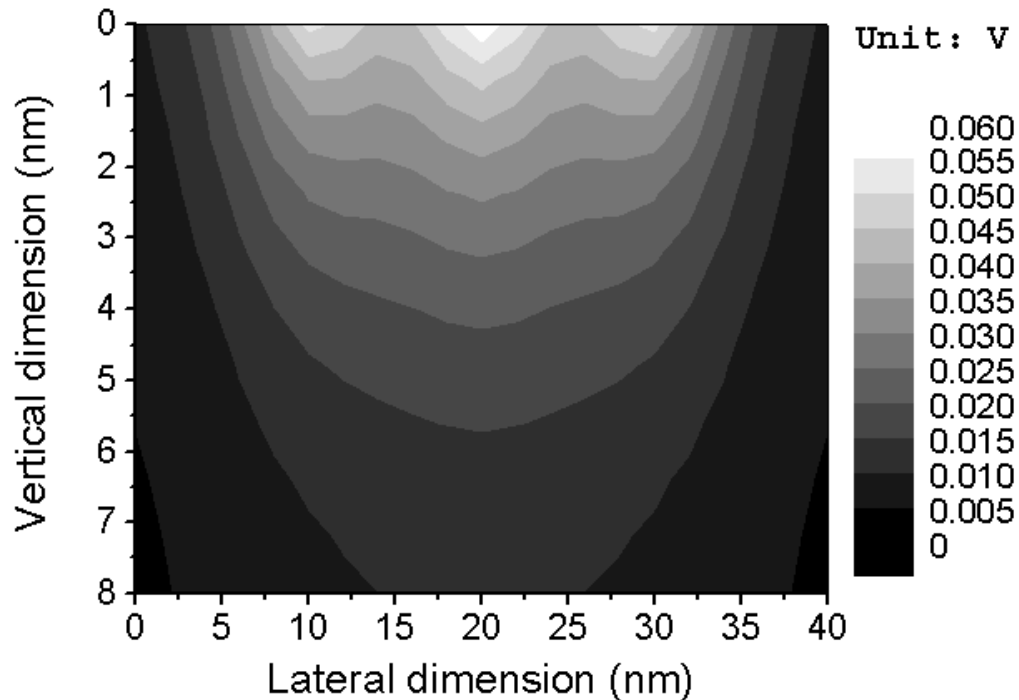


Figure 6.3. 2D profile of electric potential distribution in the p -Si substrate of a Si nanocrystal floating gate memory. The sizes of charged nanocrystals (3×3 array, each charged with one hole and with the spacing of 10 nm) are a few nanometers and treated as point charges in the simulation. $t_{TO} = 3 \text{ nm}$, $t_{CO} = 9 \text{ nm}$, and $V_G = 0$, $N_A = 10^{18} \text{ cm}^{-3}$. Work function differences were neglected.

substrate of a Si nanocrystal floating gate memory, which is due to 9 nanocrystals (3×3 array) each charged with one hole ($V_G=0$). It was found that obvious lateral potential variation begins at the spacing of around 10 nm, or 10 nm is the threshold value that 1D approximation starts to break down.

A better understanding can be obtained by calculating channel minority carrier (electron) density for gate bias around threshold voltage with periodic boundary conditions included (Fig. 6.4). The gate voltage is 4.425 V. The electron density in

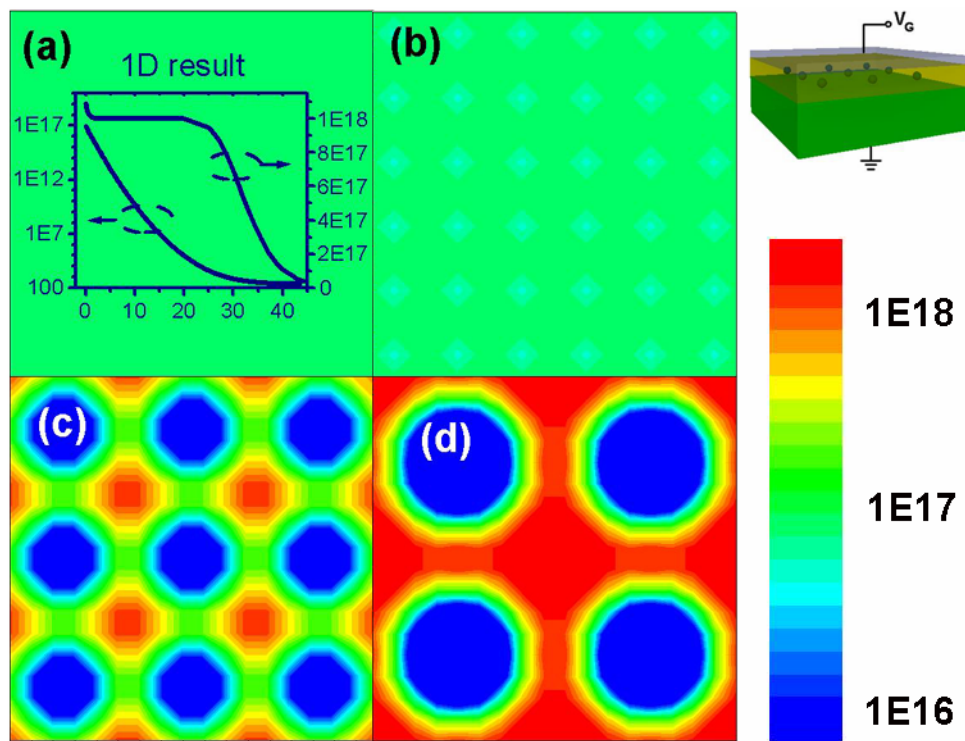


Figure 6.4. Plan views of the channel minority carrier density of a nanocrystal floating gate memory. Device structure: $t_{TO}=3$ nm, $t_{CO}=9$ nm, $N_A=10^{18}$ cm⁻³. $V_G=4.425$ V, charge density in floating gate is fixed at 4.08×10^{12} cm⁻². (a)~(d) show plan views of minority carrier (electron) densities at a central area (42×42 nm²) of channel for different density of charging centers. (a) Continuous floating gate [1D model, the figure shows depth (unit: nm) dependence of electron density (left, unit: cm⁻³) and total charge density (right, unit: cm⁻³)] (b) Inter-particle spacing is 7 nm, i.e., each nanocrystal is charged with 2 electrons (c) Assume nanocrystals aggregate. Spacing between charging centers is 14 nm, i.e., each charging center has 8 electrons. (d) Spacing between charging centers formed by aggregated nanocrystals is 21 nm, i.e., each charging center has 18 electrons.

floating gate is $4.08 \times 10^{12} \text{ cm}^{-2}$, which yields a 1.7 V threshold voltage shift relative to the uncharged floating gate. In the result, planar views of electron density at the interface between the channel and SiO_2 are shown for a homogeneously charged sheet [Fig. 6.4(a),] and three different arrays of charged nanocrystals [Figs. 6.4(b), (c) and (d)]. In the case of homogeneously charged sheet, the result was obtained from a 1D self-consistent calculation. The figures corresponding to depth (unit: nm) dependences of electron density (left, unit: cm^{-3}) and total charge density (right, unit: cm^{-3}) show a depletion layer with thickness of 30 ~ 40 nm and a weak inversion layer. In the cases of charged nanocrystals, the method of images algorithm was applied to calculate the shift of electrostatic potential at the channel due to deviation of charge distribution from planar sheet charge in floating gate. This shift of the electrostatic potential was then used to correct local electron density in the channel. At the same time, the shift of electrostatic potential caused by the change of local electron density at each grid of the channel was also taken into account. The iterations were repeated until a stable solution was reached. This approach was efficient for such 3D self-consistent problems. In the example of Fig. 6.4, after 15 iterations the total error drops exponentially to a level limited by the finite grid size.

In the result it was noticed the electron density distribution at sub-threshold for the continuously charged sheet [Fig. 6.4(a)] is close to the distribution of the electron density in Fig. 6.4(b), but differs significantly from the electron density distribution in Figures 6.4 (c) and (d). The situations vary from sub-threshold cases [Figs. 6.4(a), (b)] to the formation of isolated inversion regions [Fig. 6.4(c)] and to an inversion layer network [Fig. 6.4(d)]. These differences clearly suggest that while a one-dimensional simulation

may be enough to describe some cases with relatively small spacing between charged nanocrystals, a fully three-dimensional simulation is required in the cases with relatively large spacing between charged nanocrystals or nanocrystal agglomerates. In this example, the threshold value is again around 10 nm. The influence of inhomogeneous channel carrier density on capacitance-voltage and transistor characteristics as well as programming and dissipation processes is an interesting and important topic to be studied.

6.4 Summary

In this chapter, an initiative of 3D electrostatic simulation of Si nanocrystal memory was described. The nontrivial influence of dielectric environment on Coulomb charging energy was evaluated with the help of the method of images algorithm. The variation of channel minority carrier density was calculated by the method of images algorithm and a finite difference approach. It was found that 10 nm is the threshold value that 1D approximation starts to break down in the selected device geometry. In other words, it was proved theoretically that 10^{12} cm^{-2} is the lower bound of areal density of charged nanocrystals that 1D approximation still holds. Below this value, 3D electrostatic calculation need be applied for better accuracy.

Chapter 7

Conclusions and future directions

7.1 Conclusions

It has been said that knowledge owned by a person can be represented with a sphere; the contact area with unknown outer space increases with the volume. Indeed, with some experiments accomplished and questions answered, more questions appear and more experiments are needed to answer them. A PhD period is probably only enough time to erase several major question marks in the current field of vision.

In conclusion, we have demonstrated that STM/nc-AFM/RHEED constitute a substitute of TEM to characterize extremely small Si nanocrystals in a SiO₂ matrix. A histogram of nanocrystal sizes indicates that the sizes of most nanocrystals are between 2 to 3 nm, and the average value is 2.4 nm. A comparison between nanocrystal density ($4 \times 10^{12} - 3 \times 10^{13} \text{ cm}^{-2}$) and charge density observed in C-V measurements (up to $4 \times 10^{12} \text{ cm}^{-2}$) indicates no more than a single charge per nanocrystal on average, which is consistent with the high Coulomb charging energy and quantum confinement energy for such small Si nanocrystals. C-AFM was applied to characterize electronic properties of tunnel oxide. The observed overall high conductance, which is attributed to the narrowed and contaminated deluded zone, explains the relatively short retention time for electrons. Nanoscale charge retention characteristics were investigated by UHV nc-AFM in which a highly-doped Si tip was employed to inject charges and detect subsequent charge dissipation. Much longer hole retention time (e.g., > 1 day) than electron retention time (e.g., < 1 hour) was observed. The dissipation process of holes was further studied with

electrostatic simulation to draw quantitative data such as total charge, charge distribution, and evolution. In addition, the approach used in the quantitative charge imaging by nc-AFM was also applied in the 3D electrostatic simulation of nanocrystal memory devices.

Based on these results, a better control of nanocrystal depth distribution close to the channel is suggested to be critical in a true nonvolatile memory device. The superior retention characteristics of holes in both electrical characterization of nanocrystal floating gate MOS capacitors and more detailed nanoscale charge analysis demonstrate that *p*-channel nanocrystal memory working with holes is an interesting choice in improving data retention and in further device scaling.

7.2 Future directions

7.2.1 Nanoscale photoluminescence measurements

As discussed in chapter 5, nc-AFM images only provide indirect information about charge distribution. The methods to extract real charge distribution from nc-AFM images, such as the 3D electrostatic simulation we used, are never straightforward. Knowledge of how the charge dissipates, obtained from other experimental approaches, is always helpful to improve the accuracy of microscopic charge analysis by nc-AFM.

When a nanocrystal is charged with electrons or holes, its photoluminescence (PL) will be quenched by an Auger process, so charge status can be told by a corresponding PL signal.¹²⁹ Conventional PL measurements lack the resolution for investigation of nanoscale charge dissipation. Instead, nearfield scanning optical microscopy (NSOM) is likely a suitable instrument to directly observe nanoscale charge distribution and

evolution. Just like PL charge retention measurement (the principle is to observe the time-dependent optically-pumped PL signal after charge injection into the Si nanocrystal layer in “optical nanocrystal memory” with appropriate gate bias) or electroluminescence (EL) charge retention measurement (the principle is that after charge injection into the Si nanocrystal layer in “optical nanocrystal memory,” wait some time and then the total charge that remains in the nanocrystals can be read out by applying an opposite gate bias and measuring the emitted light. The EL peak or integrated EL signal is believed to be proportional to the total charge.) can be viewed as the optical counterpart of capacitance decay measurement, microscopic charge analysis by NSOM or a similar approach can be viewed as the optical counterpart of nc-AFM. In addition, similar to the conductive tip of nc-AFM, an NSOM tip with outside metal coating may be used for charge injection.

There are also concerns with the sensitivity of NSOM on the relatively weak photoluminescence of Si nanocrystals, which are not very efficient emitter. As an alternative, confocal microscopy may be used in a similar way.

7.2.2 Variable temperature charge retention characteristics and modelling

Hole retention characteristics have been obtained at elevated temperatures. At reduced temperatures, electron retention characteristics will also be observed easily due to smaller dissipation rates. How to interpret these results correctly and extract useful information will become the most challenging part of this research.

The electrostatic simulation of nc-AFM operation can be used to test the validity of a charge distribution. To test a charge tunneling model, the corresponding dynamic charge

dissipation process must be simulated (e.g., by Monte Carlo simulation), and the obtained time dependent charge distribution can be used to generate time dependent nc-AFM images which will be matched against the experimental nc-AFM data. It should be noted that charge imaging experiments at reduced temperatures provide good chances to study both hole and electron dissipation processes in detail.

The variable temperature charge injection and imaging experiments must be able to provide abundant data for the study of charge tunneling mechanisms. Parameters such as tunneling barrier height and average spacing between nanocrystals can be calculated. Finally, temperature calibration is always important.

7.2.3 Characterization of nanocrystal memory device working with holes

Although superior retention characteristics of holes have been clearly demonstrated, whether holes can be the working charges in practical nanocrystal memory remains largely unknown. It was generally suspected that hole injection would produce defects and degrade the tunnel oxide. A few reports indicated that low energy holes injected from the inversion layer do not affect the reliability of oxide, which is further supported by the endurance characteristics of a *p*-channel Si nanocrystal memory.⁸³ However, more tests are definitely necessary.

The endurance characterization can be performed on the *n*-channel Si nanocrystal memory devices described in this thesis. If no hole-induced degradation is observed, a *p*-channel Si nanocrystal memory may be fabricated for further testing. For optimal structure with better control of nanocrystal vertical distribution or tunnel oxide layer thickness, ion implantation energy of 1 keV was strongly suggested.⁴² In fact, hole

programming and low energy ion implantation are two major suggestions obtained from this research.

7.2.4 Future research on 3D electrostatic simulation of EFM/nanocrystal memory

In addition to conductive tip nc-AFM in which the tip is grounded, the 3D electrostatic simulation with the method of images algorithm can also be easily applied on EFM or Kelvin probe microscopy with a biased tip.

In the simulation of nanocrystal memory, some improvements can be made by including quantized channel carrier motion perpendicular to the interface. Strictly speaking, a full quantum mechanical method need be applied for such calculation. However, it is generally hard to extend quantum mechanical method to 3D, especially in a system with dimensions of tens of nanometers to hundreds of nanometers. Ancona et al.¹³⁰ introduced density-gradient theory, which is a physics-based phenomenological approach. In this method, non-locality of quantum mechanics to the lowest order was captured by assuming the electron gas to be energetically sensitive to both the density and the gradient of the density:¹³⁰

$$\varphi_{DG}^e = \varphi_{DD}^e(n) + 2b \frac{\nabla^2 \sqrt{n}}{\sqrt{n}}, \quad b = \hbar^2 / (12m^* q), \quad (7.1)$$

where the first term is in Fermi-Dirac form and the second term is density gradient dependent. It was shown that the approach can accurately take effects of quantum mechanics into account. More importantly, it can be easily extended to multiple dimensions and non-equilibrium cases. By using this approach, the accuracy of the 3D electrostatic simulation of nanocrystal memory can be further improved.

-
- ¹ R. Feynman, *There's Plenty of Room at the Bottom*. Caltech's Engineering and Science, February 1960 issue.
- ² N. Taniguchi, *On the Basic Concept of 'Nano-Technology'*. Proc. Intl. Conf. Prod. Eng. Tokyo, Part II, Japan Society of Precision Engineering (1974).
- ³ G. E. Moore, *Progress in digital integrated electronics*. IEDM Tech. Digest, pp. 11-13 (1975).
- ⁴ G. T. Tseng and J. C. Ellenbogen, *Toward Nanocomputers*. Science **294**, 1293 (2001).
- ⁵ U. Banin, Y. Cao, D. Katz, and O. Millo, *Identification of atomic-like electronic states in indium arsenide nanocrystal quantum dots*. Nature **400**, 542 (1999).
- ⁶ E. Klarreich, *Biologists join the dots*. Nature **413**, 450 (2001).
- ⁷ M. Bruchez, M. Moronne, Peter Gin, S. Weiss, and A. Paul Alivisatos, *Semiconductor Nanocrystals as Fluorescent Biological Labels*. Science **281**, 2013 (1998).
- ⁸ M. Han, X. Gao, J. Z. Su, and S. Nie, *Quantum-dot-tagged microbeads for multiplexed optical coding of biomolecules*. Nature biotechnology **19**, 631 (2001).
- ⁹ V. L. Colvin, M. C. Schlamp, and A. P. Alivisatos, *Light-emitting diodes made from cadmium selenide*. Nature **370**, 354 (1994).
- ¹⁰ S. Coe, W. K. Woo, M. Bawendi, and V. Bulovic, *Electroluminescence from single monolayers of nanocrystals in molecular organic devices*. Nature **420**, 800 (2002).
- ¹¹ M. Gao, J. Sun, E. Dulkeith, N. Gaponik, U. Lemmer, and J. Feldmann, *Lateral Patterning of CdTe Nanocrystal Films by the Electric Field Directed Layer-by-Layer Assembly Method*. Langmuir **18**, 4098 (2002).

-
- ¹² D. L. Klein, R. Roth, A.K.L. Lim, A. P. Alivisatos, and P. L. McEuen, *A single electron transistor made from a cadmium selenide nanocrystal*. *Nature* **389**, 699 (1997).
- ¹³ S. V. Kershaw, M. T. Harrison, A. L. Rogach, and A. Kornowski, *Development of IR-Emitting Colloidal II-VI Quantum-Dot Materials*. *IEEE J. Sel. Top. Quantum Electron.* **6**, 534 (2000).
- ¹⁴ A. V. Malko, A. A. Mikhailovsky, M. A. Petruska, J. A. Hollingsworth, H. Htoon, M. Bawendi, and V. I. Klimov, *From amplified spontaneous emission to microring lasing using nanocrystal quantum dot solids*. *Appl. Phys. Lett.* **81**, 1303 (2002).
- ¹⁵ L. T. Canham, *Silicon quantum wire array fabrication by electrochemical and chemical dissolution of wafers*. *Appl. Phys. Lett.* **57**, 1046 (1990).
- ¹⁶ J. Wang, H. B. Jiang, W. C. Wang, and J. B. Zheng, *Efficient Infrared-Up-Conversion Luminescence in Porous Silicon: A Quantum-Confinement-Induced Effect*. *Phys. Rev. Lett.* **69**, 3252 (1992).
- ¹⁷ R. P. Chin, Y. R. Shen, and V. Petrova-Koch, *Photoluminescence from Porous Silicon by Infrared Multiphoton Excitation*. *Science* **270**, 776 (1995).
- ¹⁸ M. Nayfeh, O. Akcakir, J. Therrien, Z. Yamani, N. Barry, W. Yu, and E. Gratton, *Highly nonlinear photoluminescence threshold in porous silicon*. *Appl. Phys. Lett.* **75**, 4112 (1999).
- ¹⁹ J. Diener, D. I. Kovalev, G. Polisski, and F. Koch, *Resonant two-photon excitation of silicon nanocrystals*. *Appl. Phys. Lett.* **74**, 3350 (1999).
- ²⁰ D. J. Lockwood, Z. H. Lu, and J. M. Baribeau, *Quantum confined luminescence in Si/SiO₂ superlattices*. *Phys. Rev. Lett.* **76**, 539 (1996).

-
- ²¹ T. Trupke, J. Zhao, A. Wang, R. Corkish, and M. Green, *Very efficient light emission from bulk crystalline silicon*. Appl Phys. Lett. **82**, 2996 (2003).
- ²² N. H. Nayfeh, N. Barry, J. Therrien, O. Akcakir, E. Gratton, and G. Belomoin, *Stimulated blue emission in reconstituted films of ultrasmall silicon nanoparticles*. Appl. Phys. Lett. **78**, 1131 (2001).
- ²³ B. Garrido, M. López, A. Pérez-Rodríguez, C. García, P. Pellegrino, R. Ferré, J. A. Moreno, J. R. Morante, C. Bonafos, M. Carrada, A. Claverie, J. de la Torre, and A. Souifi, *Optical and electrical properties of silicon-nanocrystals ion beam synthesized in SiO₂*. Nuclear Instruments and Methods in Physics Research B **216**, 213 (2004).
- ²⁴ M L Brongersma, A. Polman, K. S. Min, and H. A. Atwater, *Depth distribution of luminescent Si nanocrystals in Si implanted SiO₂ films on Si*. J. Appl. Phys. **86**, 759 (1999).
- ²⁵ J. Valenta, N. Lalic, and J. Linnros, *Electroluminescence of single silicon nanocrystals*. Appl. Phys. Lett. **84**, 1459 (2004).
- ²⁶ F. Lacona, C. Bongiorno, and C. Spinella, *Formation and evolution of luminescent Si nanoclusters produced by thermal annealing of SiO_x films*. J. Appl. Phys. **95**, 3723 (2004).
- ²⁷ G. Belomoin, E. Rogozhina, J. Therrien, P. V. Braun, L. Abuhassan, and M. H. Nayfeh, *Effects of surface termination on the band gap of ultrabright Si₂₉ nanoparticles: Experiments and computational models*. Phys. Rev. B **65**, 193406 (2002).

-
- ²⁸ M. V. Wolkin, J. Jorne, P. M. Fauchet, G. Allan, and C. Delerue, *Electronic States and Luminescence in Porous Silicon Quantum Dots: The Role of Oxygen*. Phys. Rev. Lett. **82**, 197 (1999).
- ²⁹ P. G. Kik and A. Polman, *Exciton-erbium interactions in Si nanocrystal-doped SiO₂*. J. Appl. Phys. **88**, 1992 (2000).
- ³⁰ A. Polman, *Photonic Materials Teaching Silicon new tricks*. Nature Materials **1**, 10 (2002).
- ³¹ C. Y. Chen, W. D. Chen, S. F. Song, and C. C. Hsu, *Photoluminescence of Er-doped SiO₂ films containing Si nanocrystals and Er*. Journal of Crystal Growth **253**, 10 (2003).
- ³² S. Lombardo, S. U. Campisano, G. N. Van den Hoven, A. Cacciato, and A. Polman, *Room-temperature luminescence from Er-implanted semi-insulating polycrystalline silicon*. Appl. Phys. Lett. **63**, 1942 (1993).
- ³³ T. Kimura, A. Yokoi, H. Horiguchi, R. Saito, T. Ikoma, and A. Sato, *Electrochemical Er doping of porous silicon and its room-temperature luminescence at ~1.54 μm*. Appl. Phys. Lett. **65**, 983 (1994).
- ³⁴ D. Pacifici, G. Franzò, F. Priolo, F. Iacona, and L. D. Negro, *Modeling and perspectives of the Si nanocrystals – Er interaction for optical amplification*. Phys. Rev. B **67**, 245301 (2003).
- ³⁵ Thesis by Frederic Lucarz, *Silicon nanocrystals in erbium-doped silica for optical amplifiers*. Department of Electronic and Electrical Engineering, University College London, April-August 2003

-
- ³⁶ A. Dutta, M. Kimura, Y. Honda, M. Otobe, A. Itoh, and S. Oda, *Fabrication and Electrical Characteristics of Single Electron Tunneling Devices Based on Si Quantum Dots Prepared by Plasma Processing*. Jpn. J. Appl. Phys. **36**, 4038 (1997).
- ³⁷ S. Decossas, F. Mazen, T. Baron, G. Brémond, and A. Souifi, *Atomic force microscopy nanomanipulation of silicon nanocrystals for nanodevice fabrication*. Nanotechnology **14**, 1272 (2003).
- ³⁸ B. H. Choi, S. W. Hwang, I. G. Kim, H. C. Shin, Y. Kim, and E. K. Kim, *Fabrication and room-temperature characterization of a silicon self-assembled quantum-dot transistor*. Appl. Phys. Lett. **73**, 3129 (1998).
- ³⁹ Y. Fu, M. Willander, A. Dutta, and S. Oda, *Carrier conduction in a Si-nanocrystal-based single electron transistor – I. Effect of gate bias*. Superlattices and Microstructures **28**, 3 (2000).
- ⁴⁰ N. Takahashi, H. Ishikuro, and T. Hiramoto, *Control of Coulomb blockade oscillations in silicon single electron transistors using silicon nanocrystal floating gates*. Appl. Phys. Lett. **76**, 209 (2000).
- ⁴¹ S. Tiwari, F. Rana, H. Hanafi, A. Hartstein, E. F. Crabbé, and K. Chan, *A silicon nanocrystals based memory*. Appl. Phys. Lett. **68**, 11377 (1996).
- ⁴² P. Normand, E. Kapetanakis, P. Dimitrakis, D. Skarlatos, K. Beltsios, D. Tsoukalas, C. Bonafos, G. Ben Assayag, N. Cherkashin, A. Claverie, J. A. Van Den Berg, V. Soncini, A. Agarwal, M. Ameen, M. Perego, and M. Ganciulli, *Nanocrystals manufacturing by ultra-low-energy ion-beam-synthesis for non-volatile memory applications*. Nuclear Instruments and Methods in Physics Research B **216**, 228 (2004).

-
- ⁴³ M. L. Ostraat, J. W. De Blauwe, M. L. Green, L. D. Bell, M. L. Brongersma, J. Casperson, R. C. Flagan, and H. A. Atwater, *Synthesis and characterization of aerosol silicon nanocrystal nonvolatile floating-gate memory devices*. Appl. Phys. Lett. **79**, 433 (2001).
- ⁴⁴ I. Kim, S. Han, K. Han, J. Lee, and H. Shin, Jpn. J. Appl. Phys. *Si Nanocrystal Memory Cell with Room-Temperature Single Electron Effects*. **40**, 447 (2001).
- ⁴⁵ C. Busseret, A. Souifi, T. Baron, G. Guillot, F. Martin, M. N. Semeria, and J. Gautier, *Discharge mechanisms modeling in LPCVD silicon nanocrystals using C-V and capacitance transient techniques*. Superlattices and Microstructures **28**, 493 (2000).
- ⁴⁶ B. De Salvo, C. Gerardi, S. Lombardo, T. Barno, L. Perniola, D. Mariolle, P. Mur, A. Toffoli, M. Gely, M.N. Semeria, S. Deleonibus, G. Ammendola, V. Ancarani, M. Melanotte, R. Bez, L. Baldi, D. Corso, I. Crupi, R.A. Puglisi, G. Nicotra, E. Rimini, F. Mazen, G. Ghibaud, G. Pananakakis, C. Monzio Compagnoni, D. Ielmini, A. Cacaia, A. Spinelli, Y.M. Wan, and K. van der Jeugd, *How far will silicon nanocrystals push the scaling limits of NVMs technologies?* IEDM Tech. Dig. 597 (2003).
- ⁴⁷ R. Muralidhar, R.F. Steimle, M. Sadd, R. Rao, C.T. Swift, E.J. Prinz, J. Yater, L. Grieve, K. Harber, B. Hradsky, S. Straub, B. Acred, W. Paulson, W. Chen, L. Parker, S.G.H. Anderson, M. Rossow, T. Merchant, M. Paransky, T. Huynh, D. Hadad, K.-M. Chang, and B.E. White, *A 6V embedded 90 nm silicon nanocrystal nonvolatile memory*. IEDM Tech. Dig. 601 (2003).

-
- ⁴⁸ G. Molas, B. De Salvo, G. Ghibaudo, D. Mariolle, A. Toffoli, N. Buffet, R. Puglisi, S. Lombardo, and S. Deleonibus, *Single electron effects and structural effects in ultrascaled silicon nanocrystal floating-gate memories*. IEEE Tran. Nanotechnology **3**, 42 (2004).
- ⁴⁹ G. Molas, B. De Salvo, D. Mariolle, G. Ghibaudo, A. Toffoli, N. Buffet, and S. Deleonibus, *Single electron charging and discharging phenomena at room temperature in a silicon nanocrystal memory*. Solid-State Electronics **47**, 1645 (2003).
- ⁵⁰ D. Corso, I. Crupi, G. Ammendola, S. Lombardo, and C. Gerardi, *Programming options for nanocrystal MOS memories*. Materials Science and Engineering C **23**, 687 (2003).
- ⁵¹ J. De Blauwe, *Nanocrystal nonvolatile memory devices*. IEEE Transactions on Nanotechnology **1**, 72 (2002).
- ⁵² A. Fazio, *Future directions of non-volatile memory technologies*. Mater. Res. Soc. Symp. Proc. **830**, D1.1.1 (2005).
- ⁵³ G. Binnig, H. Rohrer, Ch. Gerber, and E. Weibel, *Surface studies by scanning tunneling microscopy*. Phys. Rev. Lett. **49**, 57 (1982).
- ⁵⁴ G. Binnig, C. F. Quate, and Ch. Gerber, *Atomic force microscope*. Phys. Rev. Lett. **56**, 930 (1986).
- ⁵⁵ A. J. Mayne, F. Rose, G. Comtet, L. Hellner, and G. Dujardin, *Variable temperature STM studies of the adsorption of oxygen on the Si(111)-7 × 7 surface*. Surface Science **528**, 132 (2003).

-
- ⁵⁶ S. Fujii, U. Akiba, and M. Fujihira, *Noncontact atomic force microscopy of a mixed self-assembled monolayer of thiolates with an H- or a Cl-terminated bicycle[2.2.2]octane moiety on Au(111)*. *Nanotechnology* **15**, S19 (2004).
- ⁵⁷ D. Klinov and S. Magonov, *True molecular resolution in tapping-mode atomic force microscopy with high-resolution probes*. *Appl. Phys. Lett.* **84**, 2697 (2004).
- ⁵⁸ L. Burgi, H. Siringhaus, and R. H. Friend, *Noncontact potentiometry of polymer field-effect transistors*. *Appl. Phys. Lett.* **80**, 2913 (2002).
- ⁵⁹ W. S. Yun, J. J. Urban, Q. Gu, and H. Park, *Ferroelectric properties of individual barium titanate nanowires investigated by scanned probe microscopy*. *Nano Letters* **2**, 447 (2002).
- ⁶⁰ P. A. Rosenthal, Y. Taur, and E. T. Yu, *Direct measurement and characterization of n^+ superhalo implants in a 120 nm gate-length Si metal-oxide-semiconductor field-effect transistor using cross-sectional scanning capacitance microscopy*. *Appl. Phys. Lett.* **81**, 3993 (2002).
- ⁶¹ E. Meyer, S. P. Jarvis, and N. D. Spencer, *Scanning Probe Microscopy in Materials Science*, MRS Bullentin, 443 (July 2004).
- ⁶² P.L.T.M. Frederix, B.W. Hoogenboom, D. Fotiadis, D. J. Müller, and A. Engel, *Atomic force microscopy of biological samples*. MRS Bulletin, 449 (2004).
- ⁶³ N. C. Santos and M. A.R.B. Castanho, *An overview of the biophysical applications of the atomic force microscopy*. *Biophysical Chemistry* **107**, 133 (2004).
- ⁶⁴ M. T. Woodside and P. L. McEuen, *Scanned Probe Imaging of Single-Electron Charge States in Nanotube Quantum Dots*. *Science* **296**, 1098 (2002).

-
- ⁶⁵ H. G. Hansma, K. Kasuya, and E. Oroudjev, *Atomic force microscopy imaging and pulling of nucleic acids*. *Current Opinion in Structural Biology*, **14**, 380 (2004).
- ⁶⁶ Y. H. Liao and N. F. Scherer, *Mechanism for photon emission from Au nano-hemispheres induced by scanning tunneling microscopy*. *Appl. Phys. Lett.* **74**, 3966 (1999).
- ⁶⁷ S. Egusa, Y. H. Liao, and N. F. Scherer, *Imaging scanning tunneling microscope-induced electroluminescence in plasmonic corrals*. *Appl. Phys. Lett.* **84**, 1257 (2004).
- ⁶⁸ K. Miki, Y. Morita, H. Tokumoto, T. Sato, M. Iwatsuki, M. Suzuki, and T. Fukuda, *Real-time observation of the Si(111): (7×7)-(1×1) phase transition by scanning tunneling microscopy*. *Ultramicroscopy* **42**, 851 (1992).
- ⁶⁹ M. Anwar and I. Rouso, *Atomic force microscopy with time resolution of microseconds*. *Appl. Phys. Lett.* **86**, 014101 (2005).
- ⁷⁰ R. Crook, A. C. Graham, C. G. Smith, Ian Farrer, H. E. Beere, and D. A. Ritchie, *Erasable electrostatic lithography for quantum components*. *Nature* **424**, 751 (2003).
- ⁷¹ F.S.-S. Chien, W.-F. Hsieh, S. Gwo, A. E. Vladar, and J. A. Dagata, *Silicon nanostructures fabricated by scanning probe oxidation and tetra-methyl ammonium hydroxide etching*. *J. Appl. Phys.* **91**, 10044 (2002).
- ⁷² T. Shimizu-Iwayama, K. Fujita, S. Nakao, K. Saitoh, T. Fujita, and N. Itoh, *Visible photoluminescence in Si⁺-implanted silica glass*. *J. Appl. Phys.* **75**, 12 (1994).
- ⁷³ A. Meldrum, R. F. Haglund, L. A. Boatner, and C. W. White, *Nanocomposite materials formed by ion implantation*. *Advanced Materials* **13**, 1431 (2001).

-
- ⁷⁴ B. Garrido Fernandez, M. López, C. García, A. Pérez-Rodríguez, J. R. Morante, C. Bonafos, M. Carrada, and A. Claverie, *Influence of average size and interface passivation on the spectral emission of Si nanocrystals embedded in SiO₂*. J. Appl. Phys. **91**, 798 (2002).
- ⁷⁵ S. Tiwari, J. A. Wahl, H. Silva, F. Rana, and J. J. Welser, *Small silicon memories: confinement, single-electron, and interface state considerations*. Appl. Phys. A: Mater. Sci. Process. **71**, 403 (2000).
- ⁷⁶ K. C. Grabar, K. R. Brown, C. D. Keating, S. J. Stranick, S. Tang, and M. J. Natan, *Nanoscale characterization of gold colloid monolayers: A comparison of four techniques*. Anal. Chem. **69**, 471 (1997).
- ⁷⁷ B. Alpers, I. Rubinstein, G. Hodes, D. Porath, and O. Millo, *Energy level tunneling spectroscopy and single electron charging in individual CdSe quantum dots*. Appl. Phys. Lett. **75**, 1751 (1999).
- ⁷⁸ O. Millo, D. Katz, Y. Cao, and U. Banin, *Scanning tunneling spectroscopy of InAs nanocrystal quantum dots*. Phys. Rev. B **61**, 16773 (2000).
- ⁷⁹ T. Baron, P. Gentile, N. Magnea, and P. Mur, *Single-electron charging effect in individual Si nanocrystals*. Appl. Phys. Lett. **79**, 1175 (2001).
- ⁸⁰ E. Nogales, B. Méndez, J. Piqueras, and R. Plugaru, *Electrical characterization of nanocrystalline Si films by scanning tunnelling spectroscopy and beam-induced current in the scanning tunnelling microscope*. Nanotechnology **14**, 65 (2003).
- ⁸¹ S. M. Sze, Physics of Semiconductor Devices, 2nd ed. Wiley, New York, 1981.

-
- ⁸² S. Huang, S. Banerjee, R. T. Tung, and S. Oda, *Electron trapping, storing, and emission in nanocrystalline Si dots by capacitance–voltage and conductance–voltage measurements*. J. Appl. Phys. **93**, 576 (2003).
- ⁸³ K. Han, I. Kim, and H. Shin, *Characteristics of P-Channel Si Nano-Crystal Memory*. IEEE Trans. Electron Devices **48**, 874 (2001).
- ⁸⁴ J. S. Biteen, N. S. Lewis, H. A. Atwater, and A. Polman, *Size-dependent oxygen-related electronic states in silicon nanocrystals*. Appl. Phys. Lett. **84**, 5389 (2004).
- ⁸⁵ A. Puzder, A. J. Williamson, J. C. Grossman, and G. Galli, *Surface chemistry of silicon nanoclusters*. Phys. Rev. Lett. **88**, 097401 (2002).
- ⁸⁶ T. Franzl, D. S. Koktysh, T. A. Klar, A. L. Rogach, J. Feldmann, and N. Gaponik, *Fast energy transfer in layer-by-layer assembled CdTe nanocrystal bilayers*. Appl. Phys. Lett. **84**, 2904 (2004).
- ⁸⁷ A. Olbrich, B. Ebersberger, and C. Boit, *Conducting atomic force microscopy for nanoscale electrical characterization of thin SiO₂*. Appl. Phys. Lett. **73**, 3114 (1998).
- ⁸⁸ Y. Watanabe, A. Seko, H. Kondo, A. Sakai, S. Zaima, and Y. Yasuda, *Detection and Characterization of Stress-Induced Defects in Gate SiO₂ Films by Conductive Atomic Force Microscopy*. Jpn. J. Appl. Phys **43**, 4679 (2004).
- ⁸⁹ M. Porti, M. Nafria, X. Aymerich, A. Olbrich, and B. Ebersberger, *Electrical characterization of stressed and broken down SiO₂ films at a nanometer scale using a conductive atomic force microscope*. J. Appl. Phys. **91**, 2071 (2002).

-
- ⁹⁰ C. I. Pakes, S. Ramelow, S. Praver, and D. N. Jamieson, *Nanoscale electrical characterization of trap-assisted quasibreakdown fluctuations in SiO₂*. Appl. Phys. Lett. **84**, 3142 (2004).
- ⁹¹ R. Hasunuma, J. Okamoto, N. Tokuda, and K. Yamabe, *Nonuniformity in ultrathin SiO₂ on Si(111) characterized by conductive atomic force microscopy*. Jpn. J. Appl. Phys. **43**, 7861 (2004).
- ⁹² J. Cai and C. T. Sah, *Gate tunneling currents in ultrathin oxide metal-oxide-silicon transistors*. J. Appl. Phys. **89**, 2272 (2001).
- ⁹³ S. H. Lo, D. A. Buchanan, Y. Taur, and W. Wang, *Quantum-mechanical modeling of electron tunneling current from the inversion layer of ultra-thin-oxide nMOSFET's*. IEEE Electron Dev. Lett. **18**, 209 (1997).
- ⁹⁴ Khairurrijal, W. Mizubayashi, S. Miyazaki, and M. Hirose, *Analytic model of direct tunnel current through ultrathin gate oxides*. J. Appl. Phys. **87**, 3000 (2000).
- ⁹⁵ T. Müller, K. H. Heinig, and W. Möller, *Size and location control of Si nanocrystals at ion beam synthesis in thin SiO₂ films*. Appl. Phys. Lett. **81**, 3049 (2002).
- ⁹⁶ M. O. Andersson, Z. Xiao, S. Norrman, and O. Engström, *Model based on trap-assisted tunneling for two-level current fluctuations in submicrometer metal-silicon-dioxide-silicon diodes*. Phys. Rev. B **41**, 9836 (1990).
- ⁹⁷ E. Miranda, J. Suñé, R. Rodríguez, M. Nafria, and X. Aymerich, *Soft breakdown fluctuation events in ultrathin SiO₂ layers*. Appl. Phys. Lett. **73**, 490 (1998).

-
- ⁹⁸ R. Stomp, Y. Miyahara, S. Schaer, Q. Sun, H. Guo, and P. Grutter, *Detection of single electron charging in individual InAs quantum dot by noncontact atomic force microscopy*. Phys. Rev. Lett. **94**, 056802 (2005).
- ⁹⁹ T. Mélin, H. Diesinger, D. Deresmes, and D. Stiévenard, *Probing nanoscale dipole-dipole interactions by electric force microscopy*. Phys. Rev. Lett. **92**, 166101 (2004).
- ¹⁰⁰ J. Lambert, C. Guthmann, and M. Saint-Jean, *Relationship between charge distribution and its image by electrostatic force microscopy*. J. Appl. Phys. **93**, 5369 (2003).
- ¹⁰¹ O. Cherniavskaya, L. Chen, V. Weng, L. Yuditsky, and L. E. Brus, *Quantitative noncontact electrostatic force imaging of nanocrystal polarizability*. J. Phys. Chem. B **107**, 1525 (2003).
- ¹⁰² E. Boer, M. L. Brongersma, H. A. Atwater, R. C. Flagan, and L. D. Bell, *Localized charge injection in SiO₂ films containing silicon nanocrystals*. Appl. Phys. Lett. **79**, 791 (2001).
- ¹⁰³ C. Guillemot, P. Budau, J. Chevrier, F. Marchi, F. Comin, C. Alandi, F. Bertin, N. Buffet, Ch. Wyon, and P. Mur, *Imaging of stored charges in Si quantum dots by tapping and electrostatic force microscopy*. Europhysics Letters **59**, 566 (2002).
- ¹⁰⁴ C. Y. Ng, T. P. Chen, H. W. Lau, Y. Liu, M. S. Tse, O. K. Tan, and V. S.W. Lim, *Visualizing charge transport in silicon nanocrystals embedded in SiO₂ films with electrostatic force microscopy*. Appl. Phys. Lett. **85**, 2941 (2004).

-
- ¹⁰⁵ S. Banerjee, M. A. Salem, and S. Oda, *Conducting-tip atomic force microscopy for injection and probing of localized charges in silicon nanocrystals*. Appl. Phys. Lett. **83**, 3788 (2003).
- ¹⁰⁶ R. Dianoux, H. J.H. Smilde, F. Marchi, N. Buffet, P. Mur, F. Comin, and J. Chevrier, *Kinetic roughening of charge spreading in a two dimensional silicon nanocrystal network detected by electrostatic force microscopy*. Phys. Rev. B **71**, 125303 (2005).
- ¹⁰⁷ C. Y. Ng, T. P. Chen, M. S. Tse, V. S.W. Lim, S. Fung, and A. A. Tseng, Influence of silicon-nanocrystal distribution in SiO₂ matrix on charge injection and charge decay. Appl. Phys. Lett. **86**, 152110 (2005).
- ¹⁰⁸ R. Krishnan, Q. Xie, J. Kulik, X. D. Wang, S. Lu, M. Molinari, Y. Gao, T. D. Krauss, and P. M. Fauchet, *Effect of oxidation on charge localization and transport in a single layer of silicon nanocrystals*. J. Appl. Phys. **96**, 654 (2004).
- ¹⁰⁹ Elizabeth A. Boer, *Synthesis, Passivation and Charging of Silicon nanocrystals*. Caltech PhD thesis (2001).
- ¹¹⁰ Robert J. Walters et al, manuscript in preparation.
- ¹¹¹ C. J. Nicklaw, M. P. Pagey, S. T. Pantelides, D. M. Fleetwood, R. D. Schrimpf, K. F. Galloway, J. E. Wittig, B. M. Howard, E. Taw, W. H. McNeil, and J. F. Conley, Jr., *Defects and nanocrystals generated by Si implantation into a-SiO₂*. IEEE Transactions on Nuclear Science **47**, 2269 (2000).
- ¹¹² K. Deguchi, S. Uno, A. Ishida, T. Hirose, Y. Kamakura, and K. Taniguchi, *Degradation of ultra-thin gate oxides accompanied by hole direct tunneling: Can we keep long-term reliability of p-MOSFETs?* IEDM pp. 327 (2000).

-
- ¹¹³ U. Hartmann, *An elementary introduction to atomic force microscopy and related methods*. Institute of Experimental Physics, University of Saarbrücken, Germany.
- ¹¹⁴ J. C. Maxwell, *A treatise on Electricity and Magnetism*. 1 (1891), 3rd ed., reprint, Dover, New York, 1954.
- ¹¹⁵ Wolfgang K. H. Panofsky, *Classical Electricity and Magnetism*, 2nd edition (Addison-Wesley Publishing Company, Inc., 1962)
- ¹¹⁶ J. D. Jackson, *Classical electrodynamics*, 3rd ed. (New York: Wiley, 1999), Chap. 2, 4
- ¹¹⁷ C. D. Vansiclen, *Am. J. Phys.* 56, 1142 (1988).
- ¹¹⁸ J. H. Cloete and J. van der Merwe, *IEEE Trans. Edu.* 41, 141 (1998).
- ¹¹⁹ N. A. Burnham, R. J. Colton, and H. M. Pollock, *Phys. Rev. Lett.* 69, 144 (1992).
- ¹²⁰ K. Goto and K. Hane, *J. Appl. Phys.* 84, 4043 (1998).
- ¹²¹ G. Lannaccone and P. Coli, *Appl. Phys. Lett.* 78, 2046 (2001).
- ¹²² A. Thean and J. P. Leburton, *IEEE Electron Dev. Lett.* 22, 148 (2001).
- ¹²³ J. Sée, P. Dollfus, S. Galdin, and P. Hesto, *Physica E* 21, 496 (2004).
- ¹²⁴ J. D. Casperson, L. D. Bell, and H. A. Atwater, *J. Appl. Phys.* 92, 261 (2002).
- ¹²⁵ G. D. Wilk, R. M. Wallace, and J. M. Anthony, *J. Appl. Phys.* 89, 5243 (2001).
- ¹²⁶ J. S. Sim, J. D. Lee, and B. G. Park, *Nanotechnology* 15, S603 (2004).
- ¹²⁷ S. A. Hareland, S. Krishnamurthy, S. Jallepalli, C. Yeap, K. Hasnat, A. F. Tasch, Jr., and C. M. Maziar, *IEEE Trans. Electron. Dev.* 43, 90 (1996).
- ¹²⁸ S. M. Sze, *Physics of semiconductor devices*, 2nd edition (Wiley, New York, 1981)
- ¹²⁹ R. J. Walters, P. G. Kik, J. D. Casperson, H. A. Atwater, R. Lindstedt, M. Giorgi, and G. Bourianoff, *Appl. Phys. Lett.* **85**, 2622 (2004).

¹³⁰ M. G. Ancona and H. F. Tiersten, Phys. Rev. B **35**, 7959 (1987).

Appendix A

Information related to Omicron UHV VT STM/AFM system

A.1 STM tip/AFM cantilever selection

Etched STM tips were ordered from Molecular imaging. All tips were Pt(.8)Ir(.2) wires with diameter of 0.25 mm. A sharp tip can also be produced by cutting one end of a wire while stretching it.

Unmounted AFM cantilevers were ordered from Nanosensors. In C-AFM experiments, the contact mode cantilevers (PPP-CONT) with PtIr₅ coating were chosen to ensure superior electrical conductance. In nc-AFM experiments, the high frequency noncontact mode cantilevers (PPP-NCH) without PtIr₅ were chosen, since it was found that such coating may damage the stability of scanning. Instead, “Reflex” (Al) coating on the detector side can be selected to enhance the reflectivity of the laser beam. In addition, it was found that the cantilevers designed for electrostatic force microscopy (PPP-EFM) were not suitable for nc-AFM in our system because of the relatively low resonance frequency (~75 kHz) and/or the PtIr₅ coating. However, this type of cantilevers can be used in contact mode on hard sample surfaces.

The cantilever mounting procedure with UHV glue can be found in the manual for the Omicron system. The curing time can be reduced by increasing the curing temperature (see the data sheet for the UHV glue). However, this approach was found valid only for PtIr₅ coated cantilevers. For Si cantilevers with Al coating or without coating, doing so in air may cause surface oxidation and severely damage reflectivity of the detector side, and

maybe the tip. So unless the curing is performed in vacuum or inert gas, room temperature is highly recommended.

A.2 Self-designed parts and explanation

A.2.1 Carousel for sample/tip loading

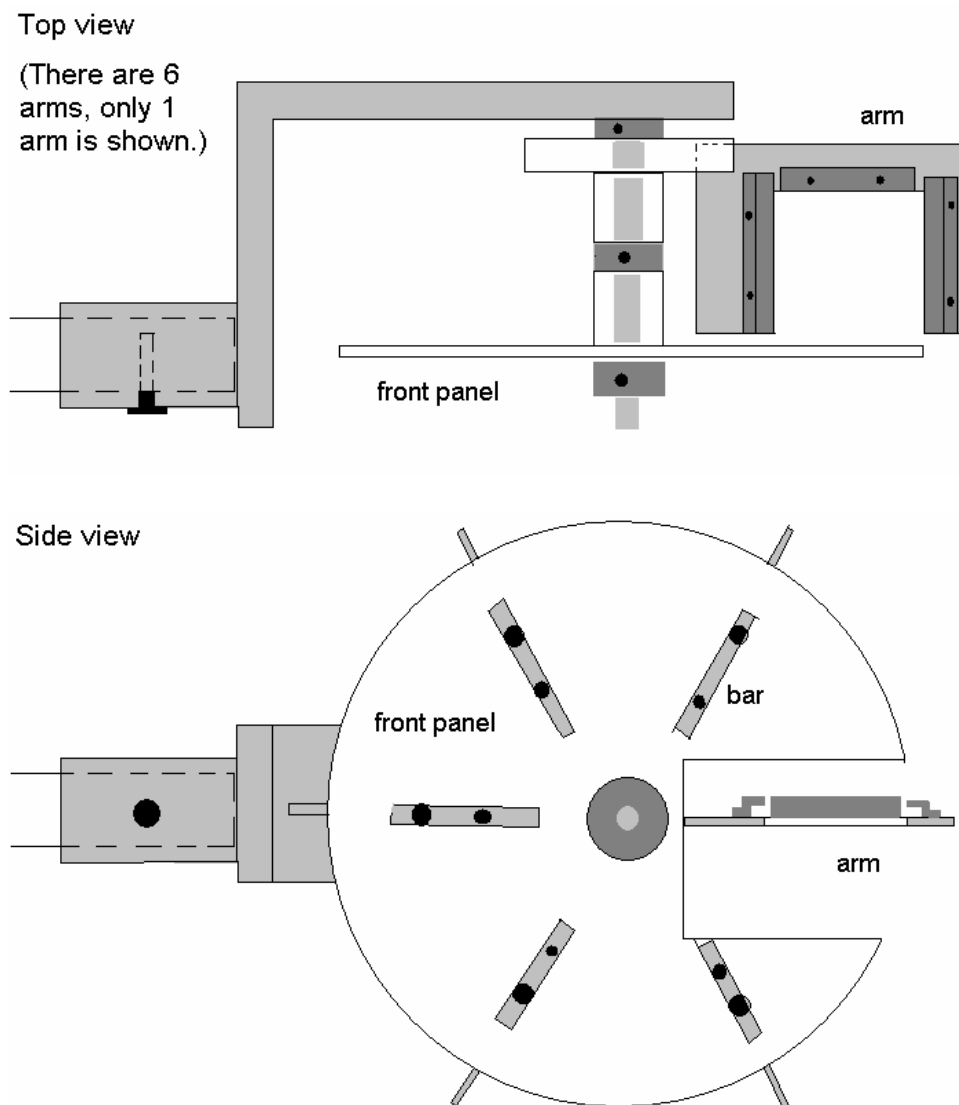


Figure A.1. Schematic of the carousel structure for sample/tip loading. Both the front panel and the arms are rotatable.

A carousel structure was designed to increase the sample/tip loading efficiency and minimize the open-close circles of the gate valve. Both the arms and the front panel are rotatable to meet the requirements at both ends of sample/tip transfer. They can be rotated by either a long tweezers (through the loading port) or the pincer grip wobble stick (near the STM/AFM stage in the UHV chamber). Each time 5 samples or tips can be transferred. To avoid possible falling off, the arm correspond to the window of the front panel were never used.

A.2.2 Standard sample plates

Omicron provided resistive/direct heating sample plates and cooling sample plates for experiments at elevated temperatures and reduced temperatures, respectively. However,

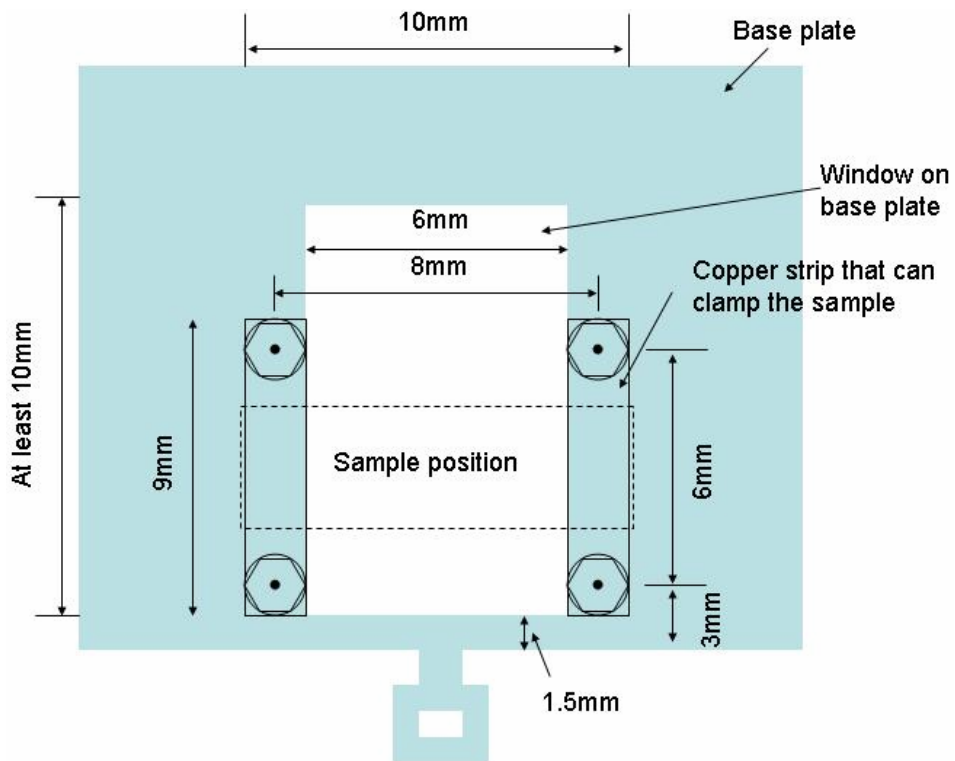


Figure A.2. Schematic of standard sample plates used for room temperature experiments.

the blank base plates for room temperature experiments need to be revised for convenient multiple use. The parameters for revision are shown in Figure A.2.

A.2.3. Cradle structure vibration isolation table and a special chamber

There are strict requirements on vibration isolation to achieve high resolution in the operation of UHV STM/AFM. In experiments, the STM/AFM stage is suspended with four springs. In addition, vibration investigation were performed to find the proper location for the instrument installation, and a cradle structure vibration isolation table were used to further reduce the vibration level while keeping a low gavity center.

In fact, the system was initially designed to be interfaced to a XPS/Auger system, so most parts were selected or designed to meet the corresponding requirements. For example, the height of the vibration isolation table was selected so that the height of loading transporter can match that in XPS/Auger system. The special chamber currently used as loading chamber was designed to be the interface chamber between two systems. Under that design, a small wobble stick would be used in the interface chamber. However, the transporter for STM/AFM system would go through the ports with 1.50 inch O.D., so the carousel structure for sample/tip loading could not be applied. With some revisions, the system still has the capability to be interfaced to the XPS/Auger system.

Appendix B

C codes for electrostatic calculation

B.1 Method of images algorithm

The following program was used to calculate the electrostatic problem in Figure 5.5. With minor revision, it can also be used to solve other similar problems such as that in Figure 6.2.

```
#include <math.h>
#include <stdio.h>
#include <conio.h>
#include <process.h>

#define outfile "c:\\users\\tao\\poten12.txt"
#define maxqnum 10000
#define e0 8.8542e-12
#define V1 0.0
#define q2 3.0*1.602e-19

double q[7+1][maxqnum+1],x[7+1][maxqnum+1],z[7+1][maxqnum+1];
int frommed[7+1][maxqnum+1];
int qnum[7+1];
int waitlst[maxqnum*7+1][2+1];

int ionum[7+1],ioobj[7+1][4+1];
int ptotal;

double xsphere[3+1],zsphere[3+1],rsphere[3+1],zinter[7+1][7+1];
double er[7+1];

void fcfinder(int med0,int med1)
{
    int i,j,k,num41,num42;
    double distance,forcex,forcez,force;
    double q41[maxqnum],x41[maxqnum],z41[maxqnum];
    double q42[maxqnum],x42[maxqnum],z42[maxqnum];

    printf("Now finding force on sphere 1...\n");

    i=0; j=0;

    for (k=1;k<=qnum[4];k++)
```

```

    {
        distance=sqrt((xsphere[1]-x[4][k])*(xsphere[1]-x[4][k])+(zsphere[1]-z[4][k])*(zsphere[1]-
            -z[4][k]));
        if (distance<rsphere[1])
        {
            i=i+1; q41[i]=q[4][k]; x41[i]=x[4][k]; z41[i]=z[4][k];
        }
        else
        {
            j=j+1; q42[j]=q[4][k]; x42[j]=x[4][k]; z42[j]=z[4][k];
        }
    }

    num41=i; num42=j;
    printf("num41=%d, num42=%d\n",num41,num42);
    forcex=0.0; forcez=0.0;

    for (i=1;i<=num41;i++)
        for (j=1;j<=num42;j++)
        {
            distance=sqrt((x41[i]-x42[j])*(x41[i]-x42[j])+(z41[i]-z42[j])*(z41[i]-z42[j]));
            force=q41[i]*q42[j]/(4.0*3.14159*e0*er[4]*distance*distance*1.0e-18);
            forcex=forcex+force*(x41[i]-x42[j])/distance;
            forcez=forcez+force*(z41[i]-z42[j])/distance;
        }

    printf("forcex=%e, forcez=%e, tan(theta)=%f\n", forcex, forcez, forcez/forcex);
}

double vfinder(double xdo,double zdo,int med0)
{
    int j;
    double voltage,distance;

    voltage=0.0;
    for (j=1;j<=qnum[med0];j++)
    {
        distance=sqrt((xdo-x[med0][j])*(xdo-x[med0][j])+(zdo-z[med0][j])*(zdo-z[med0][j]));
        voltage=voltage+q[med0][j]/(4.0*3.14159*e0*er[med0]*distance*1.0e-9);
    }
    return(voltage);
}

void mirror2(int med0,int n,int med1)
{
    double r10;

    if ((med0==4) && (med1!=5))
    {
    }

    else if ((med0==6) && (med1==7))
    {

```

```

r10=(er[med1]-er[med0])/(er[med1]+er[med0]);

if (qnum[med0]<maxqnum-10)
{
    qnum[med0]=qnum[med0]+1;
    q[med0][qnum[med0]]=-r10*q[med0][n]; x[med0][qnum[med0]]=x[med0][n];
    z[med0][qnum[med0]]=2.0*zinter[med0][med1]-z[med0][n];
    frommed[med0][qnum[med0]]=med1;
    ptotal=ptotal+1; waitlst[ptotal][1]=med0; waitlst[ptotal][2]=qnum[med0];
}

if (qnum[med1]<maxqnum-10)
{
    qnum[med1]=qnum[med1]+1;
    q[med1][qnum[med1]]=(1.0+r10)*q[med0][n];
    x[med1][qnum[med1]]=x[med0][n];
    z[med1][qnum[med1]]=z[med0][n]; frommed[med1][qnum[med1]]=med0;
}
}

else
{
    r10=(er[med1]-er[med0])/(er[med1]+er[med0]);

    if (qnum[med0]<maxqnum-10)
    {
        qnum[med0]=qnum[med0]+1;
        q[med0][qnum[med0]]=-r10*q[med0][n]; x[med0][qnum[med0]]=x[med0][n];
        z[med0][qnum[med0]]=2.0*zinter[med0][med1]-z[med0][n];
        frommed[med0][qnum[med0]]=med1;
        ptotal=ptotal+1; waitlst[ptotal][1]=med0; waitlst[ptotal][2]=qnum[med0];
    }

    if (qnum[med1]<maxqnum-10)
    {
        qnum[med1]=qnum[med1]+1;
        q[med1][qnum[med1]]=(1.0+r10)*q[med0][n];
        x[med1][qnum[med1]]=x[med0][n];
        z[med1][qnum[med1]]=z[med0][n]; frommed[med1][qnum[med1]]=med0;
        ptotal=ptotal+1; waitlst[ptotal][1]=med1; waitlst[ptotal][2]=qnum[med1];
    }
}

}

void mirrorop(int med0,int n,int med1)
{
    double l,lp,qp,xp,zp,ratio,r10;

    if ((med0==4) && (med1!=5))
    {
        l=sqrt((x[med0][n]-xsphere[med1])*(x[med0][n]-xsphere[med1])+(z[med0][n]-
        zsphere[med1])*(z[med0][n]-zsphere[med1]));
        lp=rsphere[med1]*rsphere[med1]/l;
    }
}

```

```

qp=-q[med0][n]*rsphere[med1]/l;
ratio=l/p/l;
xp=xsphere[med1]+(x[med0][n]-xsphere[med1])*ratio;
zp=zsphere[med1]+(z[med0][n]-zsphere[med1])*ratio;

qnum[med0]=qnum[med0]+1;
q[med0][qnum[med0]]=qp; x[med0][qnum[med0]]=xp; z[med0][qnum[med0]]=zp;
frommed[med0][qnum[med0]]=med1;
ptotal=ptotal+1; waitlst[ptotal][1]=med0; waitlst[ptotal][2]=qnum[med0];

if (med1!=1)
{
    qnum[med0]=qnum[med0]+1;
    q[med0][qnum[med0]]=-qp; x[med0][qnum[med0]]=xsphere[med1];
    z[med0][qnum[med0]]=zsphere[med1]; frommed[med0][qnum[med0]]=med1;
    ptotal=ptotal+1; waitlst[ptotal][1]=med0; waitlst[ptotal][2]=qnum[med0];

    qnum[med1]=qnum[med1]+1; q[med1][qnum[med1]]=-qp;
}
}

else if ((med0==6) && (med1==7))
{
    r10=(er[med1]-er[med0])/(er[med1]+er[med0]);

    qnum[med0]=qnum[med0]+1;
    q[med0][qnum[med0]]=-r10*q[med0][n]; x[med0][qnum[med0]]=x[med0][n];
    z[med0][qnum[med0]]=2.0*zinter[med0][med1]-z[med0][n];
    frommed[med0][qnum[med0]]=med1;
    ptotal=ptotal+1; waitlst[ptotal][1]=med0; waitlst[ptotal][2]=qnum[med0];

    qnum[med1]=qnum[med1]+1;
    q[med1][qnum[med1]]=(1.0+r10)*q[med0][n]; x[med1][qnum[med1]]=x[med0][n];
    z[med1][qnum[med1]]=z[med0][n]; frommed[med1][qnum[med1]]=med0;
}

else
{
    r10=(er[med1]-er[med0])/(er[med1]+er[med0]);

    qnum[med0]=qnum[med0]+1;
    q[med0][qnum[med0]]=-r10*q[med0][n]; x[med0][qnum[med0]]=x[med0][n];
    z[med0][qnum[med0]]=2.0*zinter[med0][med1]-z[med0][n];
    frommed[med0][qnum[med0]]=med1;
    ptotal=ptotal+1; waitlst[ptotal][1]=med0; waitlst[ptotal][2]=qnum[med0];

    qnum[med1]=qnum[med1]+1;
    q[med1][qnum[med1]]=(1.0+r10)*q[med0][n]; x[med1][qnum[med1]]=x[med0][n];
    z[med1][qnum[med1]]=z[med0][n]; frommed[med1][qnum[med1]]=med0;
    ptotal=ptotal+1; waitlst[ptotal][1]=med1; waitlst[ptotal][2]=qnum[med1];
}
}
}

```

```
void main()
{
    int i,j,pnow,med,n;
    double vsphere[3+1],totalq,xdo,zdo,vdo;
    FILE *fp;

    ptotal=0;pnow=0;

    //now setting outside variables to 0.

    for (i=1;i<=7;i++)
        for (j=1;j<=maxqnum;j++)
            {
                q[i][j]=0.0;
                x[i][j]=0.0;
                z[i][j]=0.0;
                frommed[i][j]=0;
            }

    for (i=1;i<=7;i++) {qnum[i]=0;}

    for (i=1;i<=maxqnum*7;i++)
    {
        waitlst[i][1]=0;
        waitlst[i][2]=0;
    }

    //now setting sphere and interface positions.

    xsphere[1]=25.0; zsphere[1]=25.0; rsphere[1]=12.0;
    xsphere[2]=0.0; zsphere[2]=5.0; rsphere[2]=5.0;
    xsphere[3]=-15.0;  zsphere[3]=5.0; rsphere[3]=5.0;

    for (i=1;i<=7;i++)
        for (j=1;j<=7;j++)
            {
                zinter[i][j]=0.0;
            }

    zinter[4][5]=zinter[5][4]=0.0;
    zinter[5][6]=zinter[6][5]=-15.0;
    zinter[6][7]=zinter[7][6]=-30.0;

    //now define relative position relations.

    ionum[1]=1; ioobj[1][1]=4;
    ionum[2]=1; ioobj[2][1]=4;
    ionum[3]=1; ioobj[3][1]=4;
    ionum[4]=4; ioobj[4][1]=1; ioobj[4][2]=2; ioobj[4][3]=3; ioobj[4][4]=5;
    ionum[5]=2; ioobj[5][1]=4; ioobj[5][2]=6;
    ionum[6]=2; ioobj[6][1]=5; ioobj[6][2]=7;
    ionum[7]=1; ioobj[7][1]=6;
```

```
//now setting dielectric constants
er[1]=er[2]=er[3]=1000.0;
er[4]=1.0;
er[5]=9.0;
er[6]=7.6;
er[7]=11.7;

//now setting initial charges.
q[1][1]=4.0*3.14159*e0*er[4]*rsphere[1]*1.0e-9*V1;
//just consider the detectable amount by outside.

q[2][1]=q2;
qnum[1]=qnum[1]+1;
qnum[2]=qnum[2]+1;

q[4][1]=q[1][1]; x[4][1]=xsphere[1]; z[4][1]=zsphere[1]; qnum[4]=qnum[4]+1;
frommed[4][1]=1; ptotal=ptotal+1; waitlst[ptotal][1]=4; waitlst[ptotal][2]=1;

q[4][2]=q[2][1]; x[4][2]=xsphere[2]; z[4][2]=zsphere[2]; qnum[4]=qnum[4]+1;
frommed[4][2]=2; ptotal=ptotal+1; waitlst[ptotal][1]=4; waitlst[ptotal][2]=2;

//output message "definition completed."
printf("Definition completed.\n");

//now begin finding image charges.

do
{
    pnow=pnow+1;
    med=waitlst[pnow][1]; n=waitlst[pnow][2];

    for (i=1;i<=ionum[med];i++)
        if (ioobj[med][i]!=frommed[med][n])
            {
                mirrorop(med,n,ioobj[med][i]);
            }

    printf("The biggest qnum is %d now.\r",qnum[4]);
} while (qnum[4]<maxqnum-10);

printf("\n");

do
{
    pnow=pnow+1;
    med=waitlst[pnow][1]; n=waitlst[pnow][2];

    for (i=1;i<=ionum[med];i++)
        if (ioobj[med][i]!=frommed[med][n])
            {
                mirror2(med,n,ioobj[med][i]);
            }
    printf("The smallest qnum is %d now.\r",qnum[7]);
}
```

```

} while ((qnum[7]<maxqnum-10) && (pnow<ptotal));

//now output several values.

for (i=1;i<=3;i++)
{
    if (qnum[i]>maxqnum) {qnum[i]=maxqnum;}
    totalq=0.0;
    for (j=1;j<=qnum[i];j++) {totalq=totalq+q[i][j];}
    vsphere[i]=totalq/(4.0*3.14159*e0*er[4]*rsphere[i]*1.0e-9);
    printf("%d.....q#:%d....V:%e\n",i,qnum[i],vsphere[i]);
}

for (i=4;i<=7;i++)
{
    if (qnum[i]>maxqnum) {qnum[i]=maxqnum;}
    printf("%d.....q#:%d\n",i,qnum[i]);
}

//now calculating potential distributions

// fcfinder(4,1);

if ((fp=fopen(outfile,"w"))==NULL)
{printf("Cannot open file outfile.\n");
getch();
exit(0);
}

for (i=0;i<=160;i++)
{
    for (j=0;j<=160;j++)
    {
        xdo=0.5*j-30; zdo=0.5*i-40.0;

        if (zdo>zinter[4][5])
        {
            if (((xdo-xsphere[1])*(xdo-xsphere[1])+(zdo-zsphere[1])*(zdo-
zsphere[1]))<=rsphere[1]*rsphere[1])
            {vdo=vsphere[1];}

            else if (((xdo-xsphere[2])*(xdo-xsphere[2])+(zdo-zsphere[2])*(zdo-
zsphere[2]))<=rsphere[2]*rsphere[2])
            {vdo=vsphere[2];}

            else if (((xdo-xsphere[3])*(xdo-xsphere[3])+(zdo-zsphere[3])*(zdo-
zsphere[3]))<=rsphere[3]*rsphere[3])
            {vdo=vsphere[3];}

            else
            {vdo=vfinder(xdo,zdo,4);}
        }
    }
}

```

```

        else if (zdo>zinter[5][6]) {vdo=vfinder(xdo,zdo,5);}
        else if (zdo>zinter[6][7]) {vdo=vfinder(xdo,zdo,6);}
        else {vdo=vfinder(xdo,zdo,7);}

        fprintf(fp,"%e\t",vdo);
    }

    fprintf(fp,"\n");
}

fclose(fp);

printf("Calculation finished, press any key...\n");
getch();
}

```

B.2 Quantitative charge imaging by nc-AFM

The following program was used to calculate nc-AFM profiles.

```

#include <math.h>
#include <stdio.h>
#include <conio.h>
#include <process.h>

#define outfile "c:\\Thesis\\simulation\\afm\\afmlineprofile_qs.txt" //nc-AFM result
#define infile "c:\\Thesis\\simulation\\afm\\qs.txt" //The initial file provides all the point charges.

#define qnum 25 //number of initial point charges
#define scansize 300e-9 //afm scan size in m
#define scannum 21 //number of pixels in afm scan

#define D 1.0e-7 //thickness of SiO2 in m
#define imgtimes 4 //a parameter in the method of images

#define rt 80.0e-9 //tip radius in m

#define q0 1.60219e-19 //basic charge
#define e0 8.8542e-12 //permittivity constant in free space
#define er1 3.9 //relative permittivity of SiO2
#define er2 11.7 //relative permittivity of Si

#define nsi 5.0e28 //number density of Si
#define nsio2 6.81e28 //number density of SiO2
#define sigma 0.34e-9 //Lennard-Jones potential parameter (for Ar)
#define epsilon 1.67e-21 //Lennard-Jones potential parameter (for Ar)
#define forcegrd 0.00887 //set-point force gradient

void setupqi(double xi[qnum+1],double yi[qnum+1],double zi[qnum+1],double qi[qnum+1])
{

```

```

FILE *fp;
int i;
float temp1,temp2,temp3,temp4;

if ((fp=fopen(infile,"rt"))==NULL)
{printf("Cannot open infile.\n");
getch();
exit(0);
}

for (i=1;i<=qnum;i++)
{fscanf(fp, "%e%e%e%e", &temp1,&temp2,&temp3,&temp4);
xi[i]=temp1;
yi[i]=temp2;
zi[i]=temp3;
qi[i]=temp4;
}

for (i=1;i<=qnum;i++)
{xi[i]=xi[i]*1e-9+scansize/2.0;
yi[i]=yi[i]*1e-9+scansize/2.0;
zi[i]=zi[i]*1e-9;
qi[i]=qi[i]*q0;
}

fclose(fp);
}

void spsioair(double xpc,double ypc,double zpc,double qpc,double xs[imgtimes+1],double
ys[imgtimes+1],double zs[imgtimes+1],double qs[imgtimes+1])
{
int i;
double r10,r21;

r10=(er1-1.0)/(er1+1.0);
r21=(er2-er1)/(er2+er1);

for (i=0;i<=imgtimes;i++) {xs[i]=xpc;ys[i]=ypc;}

zs[0]=zpc; qs[0]=qpc*(1.0-r10);

for (i=1;i<=imgtimes;i++)
if ((i%2)==1)
{zs[i]=zs[i-1]-2.0*zpc;
qs[i]=qs[i-1]*(0.0-r21);
}
else
{zs[i]=zs[i-1]-2.0*(D-zpc);
qs[i]=qs[i-1]*r10;
}
}

void spsaiar(double xpc,double ypc,double zpc,double qpc,double xs[imgtimes+1],double

```

```

        ys[imgtimes+1],double zs[imgtimes+1],double qs[imgtimes+1])
    {
        int i;
        double r10,r21;

        r10=(er1-1.0)/(er1+1.0);
        r21=(er2-er1)/(er2+er1);

        for (i=0;i<=imgtimes;i++) {xs[i]=xpc;ys[i]=ypc;}

        zs[0]=zpc; qs[0]=qpc*(1.0-r21)*(1.0-r10);

        for (i=1;i<=imgtimes;i++)
        {zs[i]=zs[i-1]-2.0*D;
        qs[i]=qs[i-1]*(0.0-r21*r10);
        }
    }

void spairair(double xpc,double ypc,double zpc,double qpc,double xs[imgtimes+1],double
ys[imgtimes+1],double zs[imgtimes+1],double qs[imgtimes+1])
{
    int i;
    double r10,r21;

    r10=(er1-1.0)/(er1+1.0);
    r21=(er2-er1)/(er2+er1);

    for (i=0;i<=imgtimes;i++) {xs[i]=xpc;ys[i]=ypc;}

    zs[0]=zpc; qs[0]=qpc;
    zs[1]=2.0*D-zpc; qs[1]=qpc*(0.0-r10);
    zs[2]=0.0-zpc; qs[2]=qpc*(0.0-r21)*(1.0+r10)*(1.0-r10);

    for (i=3;i<=imgtimes;i++)
    {zs[i]=zs[i-1]-2.0*D;
    qs[i]=qs[i-1]*(0.0-r21*r10);
    }
}

void setupq(double xi[qnum+1],double yi[qnum+1],double zi[qnum+1],double qi[qnum+1],double
x[qnum+1][imgtimes+1],double y[qnum+1][imgtimes+1],double z[qnum+1][imgtimes+1],
double q[qnum+1][imgtimes+1])
{
    int i,j;
    double xs[imgtimes+1],ys[imgtimes+1],zs[imgtimes+1],qs[imgtimes+1];

    for (i=1;i<=qnum;i++)
    {
        if (zi[i]<0)
            {spsiair(xi[i],yi[i],zi[i],qi[i],xs,ys,zs,qs);}
        else if ((zi[i]>0) && (zi[i]<D))
            {spsioair(xi[i],yi[i],zi[i],qi[i],xs,ys,zs,qs);}
        else if (zi[i]>D)

```

```

        {spairair(xi[i],yi[i],zi[i],qi[i],xs,ys,zs,qs);}
    else
        {printf("initial data error---point charge can't be exactly at interface.\n");
          getch(); exit(0);
        }

    for (j=0;j<=imgtimes;j++)
    {
        x[i][j]=xs[j];
        y[i][j]=ys[j];
        z[i][j]=zs[j]-D;          //due to the difference between structue definitions
        q[i][j]=qs[j];
    }
}

double geth0(double A, double B)
{
    double z1,zn3;

    z1=1e-6;    //initial height of AFM tip in m
    zn3=pow(z1,-3.0);
    do
    {
        zn3=zn3*2.0/3.0+(A*zn3*2.0/3.0-forcegrd)/(3.0*B*zn3*zn3-A);
    } while (fabs(A*zn3-B*pow(zn3,3)-forcegrd)>1e-10);
    z1=pow(zn3,-0.33333333);
    return(z1);
}

double geth(double x[qnum+1][imgtimes+1],double y[qnum+1][imgtimes+1],double
            z[qnum+1][imgtimes+1],double q[qnum+1][imgtimes+1],int itip,int jtip,double
            height0,double A,double B)
{
    double xm[qnum+1][imgtimes+1],ym[qnum+1][imgtimes+1],zm[qnum+1][imgtimes+1],
            qm[qnum+1][imgtimes+1];
    double f1,f2,xtip,ytip,ztip,l,z21,rz2,ratio;
    int i,j,m,n;

    xtip=(scansize/(scannum-1))*(itip-1);
    ytip=(scansize/(scannum-1))*(jtip-1);

    do
    {
        ztip=height0+rt;
        f1=0;f2=0;
        for (i=1;i<=qnum;i++)
            for (j=0;j<=imgtimes;j++)
            {
                l=sqrt((x[i][j]-xtip)*(x[i][j]-xtip)+(y[i][j]-ytip)*(y[i][j]-ytip)+(z[i][j]-
                    ztip)*(z[i][j]-ztip));
                qm[i][j]=0-q[i][j]*rt/l;
                ratio=(rt*rt/l)/l;
            }
    }
}

```

```

        xm[i][j]=xtip+(x[i][j]-xtip)*ratio;
        ym[i][j]=ytip+(y[i][j]-ytip)*ratio;
        zm[i][j]=ztip+(z[i][j]-ztip)*ratio;
    }

    for (i=1;i<=qnum;i++)
        for (j=0;j<=imgtimes;j++)
            for (m=1;m<=qnum;m++)
                for (n=0;n<=imgtimes;n++)
                    {
                        z21=zm[m][n]-z[i][j];
                        rz2=(xm[m][n]-x[i][j])*(xm[m][n]-x[i][j])+(ym[m][n]-
                            y[i][j])*(ym[m][n]-y[i][j])+z21*z21;
                        f1=f1+(pow(rz2,-1.5)-3*z21*z21*pow(rz2,-2.5))
                            *q[i][j]*qm[m][n]/(4*3.1415927*e0);
                        f2=f2+(15.0*z21*z21*z21*pow(rz2,-3.5)-9.0*z21*z21*pow(rz2,-
                            2.5))*q[i][j]*qm[m][n]/(4*3.1415927*e0);
                    }

                f1=f1+A*pow(height0,-3.0)-B*pow(height0,-9.0);
                f1=f1-forcegrd;
                f2=f2+9.0*B*pow(height0,-10.0)-3.0*A*pow(height0,-4.0);
                height0=height0-f1/f2;

    } while (fabs(f1)>1e-5);

    return(height0);
}

main()
{
    int i,j;
    double xi[qnum+1],yi[qnum+1],zi[qnum+1],qi[qnum+1];
    double x[qnum+1][imgtimes+1],y[qnum+1][imgtimes+1],z[qnum+1][imgtimes+1],
        q[qnum+1][imgtimes+1];
    double height0,A,B;
    double temp[scannum+1];
    FILE *fp;

    printf("Now begin program, press any key...\n");
    getch();
    setupqi(xi,yi,zi,qi);
    printf("qi is set:\n");
    printf("%e %e %e %e\n",xi[1],yi[1],zi[1],qi[1]);
    setupq(xi,yi,zi,qi,x,y,z,q);
    printf("q is set:\n");
    for (i=0;i<=imgtimes;i++) {printf("%e %e %e %e\n",x[1][i],y[1][i],z[1][i],q[1][i]);}

    A=4*3.1415926*3.1415927*epsilon*nsi*nsio2*pow(sigma,6.0)*rt/3.0;
    B=A*3.0*pow(sigma,6.0)/22.5; //A and B are L-J force gradient parameters
    height0=geth0(A,B);

    printf("H=%e\n",A*3.0/rt);
}

```

```

printf("A=%e\nB=%e\n",A,B);
printf("Height=%e\n Press any key to continue...\n",height0);
getch();

if ((fp=fopen(outfile,"w"))==NULL)
    {printf("Cannot open outfile.\n");
    getch();
    exit(0);
    }

printf("Now begin calculation...please wait.....\n");

for (i=(scannum+1)/2;i<=(scannum+1)/2;i++)
    {
        if (i%2==1)
            for (j=1;j<=scannum;j++)
                {
                    height0=geth(x,y,z,q,i,j,height0,A,B);
                    fprintf(fp,"%0.2f\n",height0*1e9);
                    printf("NO.%d---%d.....%f\n",i,j,height0*1e9);
                }
            else
                {
                    for (j=scannum;j>=1;j--)
                        {
                            height0=geth(x,y,z,q,i,j,height0,A,B);
                            temp[j]=height0*1e9;
                            printf("NO.%d---%d.....%f\n",i,j,height0*1e9);
                        }

                    for (j=1;j<=scannum;j++)
                        {
                            fprintf(fp,"%0.2f\n",temp[j]);
                        }
                }
            fprintf(fp,"\n");
    }

fclose(fp);
printf("All finished. Press any key.\n");
getch();
return(0);
}

```

B.3 3D calculation of channel carrier density in nanocrystal memory

The following program was used to calculate the results in Figure 6.4.

```

//It is used to get a 3D potential/charge density distribution in Si substrate.
//it outputs a 2D vertical profile and a plan view profile at interface.

#include <math.h>
#include <stdio.h>
#include <conio.h>

```

```

#include <process.h>

#define outfile1 "c:\\vert21.txt"
#define outfile2 "c:\\plan21.txt"

#define Np 1.0e24
#define T 300
#define ni 1.45e16
#define pi 3.1415926
#define q0 1.60219e-19
#define kb 1.38066e-23
#define e0 8.8542e-12 //permittivity in free space
#define er1 3.9 //relative permittivity of SiO2
#define er2 11.7 //relative permittivity of Si
#define xydmax 18 //# of grid points spacings in x and y direction. must be even.
#define zdmax 20 //# of grid points spacings in z direction.
#define hx0 2.33333e-9 //spacing between grid points
#define hy0 2.33333e-9
#define hz0 0.1e-9
#define qnum 612 //initial point charge numbers 24*24+6*6
#define imgtimes 10 //imaging operation times
#define D 1.2e-8
#define rlxtimes 4

double v1d[zdmax+1];
double roud[zdmax+1];

void spsiosi(double xpc,double ypc,double zpc,double qpc,double xs[imgtimes+1],double
ys[imgtimes+1],double zs[imgtimes+1],double qs[imgtimes+1])
{
    int i;
    double r10,r21;

    r10=-1.0;
    r21=(er2-er1)/(er2+er1);

    for (i=0;i<=imgtimes;i++) {xs[i]=xpc;ys[i]=ypc;}

    zs[0]=zpc; qs[0]=qpc*(1.0+r21);

    for (i=1;i<=imgtimes;i++)
        if ((i%2)==1)
            {zs[i]=zs[i-1]+2.0*(D-zpc);
             qs[i]=qs[i-1]*r10;
            }
        else
            {zs[i]=zs[i-1]+2.0*zpc;
             qs[i]=qs[i-1]*(0.0-r21);
            }
}

void spmetsi(double xpc,double ypc,double zpc,double qpc,double xs[imgtimes+1],double
ys[imgtimes+1],double zs[imgtimes+1],double qs[imgtimes+1])

```

```
{
    int i;
    double r10,r21;

    r10=-1.0;
    r21=(er2-er1)/(er2+er1);

    for (i=0;i<=imgtimes;i++) {xs[i]=xpc;ys[i]=ypc;}

    zs[0]=zpc; qs[0]=qpc*(1.0+r10)*(1.0+r21);

    for (i=1;i<=imgtimes;i++)
        {zs[i]=zs[i-1]+2.0*D;
          qs[i]=qs[i-1]*(0.0-r21*r10);
        }
}

void spsisi(double xpc,double ypc,double zpc,double qpc,double xs[imgtimes+1],double
           ys[imgtimes+1],double zs[imgtimes+1],double qs[imgtimes+1])
{
    int i;
    double r10,r21;

    r10=-1.0;
    r21=(er2-er1)/(er2+er1);

    for (i=0;i<=imgtimes;i++) {xs[i]=xpc;ys[i]=ypc;}

    zs[0]=zpc; qs[0]=qpc;
    zs[1]=0.0-zpc; qs[1]=qpc*r21;
    zs[2]=2.0*D-zpc; qs[2]=qpc*r10*(1.0-r21)*(1.0+r21);

    for (i=3;i<=imgtimes;i++)
        {zs[i]=zs[i-1]+2.0*D;
          qs[i]=qs[i-1]*(0.0-r21*r10);
        }
}

void output1(double v[xydmax+1][xydmax+1][zdmx+1])
{
    FILE *fp;
    int i,j,k;
    double x,np,np0;

    np0=ni*ni/Np;

    if ((fp=fopen(outfile1,"w"))==NULL)
        {printf("Cannot open file outfile.\n");
          getch();
          exit(0);
        }
    for (k=zdmx;k>=1;k--)
        {
```

```

        for (j=1;j<=xydmax;j++)
        {
            i=j;
            x=q0*(v[i][j][k]+v1d[k])/(kb*T);
            np=np0*exp(x);
            fprintf(fp,"%f\t",np);
        }
        fprintf(fp,"\n");
    }
    fclose(fp);
}

void output2(double v[xydmax+1][xydmax+1][zdmx+1])
{
    FILE *fp;
    int i,j,k;
    double x,np,np0;

    np0=ni*ni/Np;

    if ((fp=fopen(outfile2,"w"))==NULL)
        {printf("Cannot open file outfile.\n");
        getch();
        exit(0);
        }
    k=1;
    for (i=1;i<=xydmax;i++)
    {
        for (j=1;j<=xydmax;j++)
        {
            x=q0*(v[i][j][k]+v1d[k])/(kb*T);
            np=np0*exp(x);
            fprintf(fp,"%f\t",np);
        }
        fprintf(fp,"\n");
    }
    fclose(fp);
}

void setupv(double xi[qnum+1],double yi[qnum+1],double zi[qnum+1],double qi[qnum+1],double
v[xydmax+1][xydmax+1][zdmx+1])
{
    double xs[imgtimes+1],ys[imgtimes+1],zs[imgtimes+1],qs[imgtimes+1];
    double dis2,xdst,ydst;
    int i,j,k,l,s;

    for (l=1;l<=qnum;l++)
    {
        if (zi[l]<D)
        {
            spsiosi(xi[l],yi[l],zi[l],qi[l],xs,ys,zs,qs);
        }
    }
}

```



```

    }

np0=ni*ni/Np; pp0=Np+np0;
for (l=1;l<=xydmax;l++)
    {printf("*");
    for (m=1;m<=xydmax;m++)
        for (n=1;n<=zdmax;n++)
            {xsi=hx0*(l-0.5); ysi=hy0*(m-0.5); zsi=0.0-hz0*(n-0.5);
            relav=q0*(v[l][m][n]+v1d[n])/(kb*T);

            if (relav>38.7)
                {
                    rou=q0*(pp0*(exp(0.0-38.7)-1)-np0*(exp(38.7)-1));
                }
            else
                {
                    rou=q0*(pp0*(exp(0.0-relav)-1)-np0*(exp(relav)-1));
                }

            rou=rou-rou1d[n];
            qsi=rou*hx0*hy0*hz0;
            spsisi(xsi,ysi,zsi,qsi,xs,ys,zs,qs);
            for (i=1;i<=xydmax;i++)
                for (j=1;j<=xydmax;j++)
                    for (k=1;k<=zdmax;k++)
                        for (s=0;s<=imgtimes;s++)
                            {if ((i==1) && (j==m) && (k==n) && (s==0)) {break;}
                            xdst=fabs(xs[s]-hx0*(i-0.5));
                            if (xdst>(hx0*xydmax/2.0)) {xdst=hx0*xydmax-xdst;}
                            ydst=fabs(ys[s]-hy0*(j-0.5));
                            if (ydst>(hy0*xydmax/2.0)) {ydst=hy0*xydmax-ydst;}
                            dis2=xdst*xdst+ydst*ydst+(zs[s]+hz0*(k-0.5))*(zs[s]+hz0*(k-0.5));
                            ve[i][j][k]=ve[i][j][k]+qs[s]/(4.0*pi*e0*er2*sqrt(dis2));
                            }
                        }
                    }
                }
            }
        }
    }
}

printf("\n");

totalq=0.0; deltaq=0.0; totalq2=0.0;
for (i=1;i<=xydmax;i++)
    for (j=1;j<=xydmax;j++)
        for (k=1;k<=zdmax;k++)
            {
                relav=q0*(v[i][j][k]+v1d[k])/(kb*T);

                if (relav>38.7)
                    {
                        rou=q0*(pp0*(exp(0.0-38.7)-1)-np0*(exp(38.7)-1));
                    }
                else
                    {
                        rou=q0*(pp0*(exp(0.0-relav)-1)-np0*(exp(relav)-1));
                    }
            }
    }
}

```

```

        rou=rou-rou1d[k];
        relav=q0*(ve[i][j][k]+v1d[k])/(kb*T);
        if (relav>38.7)
        {
            rou2=q0*(pp0*(exp(0.0-38.7)-1)-np0*(exp(38.7)-1));
        }
        else
        {
            rou2=q0*(pp0*(exp(0.0-relav)-1)-np0*(exp(relav)-1));
        }
        rou2=rou2-rou1d[k];

        totalq=totalq+fabs(rou);
        totalq2=totalq2+rou;
        deltaq=deltaq+fabs(rou2-rou);
    }
    printf("totalq=%e, deltaq=%e, totalq2=%e\n",totalq*hx0*hy0*hz0/q0,deltaq*hx0*hy0*hz0/q0,
        totalq2*hx0*hy0*hz0/q0);
    errorq=deltaq/totalq;
    return(errorq);
}

```

```

void setupqi(double xi[qnum+1],double yi[qnum+1],double zi[qnum+1],double qi[qnum+1])
{int i,j,n;

    n=0;

    for (i=0;i<=23;i++)
        for (j=0;j<=23;j++)
        {
            n=n+1;
            xi[n]=(0.875+i*1.75)*1.0e-9;
            yi[n]=(0.875+j*1.75)*1.0e-9;
            zi[n]=3.0e-9;
            qi[n]=0.0-(72*(-q0)/(24*24));
        }

    for (i=0;i<=5;i++)
        for (j=0;j<=5;j++)
        {
            n=n+1;
            xi[n]=(3.5+i*7.0)*1.0e-9;
            yi[n]=(3.5+j*7.0)*1.0e-9;
            zi[n]=3.0e-9;
            qi[n]=-q0*2.0;
        }
}

```

```

double dopoint(double v[xydmax+1][xydmax+1][zdmx+1],int l,int m,int n,double density0)
{
    int i,j,k,s;
    double xs[imgtimes+1],ys[imgtimes+1],zs[imgtimes+1],qs[imgtimes+1];
    double densityl,xsi,ysi,zsi,qsi,relav,np0,pp0,dis2,xdst,ydst;

    np0=ni*ni/Np; pp0=Np+np0;

    xsi=hx0*(1-0.5); ysi=hy0*(m-0.5); zsi=0.0-hz0*(n-0.5);
    relav=q0*(v[l][m][n]+v[l][n])/ (kb*T);
    densityl=q0*(pp0*(exp(0.0-relav)-1)-np0*(exp(relav)-1));
    densityl=densityl-rould[n];
    qsi=(densityl-density0)*hx0*hy0*hz0;
    spsisi(xsi,ysi,zsi,qsi,xs,ys,zs,qs);

    for (i=1;i<=xydmax;i++)
        for (j=1;j<=xydmax;j++)
            for (k=1;k<=zdmx;k++)
                for (s=0;s<=imgtimes;s++)
                    {if ((i==1) && (j==m) && (k==n) && (s==0)) {break;}
                     xdst=fabs(xs[s]-hx0*(i-0.5));
                     if (xdst>(hx0*xydmax/2.0)) {xdst=hx0*xydmax-xdst;}
                     ydst=fabs(ys[s]-hy0*(j-0.5));
                     if (ydst>(hy0*xydmax/2.0)) {ydst=hy0*xydmax-ydst;}
                     dis2=xdst*xdst+ydst*ydst+(zs[s]+hz0*(k-0.5))*(zs[s]+hz0*(k-0.5));
                     v[i][j][k]=v[i][j][k]+qs[s]/(4.0*pi*e0*er2*sqrt(dis2));
                    }

    return(densityl);
}

void dorelax(double xi[qnum+1],double yi[qnum+1],double zi[qnum+1],double qi[qnum+1],double
v[xydmax+1][xydmax+1][zdmx+1],double rou[xydmax+1][xydmax+1][zdmx+1])
{
    int i,j,k,a,num;

    for (k=1;k<=zdmx;k++)
        for (a=1;a<=xydmax-1;a=a+2)
            {i=(xydmax+1-a)/2;
             j=i;
             rou[i][j][k]=dopoint(v,i,j,k,rou[i][j][k]);
             for (num=1;num<=a;num++)
                 {i=i+1;
                  rou[i][j][k]=dopoint(v,i,j,k,rou[i][j][k]);
                  }
             for (num=1;num<=a;num++)
                 {j=j+1;
                  rou[i][j][k]=dopoint(v,i,j,k,rou[i][j][k]);
                  }
             for (num=1;num<=a;num++)
                 {i=i-1;
                  rou[i][j][k]=dopoint(v,i,j,k,rou[i][j][k]);
                  }
            }
}

```

```

        }
        for (num=1;num<=a-1;num++)
        {j=j-1;
         rou[i][j][k]=dopoint(v,i,j,k,rou[i][j][k]);
        }
    }

main()
{
    double v[xydmax+1][xydmax+1][zdmax+1];
    double rou[xydmax+1][xydmax+1][zdmax+1];
    double xi[qnum+1],yi[qnum+1],zi[qnum+1],qi[qnum+1];
    int i,j,k;
    double rouerror[rlxtimes+1];

// 1D result calculated using another program. For simplicity, directly input here.
v1d[1]=8.71175e-001; rou1d[1]=-1.09075e+024*q0;
v1d[2]=8.66059e-001; rou1d[2]=-1.07446e+024*q0;
v1d[3]=8.60961e-001; rou1d[3]=-1.06113e+024*q0;
v1d[4]=8.55879e-001; rou1d[4]=-1.05022e+024*q0;
v1d[5]=8.50814e-001; rou1d[5]=-1.04128e+024*q0;
v1d[6]=8.45765e-001; rou1d[6]=-1.03396e+024*q0;
v1d[7]=8.40733e-001; rou1d[7]=-1.02795e+024*q0;
v1d[8]=8.35717e-001; rou1d[8]=-1.02302e+024*q0;
v1d[9]=8.30717e-001; rou1d[9]=-1.01897e+024*q0;
v1d[10]=8.25733e-001; rou1d[10]=-1.01565e+024*q0;
v1d[11]=8.20765e-001; rou1d[11]=-1.01291e+024*q0;
v1d[12]=8.15812e-001; rou1d[12]=-1.01066e+024*q0;
v1d[13]=8.10876e-001; rou1d[13]=-1.00881e+024*q0;
v1d[14]=8.05955e-001; rou1d[14]=-1.00728e+024*q0;
v1d[15]=8.01049e-001; rou1d[15]=-1.00602e+024*q0;
v1d[16]=7.96159e-001; rou1d[16]=-1.00498e+024*q0;
v1d[17]=7.91285e-001; rou1d[17]=-1.00413e+024*q0;
v1d[18]=7.86427e-001; rou1d[18]=-1.00342e+024*q0;
v1d[19]=7.81584e-001; rou1d[19]=-1.00284e+024*q0;
v1d[20]=7.76756e-001; rou1d[20]=-1.00235e+024*q0;
// End of 1D result.

    for (i=1;i<=xydmax;i++)
        for (j=1;j<=xydmax;j++)
            for (k=1;k<=zdmax;k++)
                {
                    v[i][j][k]=0.0;
                    rou[i][j][k]=0.0;
                }

    printf("set up qi...\n");
    setupqi(xi,yi,zi,qi);

    printf("set up v...\n");
    setupv(xi,yi,zi,qi,v);

```

```
printf("Now begin error estimation...\n");
rouerror[0]=errorest(xi,yi,zi,qi,v);
printf("The error is %f%%...\n",rouerror[0]*100.0);
//
getch();

for (i=1;i<=rlxtimes;i++)
    {printf("Now doing relax No.%d...\n",i);
      dorelax(xi,yi,zi,qi,v,rou);
      printf("Now begin error estimation...\n");
      rouerror[i]=errorest(xi,yi,zi,qi,v);
      printf("The error is %f%%...\n",rouerror[i]*100.0);
//
      getch();
    }

output1(v);
output2(v);

printf("Calculation finished, press any key...\n");
getch();
return(0);
}
```